Alma Mater Studiorum · Università di Bologna

Scuola di Scienze
Dipartimento di Fisica e Astronomia
Corso di Laurea Magistrale in Fisica

Hadron spectra measurement in Xe–Xe collisions at $\sqrt{s_{\mathrm{NN}}} = 5.44$ TeV with the ALICE experiment at the LHC

Relatore:
Prof. Silvia Arcelli

Correlatore:
Prof. Francesco Noferini

Presentata da:
Simone Ragoni

Anno Accademico 2017/2018

Contents

Abstract

In late 2017, the ALICE collaboration recorded data from Xe–Xe collisions at the unprecedented energy in nucleus-nucleus AA systems of (centre of mass energy per nucleon pair) $\sqrt{s_{\mathrm{NN}}} = 5.44$ TeV. The (transverse momentum) p_{T}-spectra at mid-rapidity ($|y| < 0.5$) of pions, kaons and protons are presented. The final p_{T}-spectra are obtained by combining independent analyses with the Inner Tracking System (ITS), the Time Projection Chamber (TPC), and the Time-Of-Flight (TOF) detectors. This thesis focuses on the analysis performed with TOF and on the performance of the special Xe–Xe run conditions. The peculiarity of these data comes also from the experimental setup: because of the lower magnetic field ($B = 0.2$ T, lower than the usual 0.5 T) we expect to explore a p_{T} region unattainable before. A comparison between the yields at different centrality bins will also be provided.

Abstract

Nell'autunno del 2017 la Collaborazione ALICE ha registrato dati da collisioni Xe–Xe all'energia mai vista prima in collisioni nucleo-nucleo AA di (energia nel centro di massa per coppia di nucleoni) $\sqrt{s_{\mathrm{NN}}} = 5.44$ TeV. Gli spettri in impulso trasverso a rapidità centrale ($|y| < 0.5$) di pioni, kaoni e protoni sono presentati. Tali spettri nella loro forma definitiva sono ottenuti combinando analisi indipendenti sui dati dell'Inner Tracking System (ITS), della Time Projection Chamber (TPC), e del Time-Of-Flight (TOF). Questa tesi si focalizza sull'analisi compiuta con il TOF e sulle prestazioni ottenute sulle speciali condizioni sperimentali in collisioni Xe–Xe. La peculiarità di questi dati deriva dalla presenza di un campo magnetico più basso del solito ($B = 0.2$ T contro i soliti 0.5 T); dunque ci si aspetta di poter esplorare una regione in p_{T} non raggiungibile prima. Un confronto tra gli spettri a differenti classi di centralità sarà pure fornito.

Introduction

It is a widespread belief that accelerator physics has been aiming only to complete the Standard Model. In 2012 the Higgs boson was discovered, and scientists are probing its properties. Searches for physics beyond the Standard Model are going on, but no new physics has been currently unearthed. Thankfully, this is not the only aim of the many research facilities. Nowadays a lot of effort is spent for the Quark-Gluon Plasma (QGP). It has been predicted that a new state of matter, the QGP, could be formed under extreme conditions, like the highest barionic densities or at the highest temperatures. Its peculiarity is that quarks and gluons will be in a deconfined state. Probes have been identified that could help us in understanding the properties of this short-lived state.

One basic question: does the QGP exist? All the results hint to its existence, so we must persevere and continue this line of work. Currently the state of the art in this field is the ALICE experiment. This is the experiment at the LHC facility, best equipped for this kind of work. It has everything we need: the best PID (Particle IDentification) capabilities among all the current LHC experiments, great multiplicity management, and the record holder in TPC (Time Projection Chamber) construction. A massive project, mostly focusing on heavy ion collisions, but without disregarding more traditional collision systems, like the pp collisions. Usually ALICE is linked to Pb–Pb collisions only, but as it has just been said, this is not true: pp, p–Pb, Pb–Pb collisions, and a 8 hours run on Xe–Xe collisions. In the future LHC could be possibly running argon too!

In my master thesis I have analyzed the Xe–Xe data to extract pion, kaon and proton spectra. Hydrodynamics suggests that the p_{T}-spectra of the pions, kaons and protons produced after

the QGP has been produced, could aid in understanding its properties. What happens is that the latter stages of the heavy ion collision, namely the chemical and kinetical freeze-out, freeze the particle species and their energies, respectively. We measured the spectra and the yield ratios for different species, sticking only to π, K and protons, both particles and antiparticles. The focus is on the measurements performed with the Time-Of-Flight (TOF) system currently installed inside ALICE, providing data for the p_{T}-region $0.4 < p_{\mathrm{T}} < 4$ GeV/c, and if we imagine a thermal production it is not too farfetched to imagine a Maxwellian production, so this range covers most of the particle production. The spectra found in this thesis actually cover a larger range than what it is expected for a TOF only analysis (the one I have been involved with). This is because they are combined spectra, made from different people working on the same analysis but with different subdetectors of the ALICE experiment.

This thesis is organized as follows: after a brief account of the theory of QGP itself with the probes generally used, comes a description of the whole ALICE apparatus, with a focus on the TOF. Right after a description of the analysis comes an account of the main results. More miscellaneous stuff has been put inside the appendices. Right at the end, before the bibliography, a small acknowledgement section can be found and that closes this work.

Chapter 1

The Physics of QGP

Over the years, nuclear collision energies have increased from beam kinetic energies of a few MeV per nucleon on fixed targets in small laboratories to, at present, collider energies at large laboratories with international collaborations. As the energy is increased, the relevant degrees of freedom change. At the lowest energies, the nucleus may remain intact or be broken up into light nuclear fragments. As various thresholds for particle production are reached, some of the energy of the system may go into producing new particles, such as pions or kaons. At high enough energies, the relevant degrees of freedom are expected to be quarks and gluons rather than hadrons, forming the quark-gluon plasma [1].

1.1 Introduction

Based on lattice QCD studies there is a change in the state of matter (a phase transition) from a hadronic system to a nearly free gas of quarks and gluons, the quark-gluon plasma. Thus we may consider the phase transition between the quark-gluon plasma and the hadronic world.

The phase transitions in nuclear matter can be compared to those in water to have a visual impact as clear as possible. The phase diagram of water is shown in Fig. 1.1. The lines on

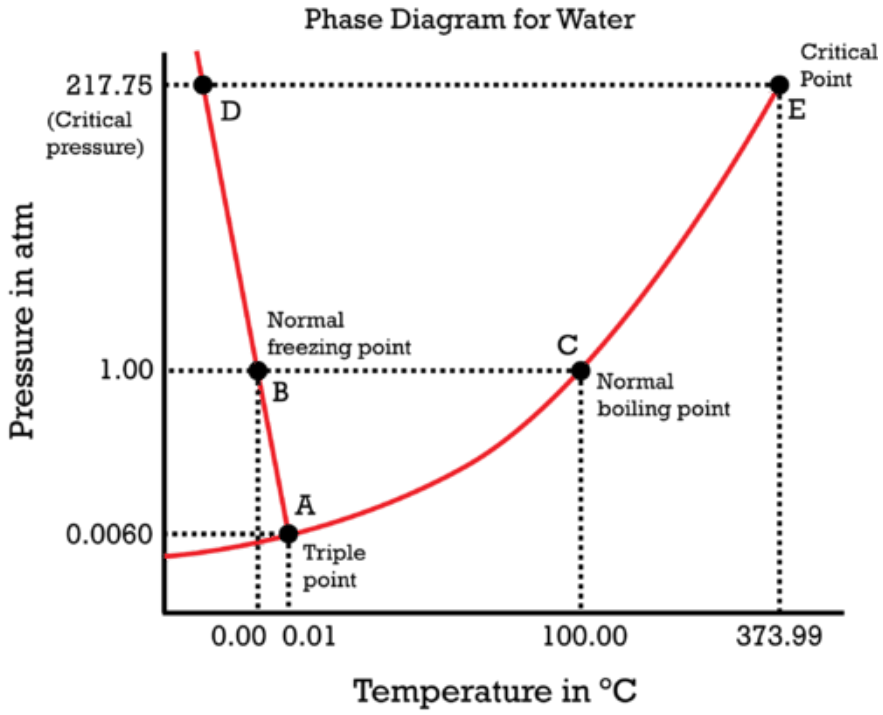

Figure 1.1: A simplified phase diagram of water.

the diagram are where the phases coexist with each other. In our everyday experience, at one atmosphere of pressure the solid, liquid and gas phases can coexist. Examples of such coexistence in water are ice in a glass of water (solid/liquid coexistence) and steam over a pot of boiling water (liquid/gas coexistence). At the coexistence point, the temperature does not change but the volume of the system can increase. For example, the steam rising from boiling water escapes into a much larger volume since the gas phase fills the available space. Water can keep boiling away with steam rising off it until all the water in the pot is gone. Likewise, the temperature of the glass of ice water does not change until the ice is melted, at which point the temperature begins to increase. These changes in water are the manifestations of a first-order phase transition.

In a first-order phase transition, while the two phases coexist, the pressure, temperature and chemical potential are equal at the phase boundary. There is, however, a discontinuity in the energy density of the two phases before and after the transition. This discontinuity, the latent heat of the transition, is characteristic of first-order phase transitions. Not all phase transitions have a discontinuity in the energy density across the transition and are

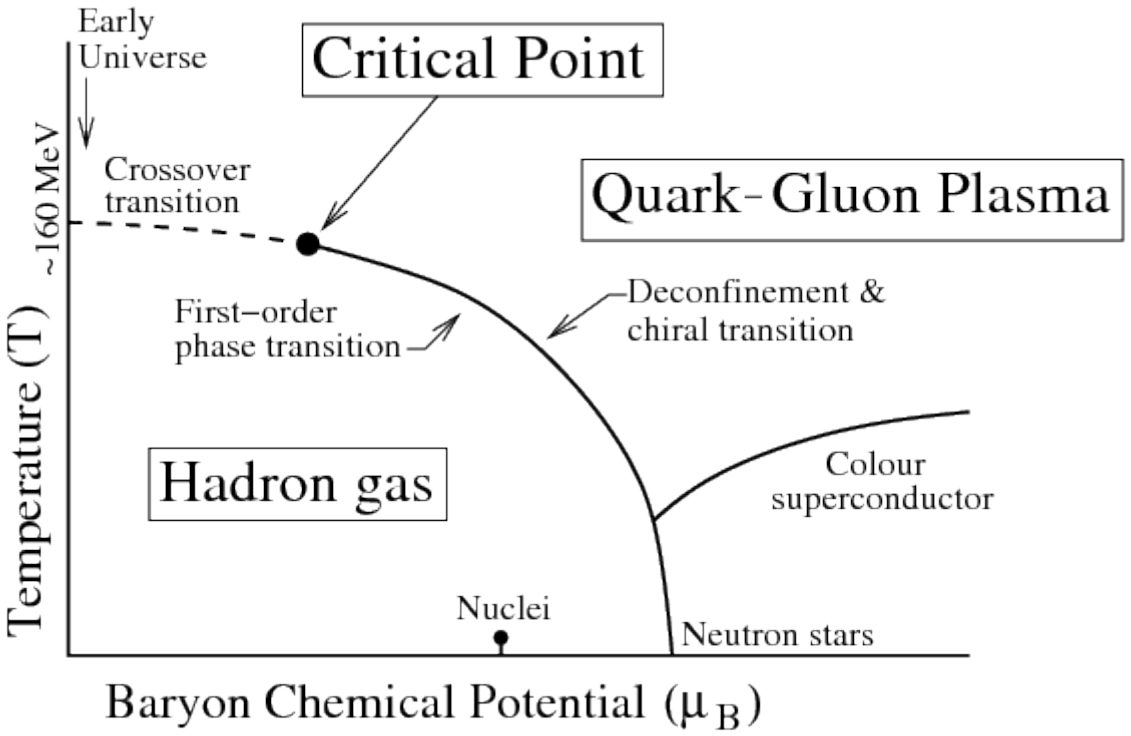

Figure 1.2: A simplified phase diagram for the QGP.

thus not of the first-order type. In these instances what happens is that the order of the transition is given by the first derivative that shows a discontinuity, and if otherwise they are all continuous a cross-over is instead obtained. All transitions higher than first order involve no latent heat.

In nuclear matter, several phases exist as well. At zero temperature we have normal nuclear matter with an energy density of $\rho \approx 0.16$ GeV/fm^3 for a nucleon at rest. The quark matter phase can be reached either by compressing nuclear matter to high densities at rather low temperatures (along the baryon density axis) or by heating the vacuum (along the temperature axis). The high density phases are expected to play a key role in the interior of neutron stars. On the other hand, the high temperature, heated-vacuum quark-matter phase was first produced in nature shortly after the Big Bang. The line of first-order transitions, see Fig. 1.2, ends on the higher temperatures part with $\mu_B \neq 0$, indicated on the diagram by the label *critical point*.

Phase transitions in nuclear matter involve symmetries. In the early universe, the quarks

were massless and there was an equal number of quarks and antiquarks. In the universe today, after the transition to normal nuclear matter, there is a small difference in the up and down quark masses, as well as an even larger difference between the light quark masses and those of the other quarks, even between the light quarks and the strange quark. This mass difference is caused by chiral symmetry breaking. However, at high temperatures chiral symmetry is expected to be restored. Today's universe is baryon dominated with quarks bound into normal matter with antibaryons far from our everyday experience and they must be produced in the laboratory. We expect to find an equal number of quarks and antiquarks produced in the central rapidity region in heavy-ion collisions. LHC, as RHIC had already done, enables us to investigate the low densities, high temperatures part of the diagram.

1.2 A heuristic approach to the probing tools for the QGP

Later on, a bit of introduction to Lattice QCD will be provided too to explain some of the properties of the QGP, but for now a clear and simple image of what is going on here could possibly aid in understanding the following. As such a simple yet intuitive and exhaustive model is needed.

So, let us consider the following *gedankenexperiment*: a volume of unknown strongly interacting matter is undergoing a process to help it increase its energy density. We have many tools at our disposal to investigate it:

- hadron radiation
- electromagnetic radiation
- dissociation of a passing quarkonium beam
- energy loss of a passing jet.

First of all, we note that the unknown medium radiates, since its temperature is much higher than that of its environment. Hadron radiation means that we study the emission of hadrons consisting of light (u, d, s) quarks; their size is given by the typical hadronic scale of about 1 fm = $\frac{1}{200\ \mathrm{MeV}}$ (in natural units, $h = c = 1$). Since they cannot exist inside a deconfined medium, they are formed at the transition surface between the QGP and the physical vacuum. The physics of this surface is independent of the interior because the transition from deconfinement to confinement occurs at T_C, no matter how hot the QGP initially was or still is in the interior of our volume [2, 3, 4, 5, 6]. This is similar to having hot water vapour inside a glass container kept in a cool outside environment: at the surface, the vapour will condense into liquid, at a temperature of 100 degrees, no matter how hot it is in the middle. If the medium has a very high energy density and can expand freely, then this expansion will lead to a global hydrodynamic flow [7, 8, 9], giving an additional overall boost in momentum to the produced hadrons: they will experience a *radial flow* depending on the initial energy density. Moreover, if the initial conditions were not spherically symmetric, as in peripheral heavy-ion collisions (see also Appendix A), the difference in pressure in different spatial directions will lead to a further directed or *elliptic flow*, see Fig. 1.3. Since both forms of flow depend on the initial conditions, flow studies of hadron spectra could possibly provide information about the earlier stages.

The hot medium also radiates electromagnetically, i.e. it emits photons and dileptons (e^+e^- and $\mu^+\mu^-$ pairs) [10, 11]. Since the photons and leptons interact only electromagnetically, once they are formed they will leave the medium without any further interactions. Hence their spectra provide information about the first phases of the medium. Photons and dileptons thus do provide a possible probe of the hot QGP. The only problem is that they can be formed anywhere and at any time, even at the cool surface or by the emitted hadrons. The task in making them a viable tool is therefore the identification of the hot thermal radiation emitted by the QGP. Both electromagnetic and hadronic radiations are emitted by the medium itself, and they provide some information about the state of the medium at the time of emission.

Another possible approach is to test the medium with an external probe, and here we have

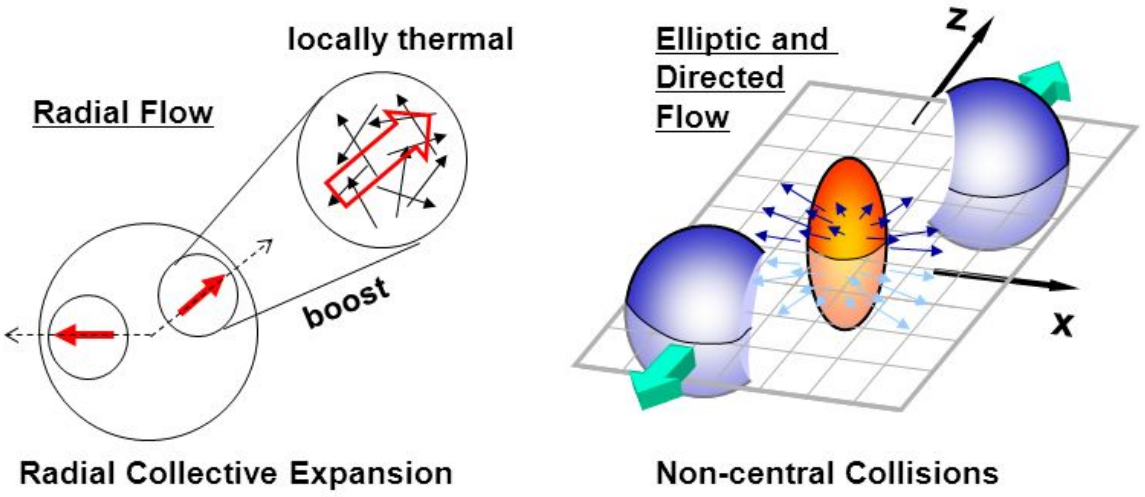

Figure 1.3: Example of radial and elliptic flow.

two so far quite successful examples, quarkonia and jets. Quarkonia are a special kind of hadrons, bound states of a heavy (c or b) quark and its antiquark. For the J/ψ and Υ the binding energies are around 0.6 and 1.2 GeV, respectively, and thus much larger than the typical hadronic scale 0.2 GeV; as a consequence, they are also much smaller, with radii of about 0.1 and 0.2 fm. It is therefore expected that they can survive inside a quark-gluon plasma through some range of temperatures above T_C [12, 13]. The higher excited quarkonium states are less tightly bound and hence larger. Since deconfinement is related to colour screening, the crucial quantity for dissociation of a bound state is the relation of binding to screening radius. We therefore expect that the different charmonium states, as an example, have different "melting temperatures"in a quark-gluon plasma. Hence the spectral analysis of in-medium quarkonium dissociation could provide a QGP thermometer [14].

So we could possibly shoot charmonia beams inside our medium to probe its temperature by analyzing which ones have survived [15]. Another possible probe is to shoot an energetic parton, quark or gluon, into our medium to be tested. How much energy it loses when it comes out on the other side will tell us something about the density of the medium [16, 17, 18, 19]. In addition, for quarks, the amount of jet quenching is predicted to depend on the mass of the quarks. In heavy-ion collisions, we have to create the probe in the same collision in which

we create the medium. Quarkonia and jets (as well as open charm/beauty and very energetic dileptons and photons) constitute the so-called hard probes, whose production occurs at the very early stages of the collision, before the medium is formed; they are therefore present when it appears. Moreover, their production involves large energy or momentum scales and can be calculated by perturbative QCD techniques and tested also in pp and p–A collisions.

1.3 At LHC

All the results shown in the following hold only in the extreme condition of $\mu_B \simeq 0$ [20]. However, this is exactly what we are looking for. The quantity μ_B, or the *bariochemical potential*, is at the first order an index representing the barion-antibarion asimmetry, meaning the closer we are to 0, the more is the production of barions and antibarions equal. But this is what we expect to find at LHC. At LHC energies, meaning $\sqrt{s_{\mathrm{NN}}} \approx 5 - 5.5$ TeV both at Pb–Pb and Xe–Xe collisions, the initial valence quarks constitute a mere 5% of the total quark density, implying a small value of μ_B. Instead, the other optimal natural laboratory is what we should find in neutron stars, so the highest possible values of μ_B.

Nowadays the scientific community is more inclined towards the cross-over style of transition, as it requires the lowest possible values of μ_B.

What happens at LHC in heavy-ion collisions is the following:

1) an initial period of matter compression and heating occurs during the interpenetration of the projectile and target baryon density distributions. Inelastic processes occurring at the microscopic level convert initial beam longitudinal energy to new internal and transverse degrees of freedom, by breaking up the initial baryon structure functions. Their partons thus acquire virtual mass, populating transverse phase space in the course of inelastic perturbative QCD shower multiplication. This stage should be far from thermal equilibrium;

2) inelastic interactions between the two arising parton fields (opposing each other in

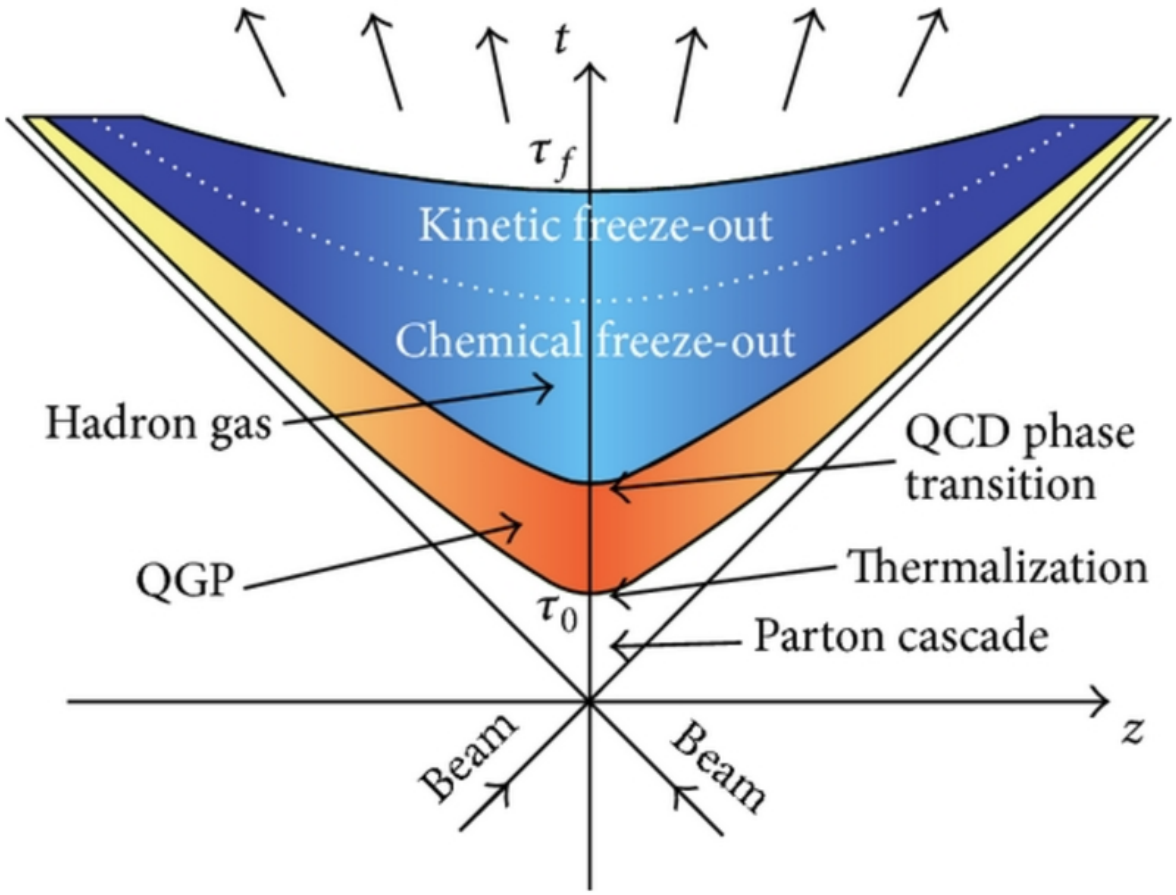

Figure 1.4: A schematic view of dynamics of a heavy-ion collision along the collision axis.

longitudinal phase space) should lead to a pile-up of partonic energy density centered at mid-rapidity (the longitudinal coordinate of the overall center of mass). Due to this mutual stopping down of the initial target and projectile parton fragmentation showers, a slowdown of the time scales governing the dynamical evolution should occur and equilibrium could possibly be approached here;

3) QGP undergoes system expansion and decay. Therefore hadrons and hadronic resonances form [21, 22], decoupling swiftly from further inelastic transmutation so that their yield ratios become stationary, the *freeze-out* [23]. A final expansion period dilutes the system until strong interaction ceases altogether, see Fig. 1.4.

We can assign a time to the many stages of the fireball evolution. Thermalization happens

somewhere around 0.6 fm/c [24]. During the expansion the particle species abundances get fixed - *chemical freeze-out* - with a time scale of $\approx$ 10 fm/c, before finally getting to the point where the particles do not interact anymore - *kinetic freeze-out* - at around 15 fm/c.

1.4 Hydrodynamics

So, eventually, expansion leads to a free-streaming stage through freeze-out and particle spectra at this moment are seen by the detector. Hydrodynamics is applied to matter under local equilibrium in the intermediate stage. It is a useful strategy to employ if we take into consideration the difficulties connected to QCD.

A lot of experimental data have been published so far at various collision energies. Ideally, we may want to describe these data from first principles, i.e. quantum chromodynamics (QCD). The QCD Lagrangian density is:

$$\mathcal{L}_{\mathrm{QCD}} = \bar{\psi_i}\left(i\gamma_\mu \mathcal{D}^\mu_{ij} - m\delta_{ij}\right)\psi_j - \frac{1}{4}F_{\mu\nu\alpha}F^{\mu\nu\alpha} \ , \tag{1.1}$$

where ψ_i is a quark field, $i = 1, 2, 3$ the color index and $\mathcal{D}^\mu$ is a covariant derivative, m the quark mass, $F^{\mu\nu\alpha}$ the field strength for the gluons, and α cycles over the colour for the gluons. Despite its simple-looking Lagrangian, it is very difficult to make any predictions directly from QCD in heavy-ion collisions due to its complexity which mainly arises from non-linearity of interactions of gluons, strong coupling, dynamical many-body system, and colour confinement. One promising strategy to connect the first principles with phenomena is to introduce hydrodynamics as a phenomenological theory. An input to this phenomenological theory comprises the equation of state:

$$P \equiv P(e, n) \ , \tag{1.2}$$

expressing the pressure P as a function of energy density e and baryon density n. This can be obtained by exploiting lattice numerical simulations of QCD. In the case of viscous hydrodynamics we need additionally the transport coefficients such as shear viscosity η, bulk viscosity ϵ , heat conductivity λ. Once hydrodynamics turns out to work quite well in the

description of dynamics, we may utilize its outputs such as local temperature or energy density for other observables. In the current formalism of jet quenching, an information of parton density or energy density along a trajectory of an energetic parton is needed [25, 26]. If we assume that the J/ψ melts above some temperature [27], the local temperature at its position is needed. Hydrodynamics provides us with the information of the bulk matter. Therefore we can say that, in this field, hydrodynamics is the heart of the dynamical modeling: it not only describes expansion and collective flow of matter but also provides important information in the intermediate stage for other phenomena.

Basic equations: The basic hydrodynamical equations [28, 29, 30] are energy-momentum conservation:

$$\partial_\mu T^{\mu\nu} = 0 \ , \tag{1.3}$$

with $T^{\mu\nu}$ being the energy-momentum tensor itself and the current conservation

$$\partial \mathcal{N}_i^\mu = 0 \ , \tag{1.4}$$

where $\mathcal{N}_i^\mu$ are the conserved currents. We expect to have a few conserved charges like the baryon number, strangeness, electric charges and so on, but generally we refer to the baryon current $\mathcal{N}_B^\mu$. These few tensors and currents may be decomposed [31, 32] as:

$$T^{\mu\nu} = e u^\mu u^\nu - P\Delta^{\mu\nu} + W^\mu u^\nu + W^\nu u^\mu + \pi^{\mu\nu} \ ,$$

$$\mathcal{N}_i^\mu = n_i u^\mu + V_i^\mu \ ,$$

with $u_\mu u^\mu = 1$ and the tensor $\Delta^{\mu\nu}$ defined as:

$$\Delta^{\mu\nu} = g^{\mu\nu} - u^\mu u^\nu .$$

Usually we refer to u^μ as the *local flow four-velocity* and it is perpendicular to $\Delta^{\mu\nu}$ as:

$$u_\mu \Delta^{\mu\nu} = u_\mu \left(g^{\mu\nu} - u^\mu u^\nu \right) = 0.$$

The quantities defined above are [33, 34]:

- **energy density** $e = u_\mu T^{\mu\nu} u_\nu$

- **hydrostatic and bulk pressure** $P = P_s + \Pi = -\frac{1}{3}\Delta_{\mu\nu}T^{\mu\nu}$
- **energy current** $W^\mu = \Delta^\mu_\alpha T^{\alpha\beta}u_\beta$
- **shear stress tensor** $\pi^{\mu\nu} = \langle T^{\mu\nu}\rangle$

with

$$\langle T^{\mu\nu}\rangle = \left[\frac{\Delta^\mu_\alpha\Delta^\nu_\beta + \Delta^\mu_\beta\Delta^\nu_\alpha}{2} - \frac{\Delta^{\mu\nu}\Delta_{\alpha\beta}}{3}\right]T^{\alpha\beta}.$$

Equations of motion: Contracting [35, 36] Eq. 1.3 with u^ν and $\Delta_{\mu\alpha}$ we obtain:

$$u_\nu\partial_\mu T^{\mu\nu} = 0\ , \tag{1.5}$$

$$\Delta_{\mu\alpha}\partial_\beta T^{\alpha\beta} = 0\ , \tag{1.6}$$

giving out

$$\dot{e} = -\left(e + P_s + \Pi\right)\theta + \pi_{\mu\nu}\langle\Delta^{\mu\alpha}\partial_\alpha u^\nu\rangle\ ,$$

and

$$\left(e + P_s + \Pi\right)\dot{u}^\mu = \Delta^{\mu\alpha}\partial_\alpha\left(P_s + \Pi\right) - \Delta^{\mu\alpha}\Delta^{\beta k}\partial_k\pi_{\alpha\beta} + \pi^{\mu\alpha}\dot{u}_\alpha\ ,$$

with $\theta = \partial_\mu u^\mu$ the *divergence of the flow* and the dot notation $\dot{x}^\mu = x_\mu\partial^\mu$.

To solve the hydrodynamic equations we introduce the following two phenomenological definitions [37], the so-called constitutive equations, for the shear stress tensor $\pi^{\mu\nu}$ and the bulk pressure Π:

$$\pi^{\mu\nu} = 2\eta\langle\Delta^{\mu\alpha}\partial_\alpha u^\nu\rangle$$

$$\Pi = -\epsilon\partial_\mu u^\mu = -\epsilon\Delta^{\mu\alpha}\partial_\alpha u_\mu$$

obtaining by substitution:

$$\dot{e} = -e\theta - P_s\theta + \frac{\Pi^2}{\epsilon} + \frac{\pi_{\mu\nu}\pi^{\mu\nu}}{2\eta} = -e\theta - P_s\theta + \frac{\Pi^2}{\epsilon} + \epsilon(-\theta)^2 + 2\eta\langle\Delta^{\mu k}\partial_k u^\nu\rangle^2.$$

The first term on the right-hand side describes dilution and compression of the energy density due to the change of the volume (θ can be parametrized as $\dot{V}/V$ with V the volume of the fluid element). If the system expands ($\theta > 0$), the energy density is diluted. So the effect

of expansion appears as a negative source term $-e\theta$ inside the equation. If we move along with a fluid element, the internal energy in the fluid element is not conserved due to the work done by pressure, which is described by the second term. Finally, the last two positive addends represent the production of entropy which heats up the system.

1.5 Lattice QCD in a nutshell

A method is needed to reliably compute the thermodynamic quantities in the non-perturbative regime of QCD, necessary to determine the order of the phase transition and the critical temperature. Lattice gauge theory has proven to be a useful way to do this, especially as computing power has continued to improve. In Lattice QCD, the thermodynamic partition function is related to the path integral formulation of quantum mechanics. In Euclidean space, with imaginary time, the action, S_E, is related to the Hamiltonian operator in the partition function and the imaginary time is related to the inverse temperature.

QCD is asymptotically free at short distances where perturbative calculations are possible. However the large momentum scales, corresponding to short distances, may cause divergences in the momentum integrations. These types of divergences are called *ultraviolet divergences*. In perturbation theory these divergences are handled using renormalization group methods. In non-perturbative QCD, the perturbative expansion is no longer valid and another way to handle the divergences is required. Lattice gauge theory reformulates QCD on a lattice of discrete space-time points. The spacing between lattice points provides a finite distance scale. This lattice spacing gives a minimum distance and thus also a maximum momentum scale which acts as a momentum cut off in the integrations. Hence terms that would become infinite remain finite. However, the result for any quantity calculated in the lattice depends on the *lattice spacing*, a. The way to remove this dependence is to perform the same calculation multiple times with different, decreasing, a.

The quantum mechanical description of the relationship between the partition function and the evolution of a system comes about in the path integral formulation developed by Feyn-

man. The path integral approach generalizes the classical action. In classical terms, there is a well-defined way of moving from point A at location x_a and time t_a to point B at x_b and t_b. Quantum mechanically, however, there are an infinite number of ways to get from A to B. Feynman proposed several postulates for the path-integral formalism [38]. The probability is given by the absolute square of a complex amplitude. The amplitude of an event is obtained by summing all paths that include that event. The weight of a particular space-time path or history as sometimes it is called, is proportional to $\exp\left[iS(\mathcal{L})\right]$ where $S(\mathcal{L})$ is the action (time integral of the Lagrangian) for that path. The proportionality factor is determined by normalizing to the square root of the total probability so that the the total probability from all normalized amplitudes is unity. The probability amplitude is integrated over all possible histories, no matter how indirect or absurd. The path integral assigns equal amplitudes to all histories, no matter how unlikely they may seem. Only the phase differs. The more strange paths will be suppressed. In the limit where the action is large, the path integral is dominated by solutions that are stationary points of the action since amplitudes with similar histories will constructively interfere, while instead the complex phases for histories far from the stationary points will vary rapidly, leading to destructive interference. Thus the most significant histories are the classical solutions to the Euler-Lagrange equation, recovering classical mechanics.

The math is as following: the amplitude is given by summing all paths that satisfy the criteria and is proportional to the weight, $\exp[iS_M]$, for that path, where S_M is the usual action $S_M[\mathcal{L}] = \int_{t_a}^{t_b} \mathcal{L} dt$, so that quantum mechanically this means that the time evolution in terms of the Hamiltonian H is:

$$\langle x_b, t_b | \exp\left[-H(t_b - t_a)\right] | x_a, t_a \rangle = \sum_{\text{all paths}} \exp\left(iS_M\right), \tag{1.7}$$

and we undergo time slicing to discretize this integral, by evaluating at multiple steps. The final step is to link this all to the partition function Z resulting in:

$$Z = \mathrm{Tr} \exp\left(-H/T\right) \equiv \langle x_a, t_a | \exp\left[-H/T\right] | x_a, t_a \rangle = \sum_{\text{all paths}} \exp\left(iS_M\right) = \\ = \int Dx \exp\left(iS_M\right) = \int Dx \exp\left(-S_E\right),$$

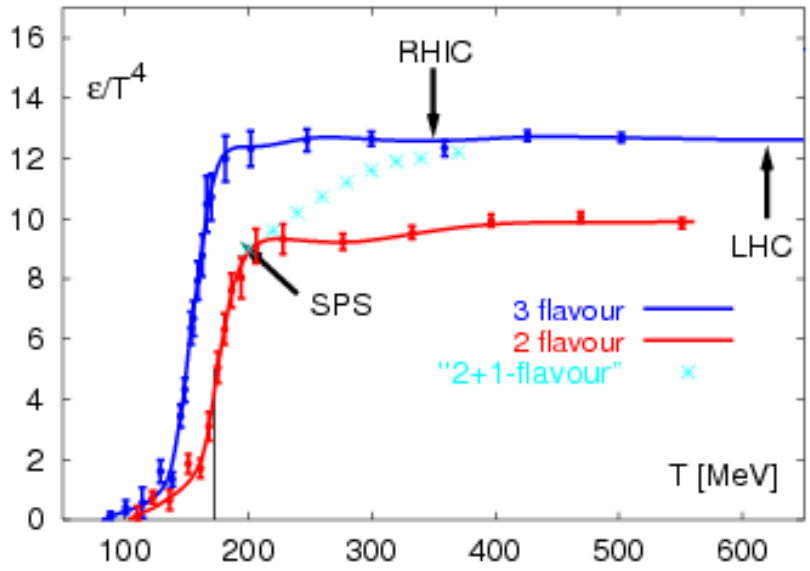

Figure 1.5: Energy density as computed with Lattice QCD. The trend is dependent on the number of light quarks. The energy densities at SPS, RHIC and LHC are plotted too.

where the last equivalence is obtained by Wick rotating the time coordinates. The same can be translated to field theory.

LQCD results: What is usually studied via Lattice QCD means is for instance, the $Q\bar{Q}$ potential between quarks, along with confinement, or the opposite problem with chiral symmetry restoration. It is shown that should three flavours be involved inside the number of the light quarks, the transition to the QGP phase would be of the first-order type, while it would be of the second-order for two flavours. Through Lattice QCD studies, the energy density against the temperature of such a system can be computed too. The energy density depends on the number of light quarks as it is shown in Fig. 1.5. Noteworthy is that the critical temperature for the transition is lower with three flavours if compared to the two flavours case.

1.6 A simple model for T_C

The actual value of T_C, the critical temperature for the QGP, is not well defined as of yet. While the order of magnitude of this quantity is known and it is common to say $T_C \approx m_\pi$ where m_π is the pion mass, with an upper limit of $T_C < 200$ MeV, the reason is not as obvious. A very simple model to provide an explanation of said value is shown in the following, although refinements are needed to lower it to the $T_C = 156$ MeV usually found [39].

For an ideal gas of massless pions, the pressure as a function of the temperature is given by the Stefan-Boltzmann form:

$$P_\pi = \frac{3\pi^2}{90} \cdot T^4 \tag{1.8}$$

where the factor 3 accounts for the three charge states of the pion. The corresponding form for an ideal quark-gluon plasma with two flavours and three colours is:

$$P_{\mathrm{QGP}} = \left[2 \times 8 + \frac{7}{8} \cdot (3 \times 2 \times 2 \times 2)\right] \frac{\pi^2}{90} \cdot T^4 - B = \frac{37\pi^2}{90} \cdot T^4 - B \tag{1.9}$$

where the first temperature term in the square brackets accounts for the two spin and eight colour degrees of freedom of the gluons, the second for the three colour, two flavour, two spin and two particle and antiparticle degrees of freedom of the quarks, with 7/8 to obtain the correct statistics. The bag pressure B takes into account the difference between the physical vacuum and the ground state for quarks and gluons in a medium. Since in thermodynamics, a system chooses the state of lowest free energy and hence highest pressure, we compare in Fig. 1.6a the temperature behaviour of the above equations. this simple model thus leads to a two-phase picture of strongly interacting matter, with a hadronic phase up to:

$$T_C = \left(\frac{45}{17\pi^2}\right)^{1/4} \cdot B^{1/4} = 0.72 \cdot B^{1/4} \approx 150 \text{ MeV} \tag{1.10}$$

this is because certain experimental results [41] point towards a bag value

$$B^{1/4} \approx 0.2 \text{ GeV},$$

and we could expect a QGP phase right above this threshold. The energy densities are [42]:

$$\epsilon_\pi = \frac{\pi^2}{10} \cdot T^4, \qquad \epsilon_{\mathrm{QGP}} = \frac{37\pi^2}{30} \cdot T^4 + B.$$

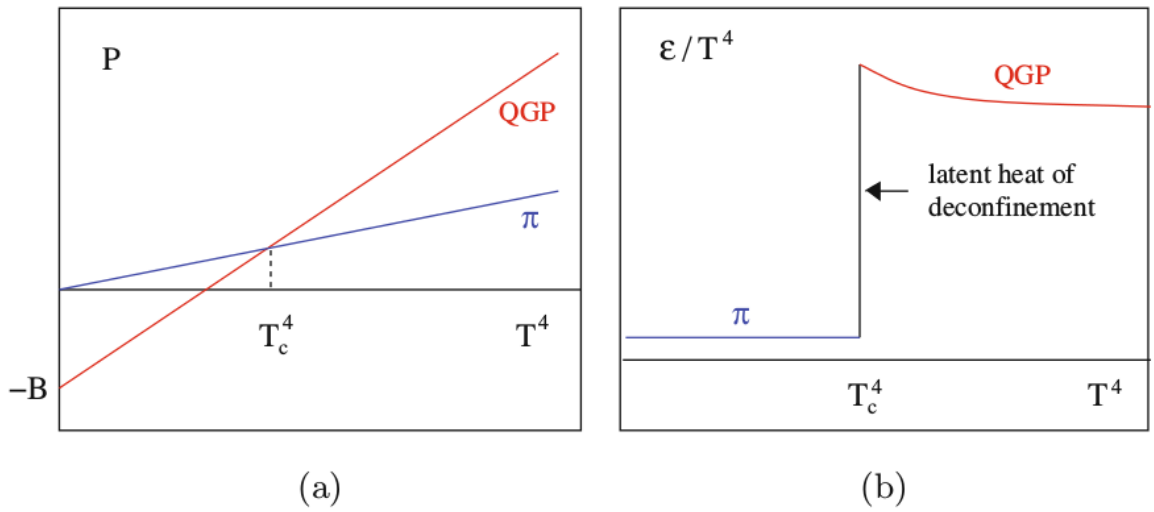

Figure 1.6: Pressure and energy density in the simplified model [40].

Please note that such a model involves only a first phase transition. Actually, whether we have a first phase transition, a second phase transitions or a cross-over is not established at the moment, although nowadays it seems that at LHC the latter two and especially the last are more likely.

1.7 A few powerful investigation tools

Before moving on, it is possible to highlight a few powerful tools that are helpful in investigating the hydrodynamical properties of the QGP, especially considering that we would like to know whether the system produced in heavy-ion collisions could possibly be described by thermodynamical quantities [43, 44, 45, 46, 47, 48, 49, 50]. The first is the transverse momentum or transverse mass distribution of produced particles. The slope of the distribution includes contributions from the freeze-out temperature and the radial expansion velocity. Following right on, the particle chemistry. Then we can discuss the azimuthal distribution. Pressure gradients within the participant matter develop into an azimuthally anisotropic flow pattern which is discernible in the final state.

Particle spectra One way to quantify the expansion (fluid) velocity of the system produced in heavy-ion collisions is to study the distributions of the produced particles, particularly the transverse momentum distribution with the invariant rate:

$$E\frac{dN}{d^3p} = \frac{dN}{\pi dy dp_{\mathrm{T}}^2}.$$

The final-state distribution is governed by the temperature at which the system freezes out and the particles no longer interact. If the values of the temperature agree for different particle species, e.g. pions, kaons, protons and antiprotons, this indicates a global freeze-out temperature and fluid velocity. When no expansion is assumed, a global temperature cannot necessarily be identified for all particle species. It could possibly be useful to remind that the low p_{T} end of the spectrum involves particles which are more likely to be in thermal equilibrium (being at low p_{T}). High p_{T} particles are more likely to have been produced in hard scatterings, governed by perturbative QCD. However, it must be remarked that while high p_{T} particles may not come to thermal equilibrium, they are still affected by the surrounding medium.

To further quantify the effects of the hot, dense matter on the transverse momentum distributions, a reference spectrum at the same energy, within the same rapidity range, would be useful. Data from pp collisions are often used as reference spectra since they contain no nuclear effects. At high p_{T}, perturbative QCD can be used to calculate the pp result rather accurately, making it a useful reference distribution. The ratio of the A–A result to the reference pp result at the same energy is denoted R_{AA}, see Eq. 1.11 and Fig. 1.7.

$$R_{\mathrm{AA}}\left(p_{\mathrm{T}}\right) = \frac{\frac{1}{N_{\mathrm{events}}^{\mathrm{AA}}}\frac{d^2N_{\mathrm{charged}}^{\mathrm{AA}}}{d\eta dp_{\mathrm{T}}}}{\langle N_{\mathrm{collisions}}\rangle N_{\mathrm{events}}^{\mathrm{pp}}\frac{d^2N_{\mathrm{charged}}^{\mathrm{pp}}}{d\eta dp_{\mathrm{T}}}} \tag{1.11}$$

The measurement of the R_{AA} is important because it is a way to ascertain if a nucleus-nucleus collision can be interpreted as a superposition of uncorrelated binary collisions between nucleons. It is also sensitive to the formation of a QGP phase: partons with high momentum tend to lose their energy by scattering with the medium, resulting in a suppression of the

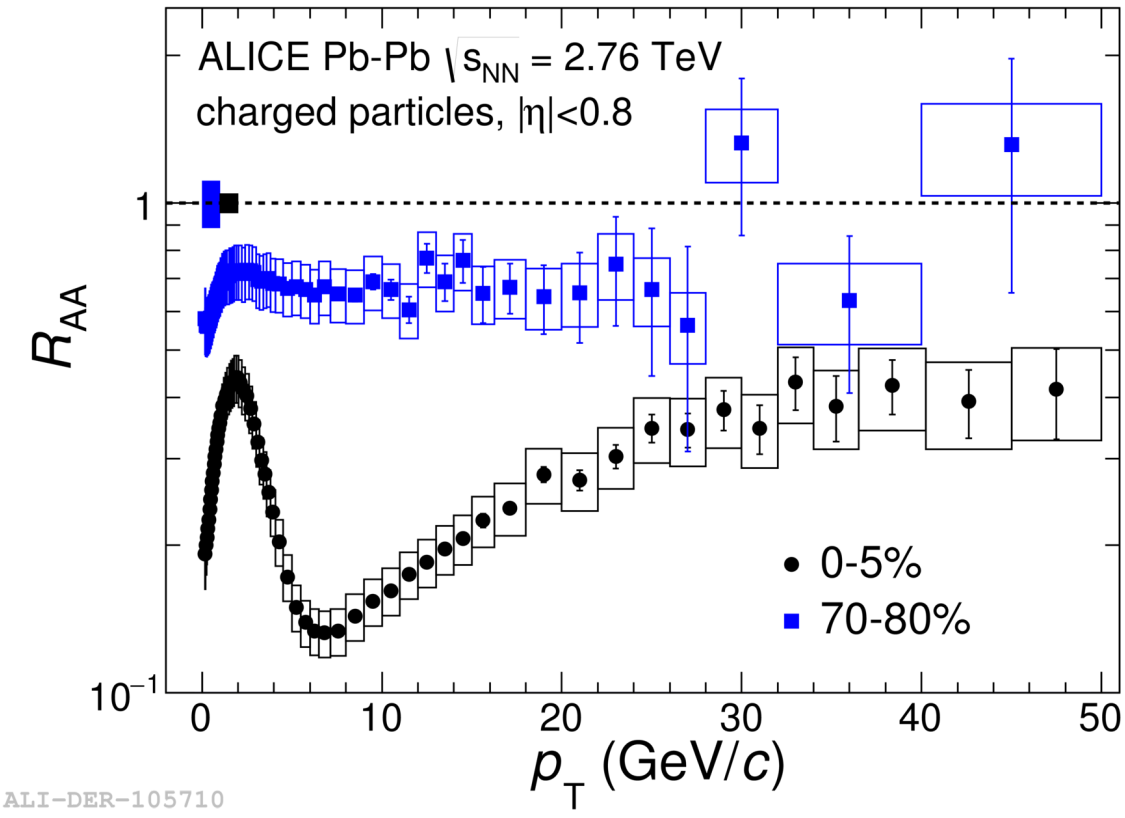

Figure 1.7: Example of R_{AA} [51] in p-Pb and Pb–Pb (two centrality classes involved).

high p_{T} component. With the nuclear modification factor the properties of the created medium can be studied by estimating the energy loss of hard partons. Two regimes are to be expected: *soft processes* dominate in the low p_{T} region (where the number of produced particles depends on the number of nucleons participating in the process, thus the R_{AA} should be lower than one, because in A–A collisions the number of participants should be vastly lower the number of collisions) while at high p_{T} hard processes (particle production depends on the number of nucleon-nucleon collisions, the R_{AA} is expected to be one if no nuclear effects are present). As can be seen in Fig. 1.7, the high p_{T} part is suppressed in central collisions.

Ultimately, this tool should check whether the matter reaches kinetic equilibrium. If we suppose a system in heavy-ion collisions is in kinetic equilibrium, the pressure is built inside the system. The matter is surrounded by vacuum, so pressure gradient in outward directions generates collective flow and, in turn, the system expands radially. The momentum distribution in kinetically equilibrated matter is isotropic. On the other hand, when the matter is moving at a finite velocity the momentum distribution is Lorentz boosted. If this kind of distortion in momentum distribution can be observed experimentally, one can obtain some information about kinetic equilibrium. Assuming each fluid element expands radially at radial flow velocity v_{T} , the p_{T}-spectra for pions and protons can be calculated by convoluting these distorted momentum distributions over azimuthal direction - the **blast wave model** [52, 53]. Here p_{T} is the transverse momentum which is perpendicular to the collision axis.

Particle chemistry The next basic check is whether the matter in heavy-ion collisions reaches chemical equilibrium. Assuming thermal and chemical equilibria, we can calculate the number density of a certain particle species using:

$$n_i(T,\mu) = \frac{g}{2\pi^2}\int_0^\infty \frac{p^2 dp}{\exp\left[\left(E_i-\mu_i\right)/T\right]\pm 1}$$

where n_i gives the number density of particle species i as a function of the temperature T and chemical potential μ_i, g is the degeneracy of the particle, p is the momentum, and E its energy. We further assume that the measured particle number is fixed at a certain temperature and chemical potential, which is called chemical freezeout. Then the average

number of particles, N_i, can be estimated by summing contribution from particles directly emitted from the system with volume V and contribution from resonance decays:

$$\langle N_i \rangle = V \left[n_i^{\mathrm{th}}(T, \mu) + \sum_R \Gamma_{R \to i} \cdot n_R(T, \mu) \right]$$

where n_i^{th} and n_R are the number density of directly emitted particle i and resonance R, respectively. $\Gamma_{R \to i}$ is the branching ratio of the resonance R decaying into species i. We can see, inside Fig. 1.8 [54], a remarkably good agreement with only these few parameters [55]. However, the models do not fully describe the data. The largest contribution to the χ^2/NDF comes from the low yield of protons relative to pions. This conclusion persists for the three different thermal model implementations which were used by the ALICE Collaboration, indicating that the residual differences in those models have a second order effect. Deviations for short-lived K^{*0} resonance that suffers from rescattering in the late hadronic phase are to be expected. Tensions between protons and multi-strange particles are probably due to an incomplete list of the particles involved that are to be included for the final fit [56, 57].

Azimuthally anisotropic collective flow (elliptic flow) In the hydrodynamic expansion following a heavy-ion collision, the matter develops a flow pattern. The flow pattern is related to the equation of state of the system through the dependence of the pressure (or energy per particle) on temperature and density. The phenomenon of this collective flow has been investigated over a wide range of energies, from tens of MeV per nucleon to the RHIC regime and now LHC's energies. To study flow in experiments, it is important to determine the reaction plane, a reference plane, of the collision. In Cartesian coordinates, the z unit vector is in the beam direction. The x unit vector lies in the direction of the impact parameter vector and forms the reaction plane with the z vector. The y unit vector is normal to the reaction plane. Particle rapidity, p_{T} and azimuthal angle with respect to the reaction plane can be determined from its motion. Basically, here with *collective flow* we mean the correlation between position of matter and direction of flow, which is not necessary to be hydrodynamically evolving matter. An example of what we have to study in this instance is shown inside the right side of Fig. 1.3: broadly speaking, we select only the few non-central collisions. In such a collision a region of the locally equilibrated state can be

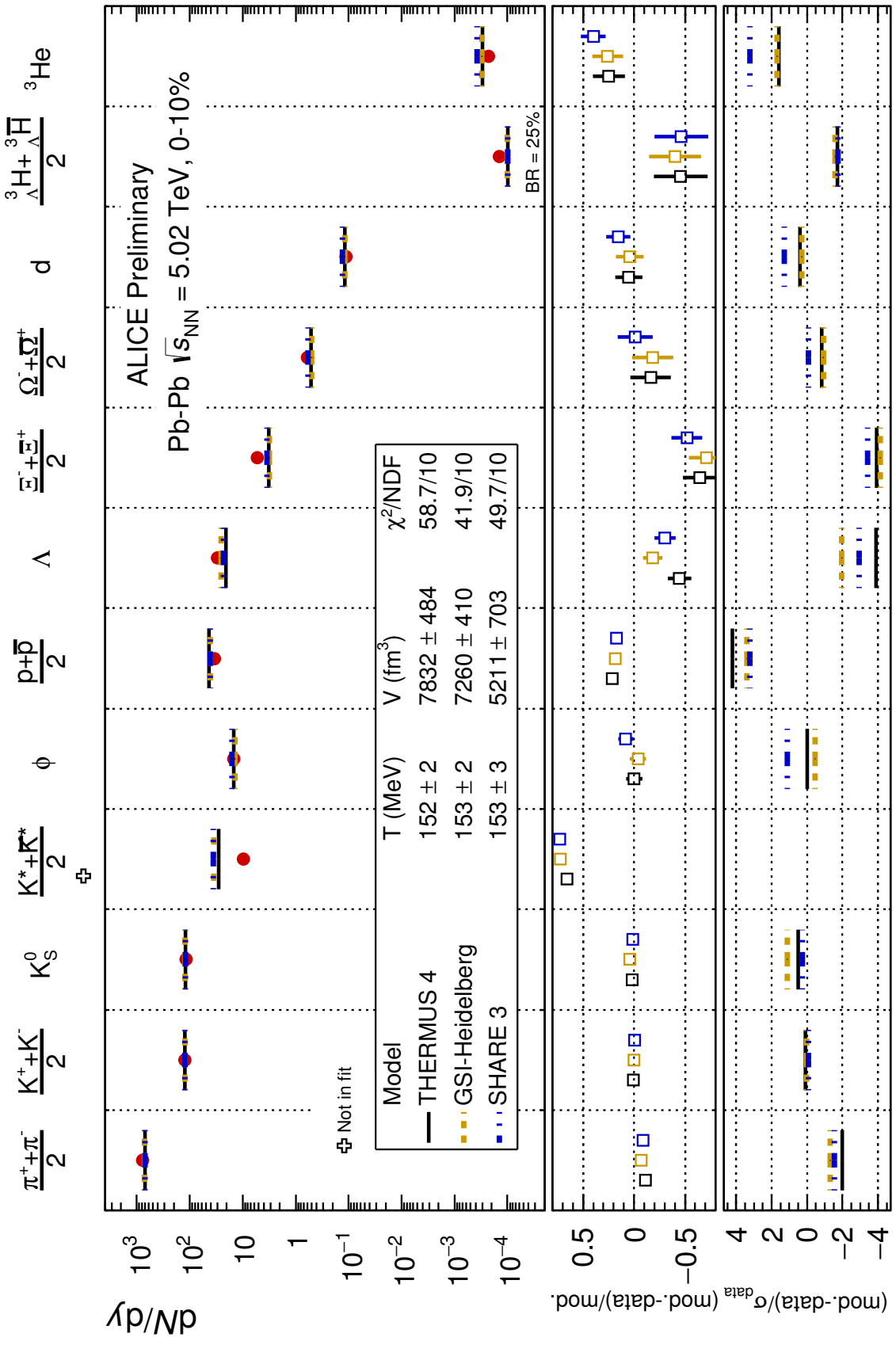

Figure 1.8: Grand canonical thermal fit of 0-10% central Pb-Pb collisions at 5 TeV, with 3 models (which are called THERMUS, GSI, SHARE).

created. In the transverse plane the overlap region has an almond-like shape, so the region is anisotropic with respect to the azimuthal angle. The azimuthal momentum distribution can be expanded into a Fourier series:

$$\frac{dN}{d\phi} = \frac{N}{2\pi}\left[1 + 2v_1 \cdot \cos\phi + 2v_2 \cdot \cos 2\phi + \cdots\right]$$

$$v_n = \frac{\int d\phi \cos(n\phi)\frac{dN}{d\phi}}{\int d\phi \frac{dN}{d\phi}} \equiv \langle \cos(n\phi) \rangle \tag{1.12}$$

where ϕ is the azimuthal angle of momentum and v_n are the Fourier coefficients of n-th harmonics [58]. Because of the symmetry around the y-axis the *sine* terms vanish. The first and second harmonics, v_1 and v_2 , are called **directed** and **elliptic flow** parameters, respectively. Directed flow is significantly seen near the beam rapidity region but vanishes near mid-rapidity due to symmetry of the collision geometry. The second harmonic, v_2, is much more relevant for studying matter around mid-rapidity in heavy-ion collisions at relativistic energies since spectators already fly away [59], therefore a lot of efforts to measure v_2 has been spent at RHIC and LHC so far. Elliptic flow is how the system responds to the initial spatial anisotropy [60, 61, 62]. To better clarify, we may suppose two extreme situations illustrated in Fig. 1.9. In the first case (see Fig. 1.9a) the mean free path among the produced particles is much larger than the typical size of the system. In this case the azimuthal distribution of particles does not depend on azimuthal angle on average due to the symmetry of the production process. The other extreme case is when the mean free path is very small compared to the typical system size (see Fig. 1.9b). In this case hydrodynamics can be applied to describe the space-time evolution of the system. The pressure gradient along the horizontal axis is much larger than that along the vertical axis due to the geometry.

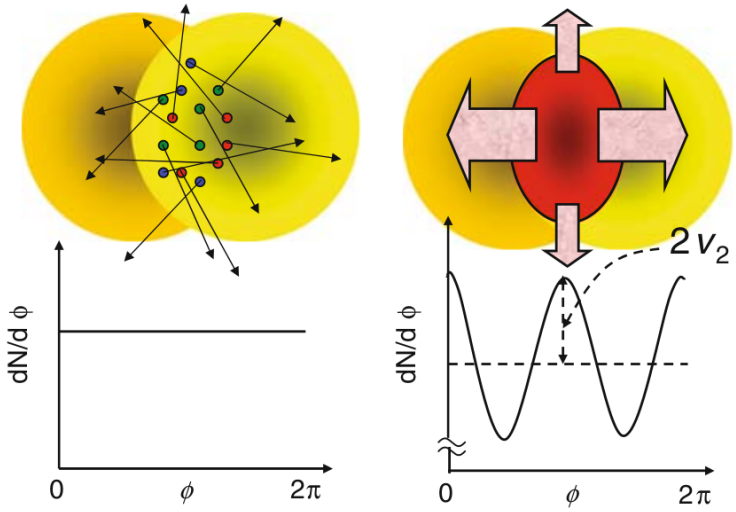

(a) Large mean free path (b) Small mean free path

Figure 1.9: Normalized azimuthal distribution $dN/d\phi$ of a non-central collision.

Chapter 2

LHC and the ALICE detector

In this chapter we want to describe the LHC facility, with a particular focus on the ALICE detector.

2.1 LHC

If we go from Geneva (CH, Switzerland) towards the northern French border, we come across the CERN (European Organization for Nuclear Research), the largest research centre in the world, with the greatest and most powerful collider of all times, LHC (Fig. 2.1). LHC is a 27 km ring, 100 m underground, kept at the coldest temperature achieved at a so large scale of something like 2 K. Its actual planned center of mass energy ($\sqrt{s}$) for the colliding beams (pp collisions) is 14 TeV, where until now we have just hit 13 TeV with an instant peak luminosity of 10^{34} cm^{-2}s^{-1}. The *luminosity* L is the quantity that multiplied by the cross-section σ gives the event rate as in:

$$\frac{dN}{dt} = \sigma \cdot L.$$

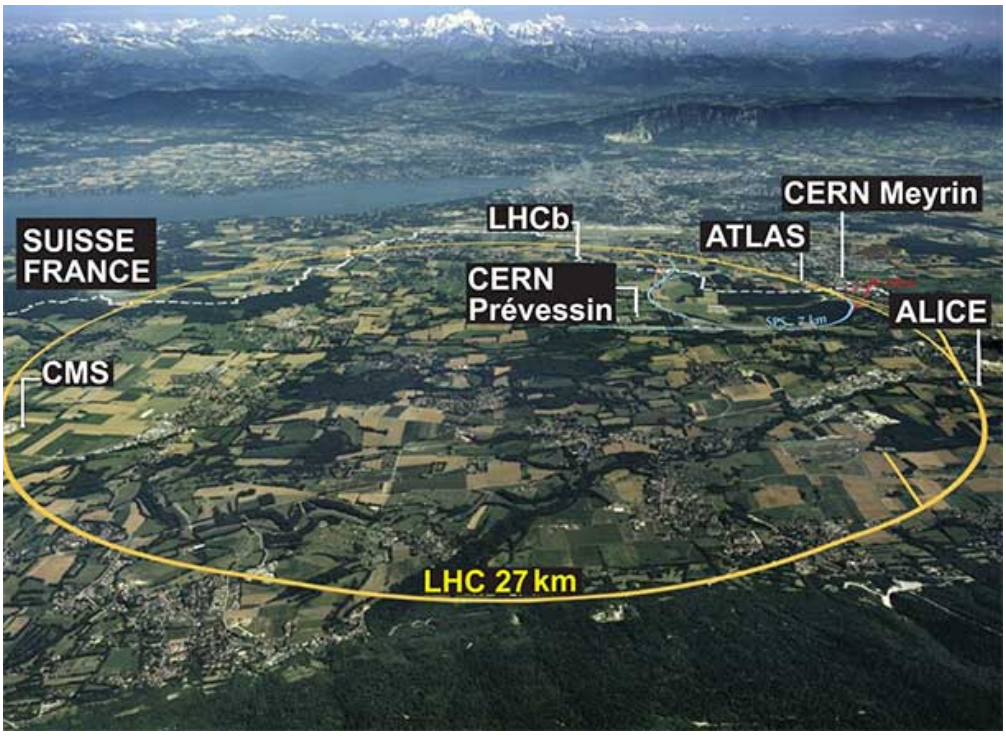

Figure 2.1: LHC ring. Aerial view.

Another useful quantity is the *integrated luminosity* L_{int} as[1]:

$$L_{int} = \int L dt.$$

If we walk alongside LHC, we find a few caverns. Four of them contain the four large detectors operating at LHC: LHCb (its main aim is to study the problem of CP violation), CMS (Compact Muon Solenoid, multipurpose detector with same goals of ATLAS but different technologies), ATLAS (A Toroidal LHC Apparatus), and finally ALICE (A Large Ion Collider Experiment, whose focus lies in the study of quark-gluon plasma formed in high energy heavy ion collisions).

[1] All collider experiments aim to maximize their integrated luminosities, as the higher the integrated luminosity, the more data is available to analyze. It is useful to note that L is explicitly given by geometrical factors of the proton bunches.

2.2 The ALICE detector: an overview

The ALICE Collaboration has built a dedicated heavy-ion collisions detector (Fig. 2.2) to better investigate the physical implications of such interactions. The hope of the scientific community is to find indications of the new state of matter, the QGP (Quark-Gluon Plasma) the first chapter has been fully dedicated to. The physical interest is wide, but just to name a few reasons, the QGP could possibly provide us with a better understanding of confinement and chiral symmetry restoration. At the beginning only ALICE was concerned about this type of colliding system (among all the CERN experiment). However, nowadays even the other detectors (e.g. ATLAS, CMS, LHCb) have been showing an increasing interest, and their upgrade will show this dedication [63, 64]. However, none of the other detectors can compete with the PID capabilities of ALICE, and this will become clear in the following, where a brief but exhaustive description of the many components of the ALICE apparatus, focusing on the Time-Of-Flight (TOF) detector, will be given.

The ALICE detector is designed to address the physics of strongly interacting matter and the quark-gluon plasma at extreme values of energy density and temperature in nucleus-nucleus collisions. It allows for a comprehensive study of hadrons, electrons, muons, and photons produced in the collision of heavy nuclei (Pb–Pb), up to the highest multiplicities anticipated at the LHC.

The choice and design of ALICE is driven by the physics requirements as well as by the experimental conditions expected in nucleus-nucleus collisions at the LHC. The most stringent design constraint is the extreme particle multiplicity. Originally, estimates for the charged particle multiplicity density at mid-rapidity in central Pb–Pb collisions spanned the range from $\frac{dN}{d\eta} = 2000$ up to almost $\frac{dN}{d\eta} = 8000$. The design of ALICE was optimized for a value of about $\frac{dN}{d\eta} = 4000$, but tested with simulations up to twice that amount. A large dynamic range is required for momentum measurement, spanning more than three orders of magnitude from tens of MeV/c to well over 100 GeV/c. This is achieved with a combination of very low material thickness to reduce multiple scattering at low p_{T} (13% X_0 up to the end of the TPC) and a large tracking lever arm of up to 3.5 m to guarantee a good resolution at

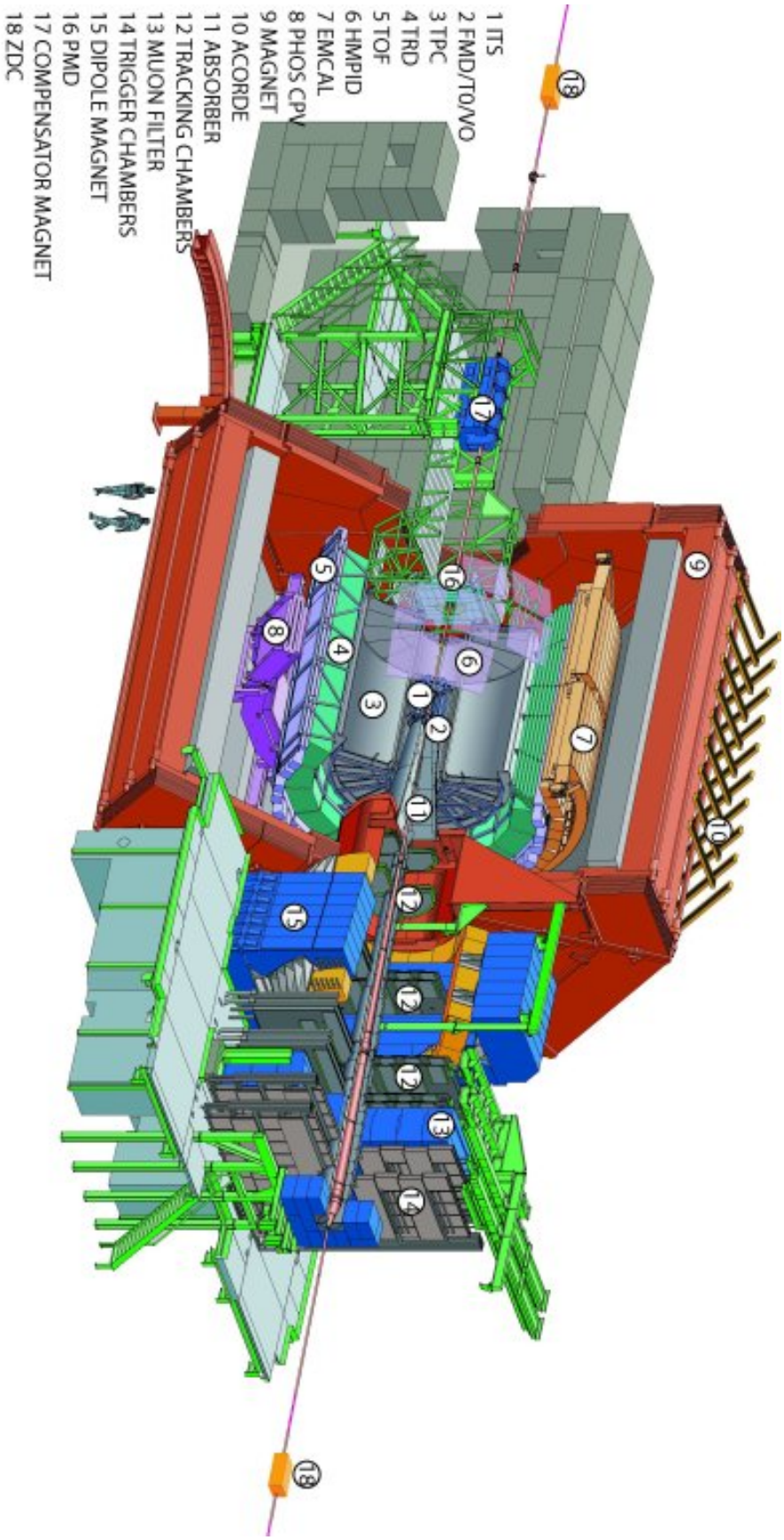

Figure 2.2: ALICE detector, full view.

high p_{T}.

The physics programme also includes collisions with lighter ions and at lower energy, in order to vary energy density and interaction volume, as well as dedicated proton-nucleus runs. Data taking during proton-proton runs at the top LHC energy provides reference data for the heavy-ion programme and address a number of specific strong-interaction topics for which ALICE is complementary to the other LHC detectors.

Looking inside the public page of the ALICE website [65], the very first line is at the same time amusing and of inspiration:

> The paradox of nuclear physics lies in the inverted ratio between the size of the observed objects and the instruments used : the smaller the scale, the larger the apparatus.

Needless to say, the ALICE apparatus is massive. It is a majestic detector, $16 \times 16 \times 26$ m^3, a heavyweight on top of that, weighing approximately 10^4 tons. Broadly speaking, it is safe to classify its components into three groups:

- **barrel detectors:** housed inside the L3 experiment solenoid magnet (Fig. 2.3, usually providing 0.5 T), they cover the pseudorapidity range $|\eta| < 0.9$ (see also Appendix B), or in other terms $\pi/4 < \theta < 3\pi/4$, with a 2π coverage in ϕ, the azimuthal angle. From the inside out, the barrel contains an Inner Tracking System (ITS) of six planes of high-resolution silicon pixel (SPD), drift (SDD), and strip (SSD) detectors, a cylindrical Time-Projection Chamber (TPC), the Transition Radiation (TRD) detector, three particle identification arrays of Time-of-Flight (TOF), Ring Imaging Cherenkov (HMPID), and two electromagnetic calorimeters (PHOS and EMCal). All detectors except HMPID, PHOS, and EMCal cover the full azimuth.

- **muon spectrometer:** placed in the forward pseudorapidity region (i.e. $-4 < \eta < -2.5$), it consists of a dipole magnet, tracking chambers and trigger chambers. Its aim is to reconstruct heavy quark resonances like the J/ψ through their $\mu^+\mu^-$ decay channel, and single muons.

Figure 2.3: The L3 magnet, now inheritance of the ALICE Collaboration.

- **forward detectors:** as the name implies, they occupy the high pseudorapidity regions, or equivalently the regions close to the beam pipe. They are small, and their aim is mostly triggering and measuring global event characteristics. We can list them: T0 (measuring the event time), V0 (rejects the beam-gas background and triggers minimum bias events), Forward Multiplicity Detector (FMD, provides information on the multiplicity), Photon Multiplicity Detector (PMD, as the name implies, it measures the multiplicity and the spatial distribution of photons in the $2.3 < \eta < 3.7$ region), and finally the Zero Degree Calorimeter (ZDC, it prevalently measures the number of spectators of the colliding nuclei in A–A collisions).

Additionally, an array of scintillators called ACORDE has been installed on top of the magnet to trigger on cosmic rays. A summary of the ALICE detector single components is shown inside Fig. 2.4. Later on a few more details will be given.

Detector	Acceptance (η, ϕ)	Position (m)	Dimension (m^2)	Channels
ITS layer 1,2 (SPD)	$\pm 2, \pm 1.4$	0.039, 0.076	0.21	9.8 M
ITS layer 3,4 (SDD)	± 0.9, ± 0.9	0.150, 0.239	1.31	133 000
ITS layer 5,6 (SSD)	± 0.97, ± 0.97	0.380, 0.430	5.0	2.6 M
TPC	± 0.9 at r=2.8 m ± 1.5 at r=1.4 m	0.848, 2.466	readout 32.5 m^2 Vol. 90 m^3	557 568
TRD	± 0.84	2.90, 3.68	716	1.2 M
TOF	± 0.9	3.78	141	157 248
HMPID	± 0.6, $1.2^\circ < \phi < 58.8^\circ$	5.0	11	161 280
PHOS	± 0.12, $220^\circ < \phi < 320^\circ$	4.6	8.6	17 920
EMCal	± 0.7, $80^\circ < \phi < 187^\circ$	4.36	44	12 672
ACORDE	± 1.3, $-60^\circ < \phi < 60^\circ$	8.5	43	120
Muon Spectrometer				
Tracking station 1	$-2.5 < \eta < -4.0$	-5.36	4.7	1.08 M
Tracking station 2		-6.86	7.9	
Tracking station 3		-9.83	14.4	
Tracking station 4		-12.92	26.5	
Tracking station 5		-14.22	41.8	
Trigger station 1	$-2.5 < \eta < -4.0$	-16.12	64.6	21 000
Trigger station 2		-17.12	73.1	
ZDC:ZN	$\lvert\eta\rvert < 8.8$	± 116	2×0.0049	10
ZDC:ZP	$6.5 < \lvert\eta\rvert < 7.5$ $-9.7^\circ < \phi < 9.7^\circ$	± 116	2×0.027	10
ZDC:ZEM	$4.8 < \eta < 5.7$, $-16^\circ < \phi < 16^\circ$ and $164^\circ < \phi < 196^\circ$	7.25	2×0.0049	2
PMD	$2.3 < \eta < 3.7$	3.64	2.59	2 221 184
FMD disc 1	$3.62 < \eta < 5.03$	inner: 3.2		
FMD disc 2	$1.7 < \eta < 3.68$	inner: 0.834 outer: 0.752	0.266	51 200
FMD disc 3	$-3.4 < \eta < -1.7$	inner:-0.628 outer:-0752		
V0A	$2.8 < \eta < 5.1$	3.4	0.548	32
V0C	$-1.7 < \eta < -3.7$	-0.897	0.315	32
T0A	$4.61 < \eta < 4.92$	3.75	0.0038	12
T0C	$-3.28 < \eta < -2.97$	-0.727	0.0038	12

Figure 2.4: Summary of the ALICE detector subsystems. The acceptance in η is calculated from the nominal interaction point and is 2π in azimuth, unless noted otherwise. The position is the approximate distance from the interaction point to the face of the detector and corresponds to the radius for barrel detectors (inner and outer radius for the TPC and TRD) or the position along the beam (z coordinate) for the others. The dimension corresponds to the total area covered by active detector elements. "Channels" is the total number of independent electronic readout channels. In case a detector is subdivided, the numbers refer to the individual components.

2.3 Magnets

The experiment includes the already mentioned solenoid magnet previously used in the L3 experiment of LEP, housing the central detectors, and a dipole magnet situated next to the solenoid which is part of the forward muon spectrometer. It is worth mentioning that the magnetic field provided by the solenoid may be as high as half a tesla and actually there have been instances where it had been lowered to $B = 0.2$ T. The dipole magnet is placed 7 m from the interaction vertex, at about 10 cm distance from the L3 solenoid [66].

2.4 ITS - Inner Tracking System

The main tasks of the Inner Tracking System (ITS) are to localize the primary vertex with a resolution better than 100 μm, to reconstruct the secondary vertices from the decays of hyperons and D and B mesons, to track and identify particles with momentum below 200 MeV/c, to improve the momentum and angle resolution for particles reconstructed by the Time-Projection Chamber (TPC) and to reconstruct particles traversing dead regions of the TPC.

The ITS surrounds the beam pipe, for which it provides the mechanical support so that no relative movement will take place during operation. The beam pipe is a 800 μm-thick beryllium cylinder of 6 cm outer diameter, coaxial with the ITS detector layers. The ITS consists of six cylindrical layers of silicon detectors, located at radii between 4 and 43 cm. It covers the pseudorapidity range of $|\eta| < 0.9$. Due to the high particle density expected in heavy-ion collisions at LHC, (as many as 50 particles per cm^2 had been predicted for the inner layer), Silicon Pixel Detectors (SPD) have been chosen for the innermost two layers, and Silicon Drift Detectors (SDD) for the following two layers. The two outer layers, where the track density had been expected to be below one particle per cm^2, are equipped with double-sided Silicon micro-Strip Detectors (SSD). The four outer layers can be used for particle identification via $\frac{d\mathrm{E}}{dx}$ measurement in the non-relativistic ($\frac{d\mathrm{E}}{dx} \propto \frac{1}{\beta^2}$) region. The momentum and impact parameter resolution for low-momentum particles are, however, dominated by

multiple scattering effects in the material of the detector. Consequently, the amount of material in the active volume had been kept to a minimum.

The granularity of the detectors was optimized to cope with a track density of 8000 tracks per unit of rapidity at mid-rapidity, the upper limit of theoretical predictions. Under these conditions, the ITS would detect simultaneously more than 15 000 tracks. Keeping the system occupancy low, at the level of a few per cent, requires several million effective cells in each layer of the ITS.

It is important to remind that the ITS will be undergoing a full revision for the LHC Run 3, and, as of now, the R&D has been completed and the prototypes have already been tested.

2.5 TPC - Time Projection Chamber

The Time-Projection Chamber (TPC) [67] is the main tracking detector of the central barrel and is optimised to provide, together with the other central barrel detectors, charged-particle momentum measurements with good two-track separation, particle identification, and vertex determination. The phase space covered by the TPC in pseudo-rapidity is $|\eta| < 0.9$ for tracks with full radial track length (e.g. matches in ITS, TRD, and TOF detectors); for reduced track length, an acceptance up to about $|\eta| < 1.5$ is viable. The TPC covers the full azimuth. A large p_{T} range is covered from low p_{T} of about 0.1 GeV/c up to 100 GeV/c, with resolutions $\sigma(p_{\mathrm{T}})/p_{\mathrm{T}} < 1\%$ and 3.5% respectively for $p_{\mathrm{T}} < 1$ GeV/c and 50 GeV/c [68].

Charged-particle tracking and PID via ionization energy loss (dE/dx) in the TPC is accomplished by the measurement of the ionization of up to 159 samples along a trajectory of ≈160 cm. Tipical energy loss resolutions are $\sigma(dE/dx)/(dE/dx) \approx 5.5\%$ to 7%, for central collisions. Further PID capabilities arise from topological reconstruction of the weak decays of strange hadrons and gamma conversions [68].

At the Pb-Pb design luminosity of the LHC, an interaction rate of 8 kHz had been expected, 10% of which are to be considered as central collisions. In the TPC design phase, an ex-

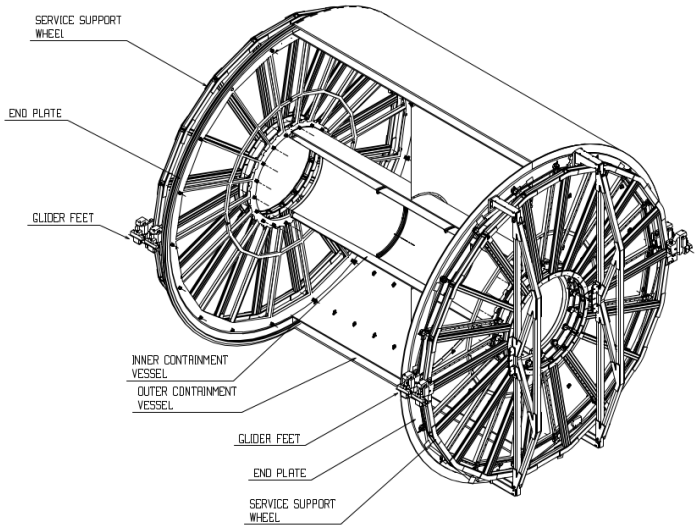

Figure 2.5: 3D view of the TPC field cage and service support wheels, without readout chambers.

treme charge particle multiplicity density of $\frac{dN}{d\eta} = 8000$ had been assumed, which would have resulted in 20 000 charged primary and secondary tracks in the TPC acceptance, an unprecedented track density for a TPC, setting new demands on the design, ultimately resulting in maximum occupancies (defined as the ratio of the number of readout pads and time bins above threshold to all pads and time bins) of about 40% at the innermost radius and 15% at the outermost radius for the quoted extreme multiplicity.

The TPC is cylindrical in shape; the active volume has an inner radius of about 85 cm, an outer radius of about 250 cm, and an overall length along the beam direction of 500 cm. The detector is made of a large cylindrical field cage (Fig. 2.5), filled with 90 m^3 of $Ne/CO_2/N_2$ (90/10/5) and multi-wire proportional chambers with cathode pad readout are mounted into 18 trapezoidal sectors at each end plate [69, 70]. Due to the $Ne/CO_2/N_2$ gas mixture used in the TPC, the field cage is operated at high voltage gradients, of about 400 V/cm, with a high voltage of 100 kV at the central electrode, which results in a maximum drift time of about 90 μs.

2.6 TRD - Transition Radiation Detector

The main purpose of the ALICE Transition Radiation Detector (TRD) [71] is to provide electron identification in the central barrel for momenta above 1 GeV/c. Below this momentum electrons can be identified via specific energy loss measurement in the TPC. Above this threshold, transition radiation (TR) from electrons passing a radiator can be exploited in concert with the specific energy loss in a suitable gas mixture to obtain the necessary pion rejection capability. In conjunction with data from the ITS and the TPC it is possible to study the production of light and heavy vector-meson resonances and the dilepton continuum both in pp as well as in Pb–Pb collisions. By making use of the excellent impact parameter resolution of the ITS, it is possible to reconstruct open charm and open beauty in semi-leptonic decays.

The TRD consists of 540 individual readout detector modules. They are arranged into 18 super modules each containing 30 modules arranged in five stacks along z and six layers in radius. In the longitudinal (z) direction, the active length is 7 m, the overall length of the entire super module is 7.8 m, its total weight is 1650 kg. Each detector element consists of a radiator of 48 mm thickness, a drift section of 30 mm thickness, and a multi-wire proportional chamber section (7 mm) with pad readout. Ionizing radiation produces electrons in the counting gas (Xe/CO_2 (85:15)). Particles exceeding the threshold for transition radiation production ($\gamma \simeq 1000$) will in addition produce X-ray photons in the energy range of 1 to 30 keV. X-rays in this energy regime are efficiently converted by the high-Z counting gas with the largest conversion probability at the very beginning of the drift region. All electrons from ionization energy loss and X-ray conversions will drift towards the anode wires. After gas amplification in the vicinity of the anode wires the signal is induced on the readout pads.

2.7 TOF - Time-Of-Flight, brief introduction

The Time-Of-Flight (TOF) detector [72] is a large array that covers the central pseudo-rapidity region ($|\eta| < 0.9$) for Particle IDentification (PID) in the intermediate momentum

range, below about 2.5 GeV/c for pions and kaons, up to 4 GeV/c for protons, with a π/K and K/p separation better than 3σ. The TOF, coupled with the ITS and TPC for track and vertex reconstruction and for $\frac{dE}{dx}$ measurements in the low-momentum range (up to about 1 GeV/c), provides event-by-event identification of large samples of pions, kaons, and protons. In addition identified kaons allow for invariant mass studies, in particular the detection of open heavy-flavoured states and vector-meson resonances.

More precisely, the TOF detector should cover the hadron momentum range from about 0.5 GeV/c (upper limit for dE/dx measurements in both the ITS and TPC detectors for K/π separation) to about $4 \div 5$ GeV/c, in order to satisfy the basic physics goals which had been described in the first chapter ultimately requiring a TOF detector with outstanding intrinsic characteristics.

2.7.1 Determining TOF resolutions

To evaluate the influence of different parameters of the TOF system on the PID quality, we should firstly consider the following equations [73]:

$$m = p \cdot \sqrt{\frac{t^2}{L^2} - 1} \tag{2.1}$$

where m is the mass of the particle, p the momentum, E the energy, t the time-of-flight and L the track length. Owing to:

$$\frac{\delta m}{m} = \frac{1}{m}\frac{\partial m}{\partial p}\cdot\delta p + \frac{1}{m}\frac{\partial m}{\partial t}\cdot\delta t + \frac{1}{m}\frac{\partial m}{\partial L}\cdot\delta L = \frac{\delta p}{p} + \left(\frac{E}{m}\right)^2\frac{\delta t}{t} + \left(\frac{E}{m}\right)^2\frac{\delta L}{L}$$

it is easy to see that at relatively high momenta, the resolution is driven much more by the errors on the time-of-flight and track length measurements than by the error on the momentum determination. The nominal performance of a TOF array with a system resolution from 80 to 150 ps, located at R = 3.70 m from the vertex is shown in Fig. 2.6.

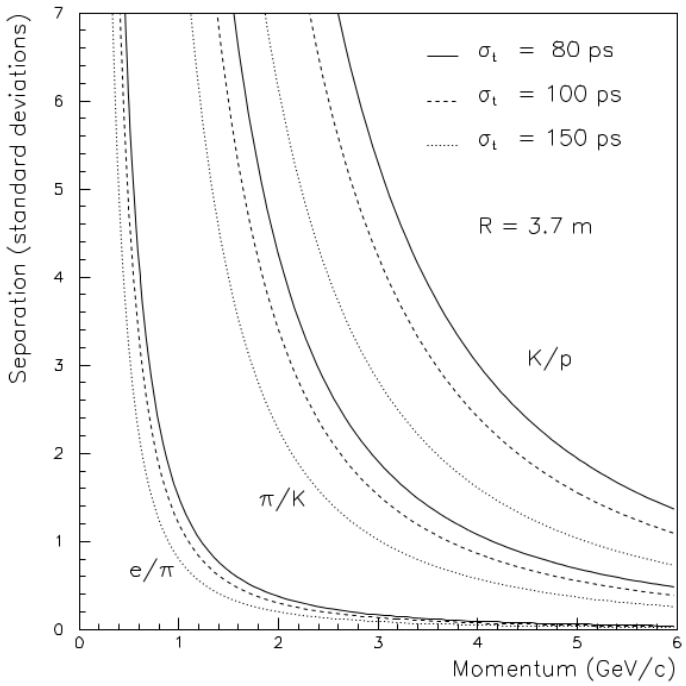

Figure 2.6: Particle separation with a TOF detector at R = 3.70 m, i.e. ALICE TOF.

2.7.2 Technical design

Aiming to build a TOF array, covering approximately 140 m^2 , with roughly 160 000 cells, 2.5×3.5 cm^2 each , with a time resolution better than 100 ps implies that the actual cost of such a system would be outrageous had it not been a gaseous detector [74]. That is why the chosen design had envisaged the use of MRPC [75]. The TOF detector covers a cylindrical surface of rapidity acceptance $|\eta| < 0.9$ and full ϕ coverage, with an inner radius of 3.7 m. Its whole structure is divided in 18 supermodules (sectors) (Fig. 2.7). Each supermodule is again divided in 5 parts (2 outer, 2 intermediate, and 1 central). Each outer and intermediate submodule houses 18 MRPCs while the 18 central parts only have 15 MRPCs inside.

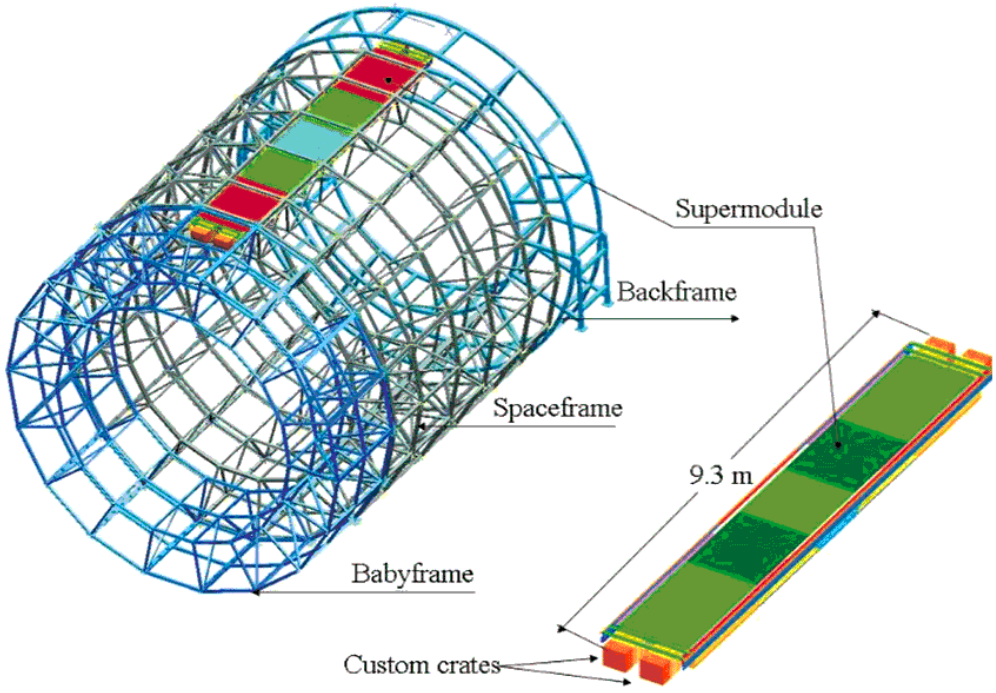

Figure 2.7: A schematic layout of one of the 18 TOF supermodules.

2.7.3 The double-stack MRPC

The double-stack MRPC is the final considered design during the TOF R&D. It consists of two stacks of equally spaced resistive plates, creating a series of gas gaps. High voltage is applied to the outer surfaces of the stack of resistive plates while all the internal plates are electrically floating. In this way the internal plates take voltage given by electrostatics and they are kept at the correct voltage values by the flow of positive ions and electrons created in the avalanches. Two external and one central printed circuit boards (PCB) contain the cathode and anode readout pads (96 per MRPC). Each stack has 5 gas gaps of 250 μm, see Fig. 2.8. This gap is possible thanks to a fish-line spacer held around a series of nylon screws, fixed in drilled holes in one of the two external central printed circuit boards. Due to the stack structure, the avalanches produced in different gaps by through-going particles ionizing the gas are independent and the signal is the sum of all gaps'. The resistive plates are made of soda-lime glass [76] with the internal and outer plates being 400 and 550 μm thick, respectively. To provide a good mechanical rigidity, two honeycomb panels are glued on the external PCBs.

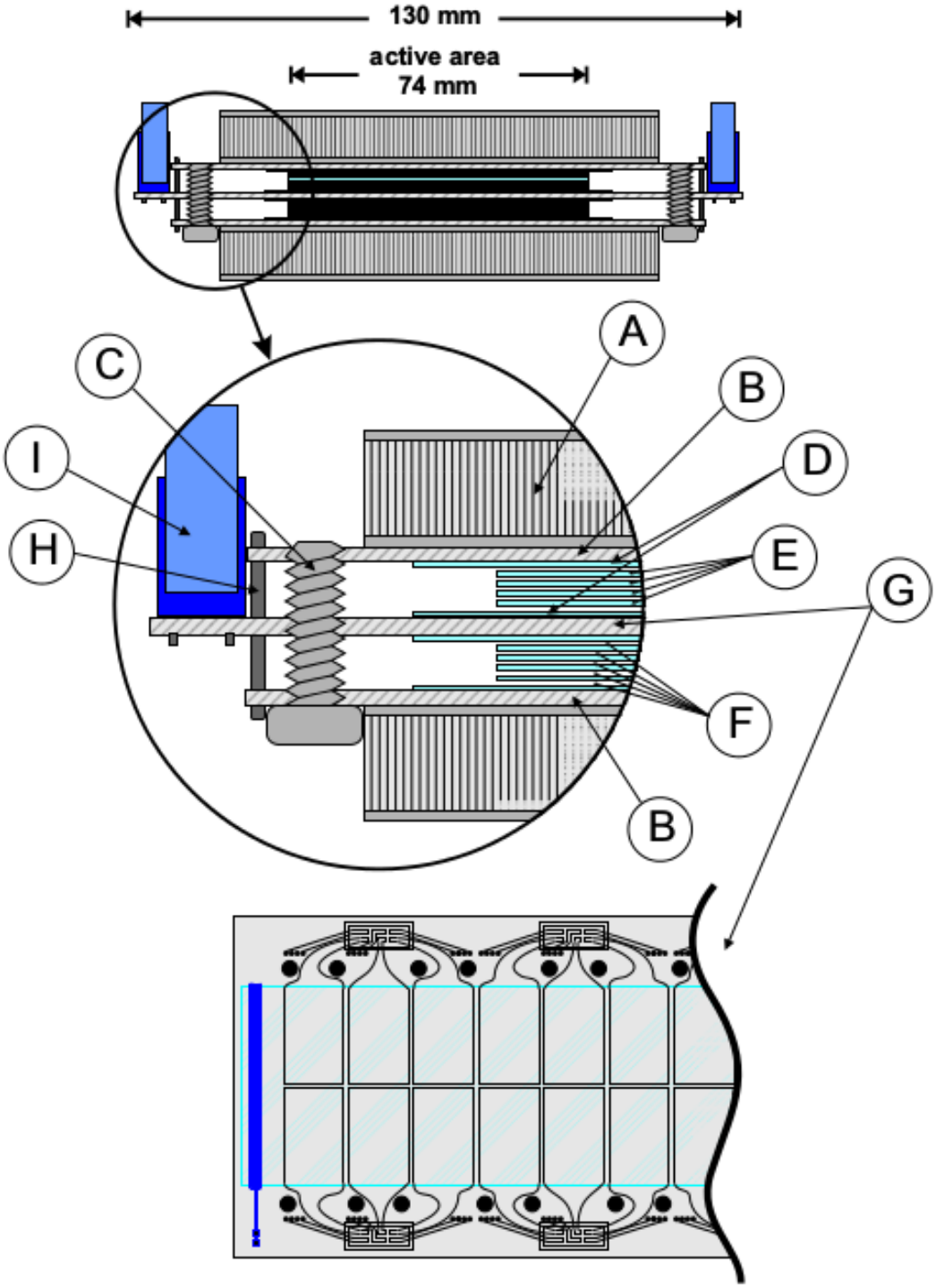

Figure 2.8: Schematic drawing (cross section and top view of the anode PCB) of the ALICE TOF MRPC strip. (A) 10 mm thick honeycomb panel; (B) PCB with cathode pads; (C) M5 nylon screw to hold fishing line; (D) 550 μm thick external glass plates with resistive coating; (E) 400 μm thick internal glass plates; (F) 250 μm wide gas gaps; (G) PCB with anode pads; (H) metallic pins to bring cathode signals to central PCB; (I) connectors for differential signal from MRPC to front-end electronics.

TOF performance: In a beam test setup [77] the average MRPC time resolution, including the contributions of the complete front-end and readout electronics, was *measured to be better* than 50 ps. During collisions the time resolution of the TOF was measured to be about 56 ps [78], which is very close to the performance obtained on test beam data.

2.8 HMPID - High-Momentum Particle Identification Detector

The High-Momentum Particle Identificaton Detector (HMPID) [79], is dedicated to measurements of identified hadrons at $p_{\mathrm{T}} > 1$ GeV/c. Its aim is to enhance the PID capability of ALICE by enabling identification of charged hadrons beyond the momentum interval attainable through energy-loss (in ITS and TPC) and time-of-flight measurements (in TOF). The detector was optimised to extend the useful range for π/K and K/p discrimination, up to 3 GeV/c and 5 GeV/c, respectively. The HMPID was designed as a single-arm array with an acceptance of 5% of the central barrel phase space.

The HMPID is based on proximity-focusing Ring Imaging Cherenkov (RICH) counters and consists of seven modules of about 1.5×1.5 m^2 each, mounted in an independent support cradle. The radiator, which defines the momentum range covered by the HMPID, is a 15 mm thick layer of C_6F_{14} (perfluorohexane) liquid with an index of refraction of $n = 1.2989$ at $\lambda = 175$ nm corresponding to $\beta_{min} = 0.77$ (i.e. a momentum threshold $p_{th} = 1.21m$ [GeV/c] where m is the particle mass). Cherenkov photons, emitted by a fast charged particle traversing the radiator, are detected by a photon counter.

2.9 PHOS - PHOton Spectrometer

The PHOton Spectrometer (PHOS) [80] is a high-resolution electromagnetic spectrometer covering a limited acceptance domain at central rapidity. The main physics objectives are the

test of thermal and dynamical properties of the initial phase of the collision extracted from low p_{T} direct photon measurements and the study of jet quenching through the measurement of high-p_{T} π^0. The high particle multiplicity in nuclear collisions requires a dense, highly segmented calorimeter with small Molière radius at a large distance from the interaction point to keep the cell occupancy at a manageable level. Direct photons are discriminated against decay photons either through shower shape analysis at high p_{T} or through invariant mass analysis at low p_{T}. The high-energy resolution and granularity is provided by using dense scintillator material (lead-tungstate, $PbWO_4$) of 20 X_0 with high photo-electron yield.

PHOS is designed as a single-arm high-resolution high-granularity electromagnetic spectrometer consisting of a highly segmented electromagnetic calorimeter (PHOS) and a Charged-Particle Veto (CPV) detector. PHOS is subdivided into five independent PHOS+CPV units, called PHOS modules. It is positioned on the bottom of the ALICE setup at a distance of 460 cm from the interaction point. After its final installation it covers approximately a quarter of a unit in pseudo-rapidity, i.e. $|\eta| < 0.12$, and 100 degrees in azimuthal angle.

2.10 EMCAL - ElectroMagnetic CALorimeter

The ElectroMagnetic CALorimeter (EMCAL) [81] has been designed with the aim to enable ALICE to explore in detail the physics of jet quenching (interaction of energetic partons with dense matter). The EMCal is a large Pb-scintillator sampling calorimeter with cylindrical geometry, located adjacent to the ALICE magnet coil at a radius of ≈4.5 metres from the beam line. It covers $|\eta| < 0.7$ with an azimuthal coverage of $\Delta\phi = 107$ degrees, and is positioned approximately opposite in azimuth to the high-precision ALICE Photon-Spectrometer (PHOS) calorimeter. The size of the EMCal is constraint by the available free space and the maximum weight which can be supported by the L3 magnet. The emphasis on high p_{T} means that the intrinsic energy resolution of the EMCAL can be modest and the detector granularity can be coarser, with moderately high occupancy.

2.11 ACORDE - ALICE COsmic Ray DEtector

ACORDE, the ALICE cosmic ray detector, is an array of plastic scintillator counters placed on the upper surface of the L3 magnet. It plays a two-fold role in ALICE:

- the first task is to provide a fast (Level-0) trigger signal, for the commissioning, calibration and alignment procedures of some of the ALICE tracking detectors;
- it also detects in combination with the TPC, TRD and TOF, single atmospheric muons and multi-muon events thus allowing us to study high-energy cosmic rays in the energy region of the knee in the cosmic ray spectrum.

2.12 Forward Muon Spectrometer

Muon detection is performed in the pseudo-rapidity region $-4 < \eta < -2.5$ by the muon spectrometer. With this detector, the complete spectrum of heavy-quark vector-mesons resonances (i.e. J/ψ, ψ', Υ, Υ' and Υ''), as well as the ϕ meson, have been measured in the $\mu^+\mu^-$ channel. The simultaneous measurement of all the quarkonia species with the same apparatus allows for a direct comparison of their production rate as a function of different parameters such as transverse momentum and collision centrality. In addition to vector mesons, the unlike-sign dimuon continuum up to masses around 10 GeV/c^2 can be measured. Since at LHC energies the continuum is expected to be dominated by muons from the semi-leptonic decay of open charm and open beauty, it would become possible to study the production of open (heavy) flavours with the muon spectrometer. The physical motivation finds root in the QCD predicting a decreasing production of heavy quark resonances.

The spectrometer consists of the following components: a passive front absorber to absorb hadrons and photons from the interaction vertex; a high-granularity tracking system of 10 detection planes; a large dipole magnet; a passive muon-filter wall, followed by four planes of trigger chambers; an inner beam shield to protect the chambers from primary and secondary particles produced at large rapidities.

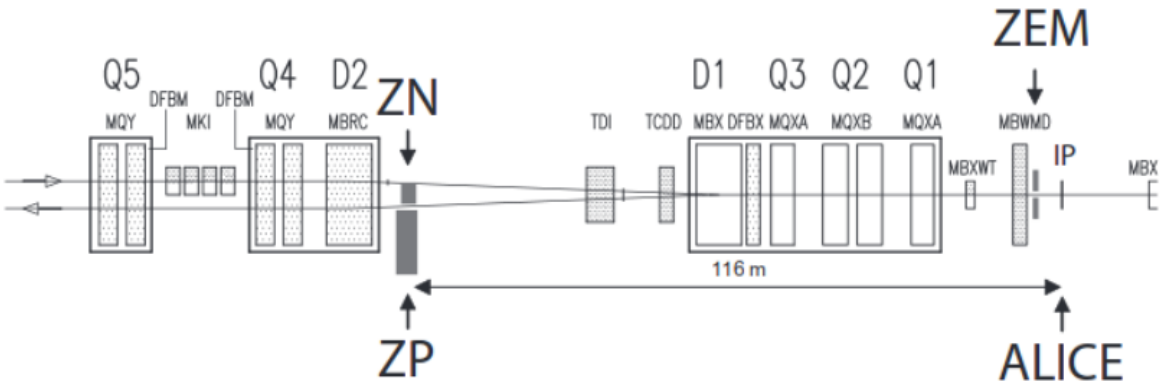

Figure 2.9: Schematic top view of the side of the ALICE beam line opposite to the muon arm. The locations of the neutron (ZN), proton (ZP) and forward electromagnetic (ZEM) calorimeters are shown. The position of the beam line dipoles (Dx) and quadrupoles (Qx) are also indicated.

2.13 Forward Detectors

ZDC: The number of participant nucleons is the observable most directly related to the geometry of A–A collisions. It can be estimated by measuring the energy carried in the forward direction by non-interacting (spectator) nucleons. In ALICE, spectator nucleons are detected by means of Zero-Degree Calorimeters (ZDC). In addition, the ZDC can give an estimate of the reaction plane in nuclear collisions being also a position-sensitive detector.

In ALICE two sets of hadronic ZDCs are located at 116 m on either side of the Interaction Point (IP), see Fig. 2.9. In addition, two small electromagnetic calorimeters (ZEM) are placed at about 7 m from the IP, on both sides of the LHC beam pipe, opposite to the muon arm. Spectator protons are spatially separated from neutrons by the magnetic elements of the LHC beam line. Therefore, each ZDC set is made by two distinct detectors: one for spectator neutrons (ZN), placed between the beam pipes at 0 degrees relative to the LHC axis, and one for spectator protons (ZP), placed externally to the outgoing beam pipe on the side where positive particles are deflected.

PMD: The multiplicity and spatial distribution (η-ϕ) of photons in the forward pseudo-rapidity region of $2.3 < \eta < 3.7$ are measured by the Photon Multiplicity Detector (PMD) [82]. Due to the large particle density in the forward region, calorimetric techniques for photon measurements are not feasible. The PMD uses the preshower method where a three radiation length thick converter (1.5 cm thick lead with a 0.5 cm stainless steel backing) is sandwiched between two planes of highly granular gas proportional counters.

FMD: The main functionality of the Forward Multiplicity Detector (FMD) is to provide charged-particle multiplicity information in the pseudo-rapidity range $-3.4 < \eta < -1.7$ and $1.7 < \eta < 5$. The overlap between the FMD silicon rings and the ITS inner pixel layer provides redundancy and cross-checks of measurements between subdetectors and ensures that continuous coverage for a distribution of vertices along the z-axis.

V0: The V0 detector [83] is a small angle detector consisting of two arrays of scintillator counters, called V0A and V0C, which are installed on either side of the ALICE interaction point. The V0A detector is located 340 cm from the vertex on the side opposite to the muon spectrometer whereas V0C is fixed to the front face of the hadronic absorber, 90 cm from the vertex. They cover the pseudo-rapidity ranges $2.8 < \eta < 5.1$ (V0A) and $-3.7 < \eta < -1.7$ (V0C) and are segmented into 32 individual counters each distributed in four rings.

T0: The T0 detector [84] had been designed with the following objectives: firstly, to provide the event time needed for PID with the TOF detector. This timing signal corresponds to the real time of the collision (plus a fixed time delay) and is independent of the position of the vertex. Then, to provide a L0 trigger when the position is within the preset values discriminating against beam-gas interactions. The detector consists of two arrays of Cherenkov counters, 12 counters per array.

Chapter 3

π, K, p identification with TOF in Xe–Xe collisions

This thesis describes the strategy and techniques used to perform the measurement of the $\pi^{\pm}$, $K^{\pm}$, p and $\bar{p}$ in Xe–Xe collisions at $\sqrt{s_{NN}} = 5.44$ TeV for the TOF system. However, the whole analysis requires a combination with other different autonomous sub-analysis based on other sub-detectors of the ALICE apparatus, using different techniques concerning PID, namely the TPC and ITS. In order to ensure the cross-analysis compatibility of the results common tools were used for what concerns event and track selection. The final goal of this analysis is the combination of all results so as to provide a unique spectra covering the widest p_T interval possible with the best precision.
Single analyses are inspired by previous studies performed for the same type of measurement, in particular Pb–Pb at $\sqrt{s_{NN}} = 5.02$ TeV and $\sqrt{s_{NN}} = 2.76$ TeV. However differences do emerge. The most relevant one is due to the lower magnetic field $B = 0.2$ T compared to the usual 0.5 T. Others are:

- ITS:
  - Dedicated study of the dE/dx parameterization in silicon in the low-B field configuration

Analysis	π	K	p
ITSsa	0.08-0.70 GeV/c	0.20-0.45 GeV/c	0.30-0.50 GeV/c
TOF	0.40-5.00 GeV/c	0.4-3.60 GeV/c	0.50-5.00 GeV/c
TPC	0.25-0.70 GeV/c	0.25-0.45 GeV/c	0.40-0.80 GeV/c

Table 3.1: π, K and p p_{T}-ranges in GeV/c used for the different detectors in Xe–Xe analysis.

- TOF:
  - Dedicated study of the TOF detector response at low p_{T} in the low-B field configuration
  - Dedicated study of the TPC-TOF mismatch contribution to the TOF signal
  - New template generation procedure
- TPC:
  - Dedicated study of the TPC response in the low-B field configuration
  - Detailed study of the contamination from feed-down

The combined spectra present an overlap in p_{T} ranges of the different analyses. These ranges are listed in Table 3.1.

The dataset is the LHC17n_pass1 (ESDs) collected in 2017, with low magnetic field configuration ($B = 0.2$ T), focusing only on the runs 280234 and 280235 (1.3 M events), corresponding to the Xe–Xe data taking period on October 12th, 2017. The actual aim of these collisions is to test the viability for the machinery to run with a different type of nuclei.

The setup of the event selection is performed automatically to make sure that each analysis is working with the same events. The events are divided in centrality classes: [0-5 %], [5-10 %], [10-20 %], [20-30 %], [30-40 %], [40-50 %], [50-60 %], [60-70 %], [70-80 %], [80-90 %].

3.1 TOF strategy

The analysis relies on the global tracks (ITS-TPC) and the extraction of the total yield by performing PID exclusively with the TOF detector. In particular the parameterization of the signal and the background will be described. The main goal of this analysis is to provide spectra as a function of p_{T} for identified π^+, π^-, K^+, K^-, p and $\bar{\mathrm{p}}$ at intermediate p_{T} that will be later combined with the ITS and TPC's spectra. The strategy, as it will be better explained in the following, is based on the comparison between the measured time of flight and its theoretical prediction for each mass hypothesis.

The analysis strategy mainly relies on tracks reconstructed in TPC which are extended to TOF. The assignment of a TOF cluster to the propagated track lets us record the precise measurement of the arrival time. This information, together with the measurement of the event time, is very useful to provide PID in the intermediate transverse momentum region. Examples of the measured particle velocity β as a function of the momentum p can be seen in Fig. 3.1 for Xe–Xe collisions.

The identification of different particle types is performed with a statistical approach, measuring the *time-of-flight* as reported in Eq.3.1.

$$time\text{-}of\text{-}flight = t_{\mathrm{TOF}} - t_0 \tag{3.1}$$

The time of flight is defined as the difference between the time measured by the TOF detector (t_{TOF}) and the start time t_0. For simplicity's sake from now on we will refer to the $time\text{-}of\text{-}flight$ as t.

The expected *time-of-flight* ($t_{exp,i}$) can be computed for every particle species for each track by taking into account the track length and the energy loss in the material.

The resolution on the time of flight can be obtained by Eq. 3.1:

$$\sigma_t^2 = \sigma_{TOF}^2 + \sigma_{t_0}^2 \tag{3.2}$$

The PID strategy with TOF takes advantage of the separation between the different particles

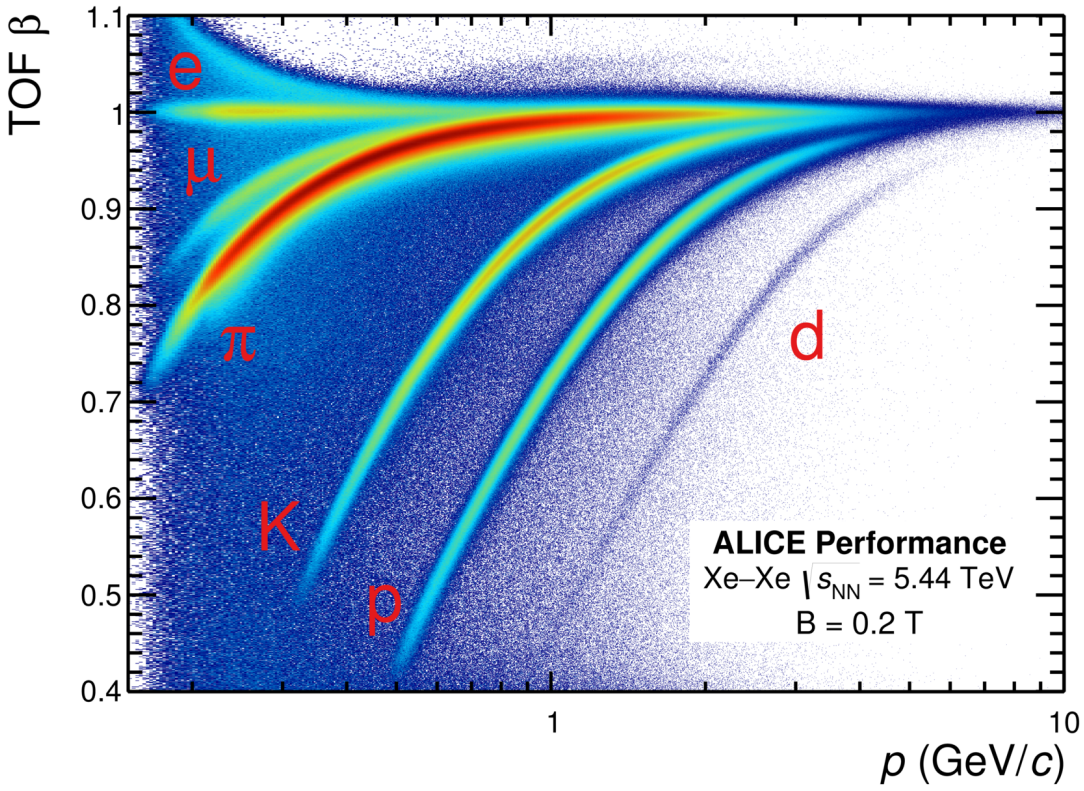

Figure 3.1: $\beta = \frac{v}{c} = \frac{L}{ct}$ measured with the TOF detector as a function of the track momentum in Xe–Xe collisions at $\sqrt{s_{\mathrm{NN}}} = 5.44$ TeV. The visible bands are from e, μ, π, K, p and d. The contribution from wrongly associated tracks can be seen outside the bands.

by calculating the $n\sigma$ separation:

$$n\sigma_i = \frac{t - t_{exp,i}}{\sigma_i} \tag{3.3}$$

Indicating by $n\sigma_i$ the distance in number of standard deviations of the measured value from the expected one under a specific mass hypothesis, and by σ_i the uncertainty on the numerator, which can be expressed as:

$$\sigma_i^2 = \sigma_t^2 + \sigma_{t_{exp}}^2 \equiv \sigma_{TOF}^2 + \sigma_{t_0}^2 + \sigma_{t_{exp}}^2 \tag{3.4}$$

The t_0 can be determined with different methods [85], each one with different precision. The measurement of the t_0 with the TOF is fully efficient in Xe–Xe collisions from central collision up to centrality bin $80\% - 90\%$, where instead the multiplicity of tracks reaching TOF is not high enough as to ensure the determination of the event time in each collision. In this case the measurement of the start time relies mostly on the T0 detector or, in case it is not available, on the bunch crossing time which has the worse resolution.

3.1.1 Track selection

The selection of a good track is based on the application of several requirements. As can be seen in Table 3.2, a good track has to traverse at least 70 TPC rows, has to show a χ^2/NDF less than 4, plus cuts on the DCA (Distance of Closest Approach), with the z and xy components treated differently. While the DCA_z cut is 2 cm, the DCA_{xy} cut is p_{T}-dependent and is shown in the next paragraphs. An additional requirement is that tracks are to be matched to TOF. The **Geometrical Cut** has been recently introduced to reject tracks based on their length in the TPC's active zone (geometric-length cut). Its working principle is illustrated in Fig. 3.2. The cut leads to a reduction of the raw yield in the p_{T}-area around 1.5 GeV/c, the p_{T} region where the tracks cross the TPC sector's boundaries with small inclination angles leading to a significant fraction of their lengths located close to chamber edges. How to achieve that is shown inside the table. Firstly, the dead zone width between the TPC's sectors is taken to be 2 cm, then the other two values imply the cut on

Track cut	Cut value
TPC Crossed Rows	70
Track Global χ^2 per NDF	4
Track DCA_z	2 cm
Track DCA_{xy}	see Eq. 3.5
Geometrical Cut	SetCutGeoNcrNcl(2., 130., 1.5, 0.0, 0.0)

Table 3.2: Summary of the cuts used to select the track sample, plus the recently introduced *Geometrical Cut*.

the track length L, that should be p_{T}-dependent as $L > 130 - \left(\frac{1}{\frac{p_{\mathrm{T}}}{\mathrm{GeV/c}}}\right)^{1.5}$ [cm].

Aiming to measure the spectra of primary particles i.e. the ones which are produced directly in the collision or in strong decays, a selection has been carried on, based on the distance of closest approach of the track to the primary vertex in the xy-plane (DCA_{xy}) as a function of the p_{T} . The p_{T} dependence of the DCA_{xy} cut is as follows:

$$DCA_{xy} < 0.0105 + \frac{0.0350}{\left(\frac{p_{\mathrm{T}}}{\mathrm{GeV/c}}\right)^{1.1}} \text{ [cm]} \tag{3.5}$$

The residual contamination from secondary particles produced in weak decays and knock out inside the medium which are not removed by the cut on DCA_{xy} is taken into account by estimating the real fraction of primary particles within the DCA_{xy} cut with a data driven approach. This fraction of primary particles is then used to correct for feed-down the measured spectra, the procedure to compute such correction is described below.

As a first step the DCA_{xy} distribution is measured as a function of p_{T} for each particle species in data and Monte Carlo. For the Monte Carlo case the particle identity is known from Monte Carlo Truth as well as for the mechanism of production (primaries, secondaries from strangeness or secondaries from material). In the data the selection of the particle species is performed with a 2σ cut on the combined signal in TPC[1] and TOF, defined as:

[1] $N\sigma_{TPC} = \frac{(dE/dx)_{measured} - (dE/dx)_{expected}}{\sigma_{dE/dx_{measured}}}$

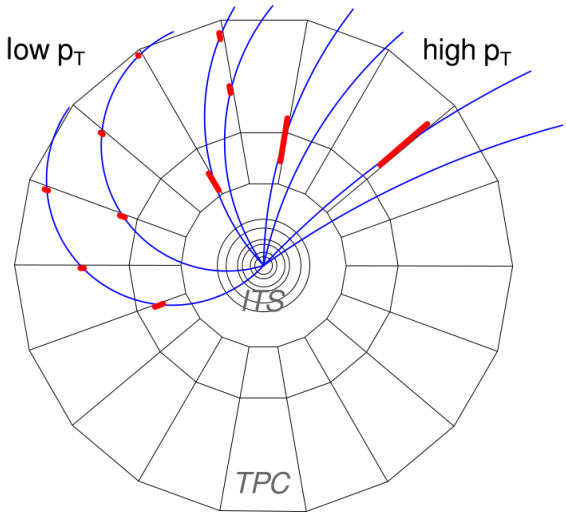

Figure 3.2: Sketch of the TPC's tracks. Low p_T tracks have only a small fraction of their lengths in dead areas (Red), as they cross the sector boundaries with a steep angle. High p_T tracks either are mainly located within dead zones or in the active area; therefore the fraction of rejected tracks is low. Tracks with an intermediate p_T are more likely to intersect a large fraction of the dead zone leading to being rejected more often than others.

$$\sigma_{TPC-TOF,\ i} = \sqrt{\sigma^2_{TPC,\ i} + \sigma^2_{TOF,\ i}} \tag{3.6}$$

The effect of the cut is shown in Fig. 3.3. This tight cut on the TPC-TOF signal is necessary to obtain the high purity sample of tracks and to avoid any contamination related bias on the DCA_{xy} distribution (which vary significantly depending on particle species). The Monte Carlo truth on PID is requested to construct the DCA_{xy} distributions for primary particles and the ones originating from feed-down (weak decays or production in material). The relative fractions are obtained with a template fit to the data, performed using the *TFractionFitter* class of Root or the *RooFit* package, see Figg. 3.4 and 3.5 for the template fits to π^+ and protons respectively. This procedure enables the unfolding of the various components of the convoluted DCA_{xy} distributions measured in real data with maximum likelihood algorithms. This feed-down correction is only evaluated for $\pi^{\pm}$, p and $\bar{\mathrm{p}}$ [86]. Kaons are not considered as they are strange particles, hence with limited production inside the medium like other particles, so for kaons a DCA cut is enough to distinguish primary particles. In order to extend the measurement of the primary fraction to higher p_{T} the values are fitted with the function reported in Eq. 3.7.

$$f_{primaries} = \alpha + \beta \cdot e^{\gamma \cdot x} \tag{3.7}$$

Primary fractions are shown for Minimum Bias[2] (MB) Xe–Xe collisions in Figg. 3.6 and 3.7 for π and p respectively, while in Fig. 3.8 primary fractions are shown as a function of centrality.

Since there is a strong centrality dependence, the corrections to remove contaminations from secondaries are calculated in each centrality class. This dependence is due to the increase of strangeness production (K^0_s and Λ) in the more central collisions.

[2]Minimum Bias events require at least a hit in the inner silicon detector (SPD) or in either of the two scintillator counter arrays (V0), essentially requiring at least one charged particle in 8 units of rapidity.

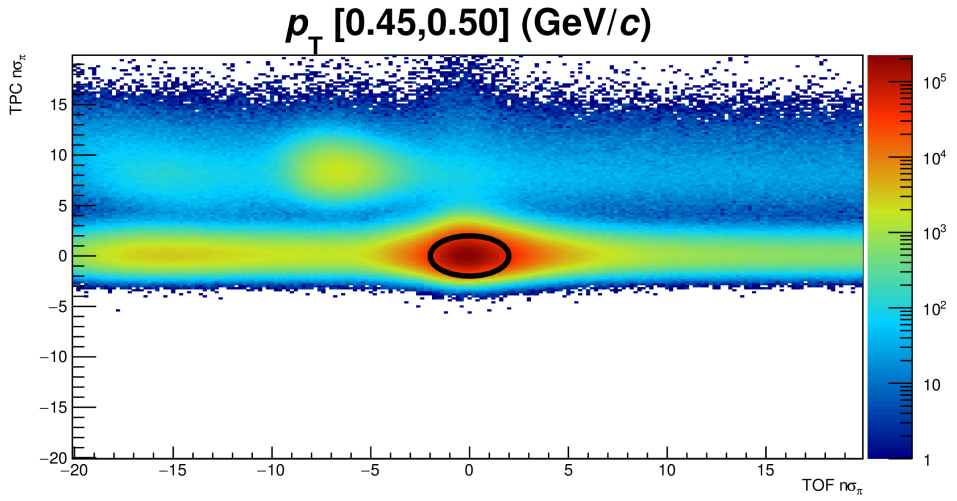

Figure 3.3: Combined separation for π performed with TOF (*x-axis*) and TPC (*y-axis*) in a selected p_{T} bin. The black circle represents a 2σ cut on the combined signal as reported in Eq. 3.6. The continuous bands which are evenly distributed over large range in TOF $n\sigma$ are due to tracks wrongly matched between TPC and TOF. This plot shows the PID based on the signal in TPC and TOF used to extract pure samples of π used to construct DCA_{xy} templates for the extraction of the primary fraction.

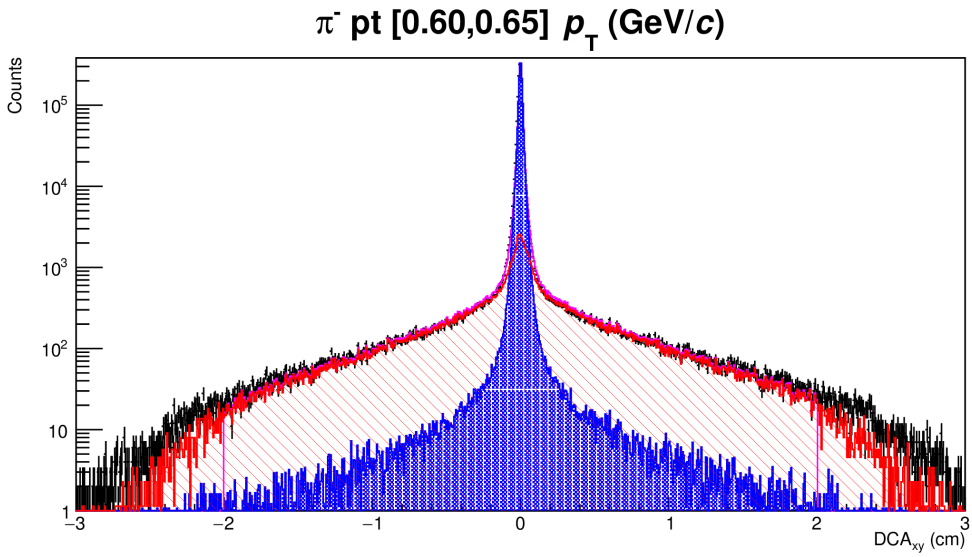

Figure 3.4: DCA_{xy} distribution measured for π^+ (in black) fitted with the templates for primary pions (in blue) and the one from weak decays (in red). The yield of primary particles is obtained by integrating the fitted template for primaries within the range defined by the DCA_{xy} cut reported in Eq. 3.5.

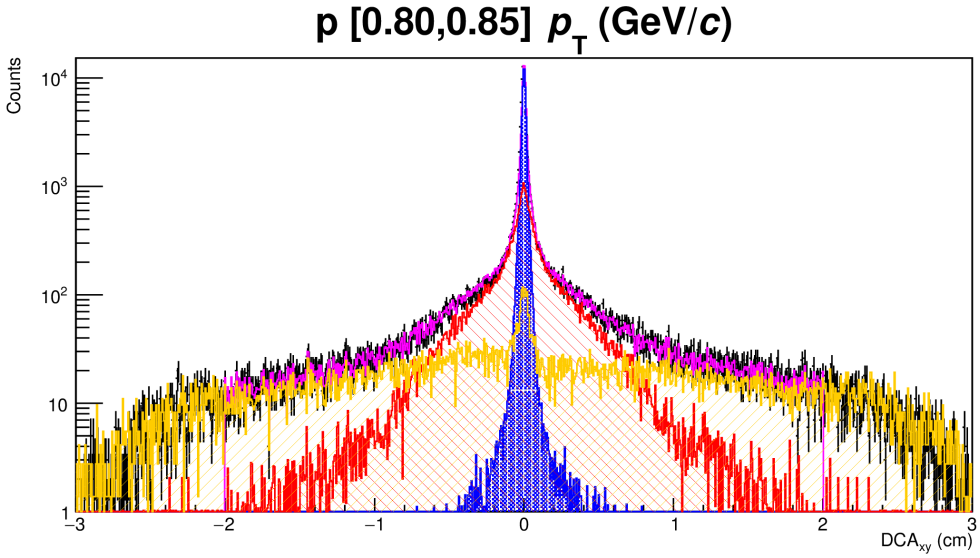

Figure 3.5: DCA_{xy} distribution measured for p (in black) fitted with the templates for primary protons (in blue), the one from weak decays (in red), and the one from material (in orange). The yield of primary particles is obtained by integrating the fitted template for primaries within the range defined by the DCA_{xy} cut reported in Eq. 3.5.

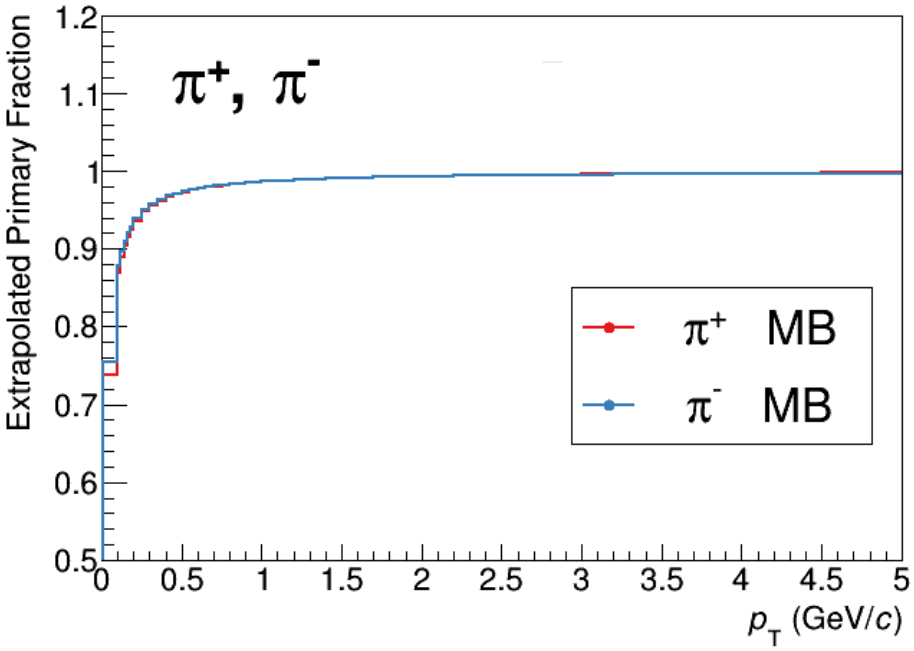

Figure 3.6: Primary fraction for π^+ and π^- in MB Xe–Xe collisions as a function of p_{T}. The values are obtained by fitting the fraction with the fit function reported in Eq. 3.7.

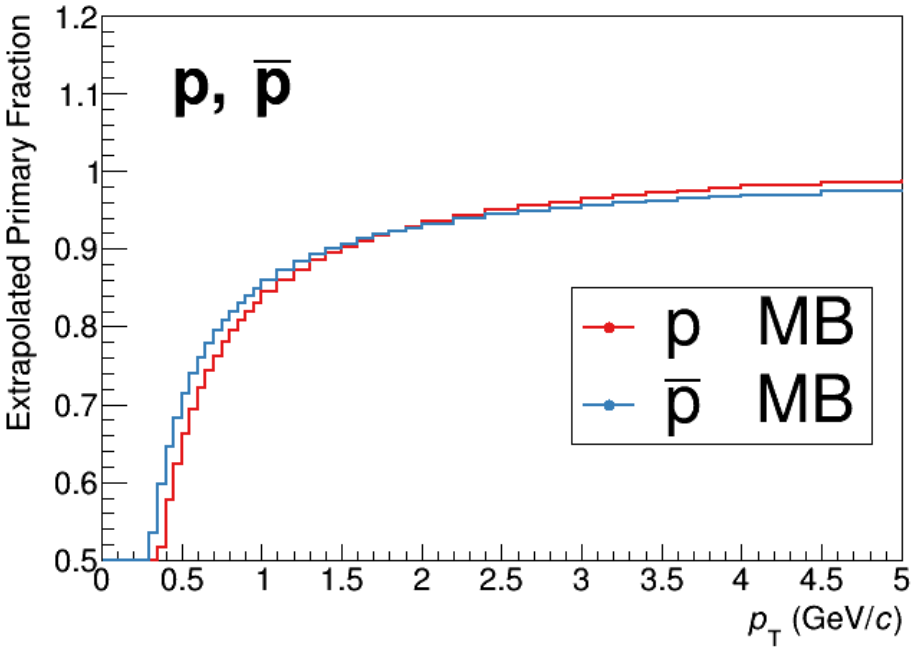

Figure 3.7: Primary fraction for p and $\bar{\mathrm{p}}$ in MB Xe–Xe collisions as a function of p_{T} . The values are obtained by fitting the fraction with the fit function reported in Eq. 3.7.

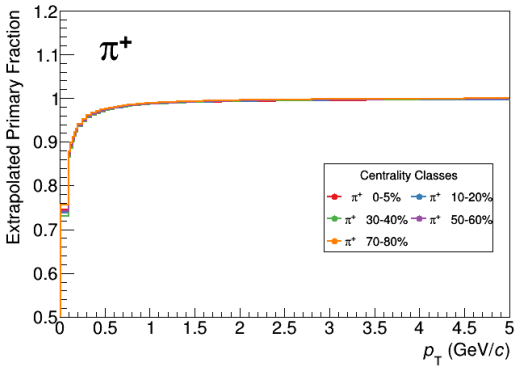

(a) Primary fraction for π^+ vs centrality.

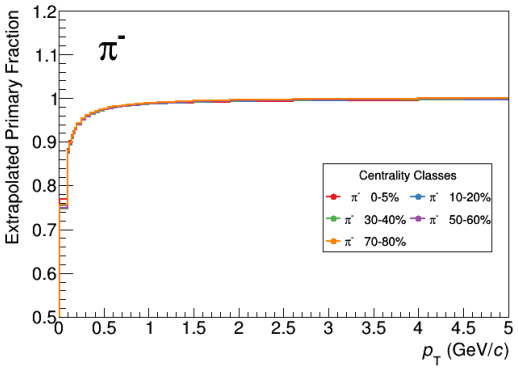

(b) Primary fraction for π^- vs centrality.

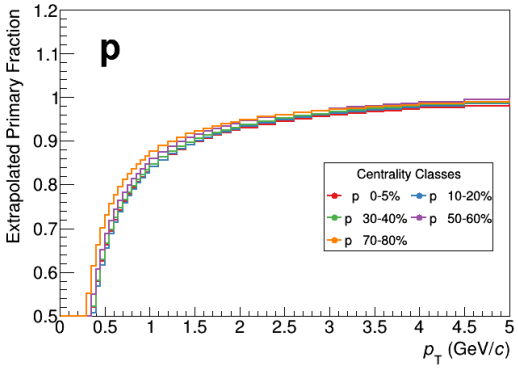

(c) Primary fraction for p vs centrality.

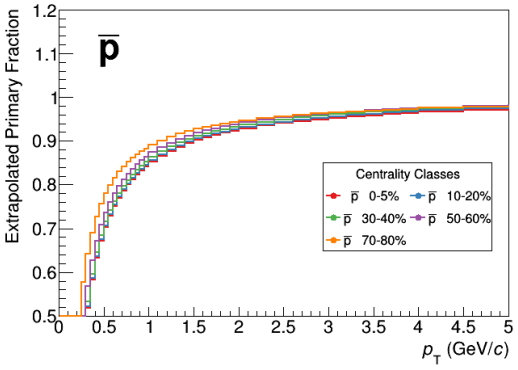

(d) Primary fraction for $\bar{\text{p}}$ vs centrality.

Figure 3.8: Primary fraction for both positive and negative π, and p/$\bar{\text{p}}$ as measured in each centrality class of Xe–Xe collisions.

3.2 TOF signal description

The TOF detector response must be correctly parametrized to perform particle identification. The parameterization is reported inside Eq. 3.8 and Eq. 3.9. Basically the actual form of $f(t)$ (t now represents $t_{TOF} - t_{exp}$, see Fig. 3.9) is the result of the convolution between a Gaussian distribution with an exponential tail on the right side of the peak (f_1, TOF response) and another pure Gaussian distribution (f_2, smearing for t_0 and t_{exp}).

$$f(t) = f_1(t) \otimes f_2(t) \tag{3.8}$$

$$f_1(t) = \begin{cases} \text{norm} \cdot \text{Gaus}(t, \mu, \sigma), & \text{if } t \leq \mu + \tau. \\ \text{norm} \cdot \text{Gaus}(\mu + \tau, \mu, \sigma) \cdot \exp\left(-\frac{\tau \cdot (t-\mu-\tau)}{\sigma^2}\right), & \text{otherwise.} \end{cases} \tag{3.9}$$

The parameters are tuned on real data and are set to $\mu = 0$, $\sigma = \sigma_{TOF} = 56$ ps and $\tau = 0.85\sigma$. These parameters are intrinsic to the TOF detector and are to be taken as asymptotic values that are measured once the particle momentum is high enough that the energy loss becomes negligible. The parameters used to describe the TOF signal are extracted with a fit to the distribution of $t - t_{exp,\pi} - t_0$ in the region where the peak for π is clearly separated in TOF.

This approach lets us deconvolute the effect on the resolution only due to the TOF itself (*intrinsic*) which will be called σ_{TOF}, with its actual value measured on real data of $\sigma_{TOF} =$ 56 ps. This procedure lets us also consider inside the signal parameterization the effect on the resolution related to the algorithm which computes the event start time based on the number of reconstructed tracks matched to the TOF system.

The TOF signal as it has been parametrized, is used to build the templates for all the particle species. These templates let us fit the data and extract the particle raw yields.

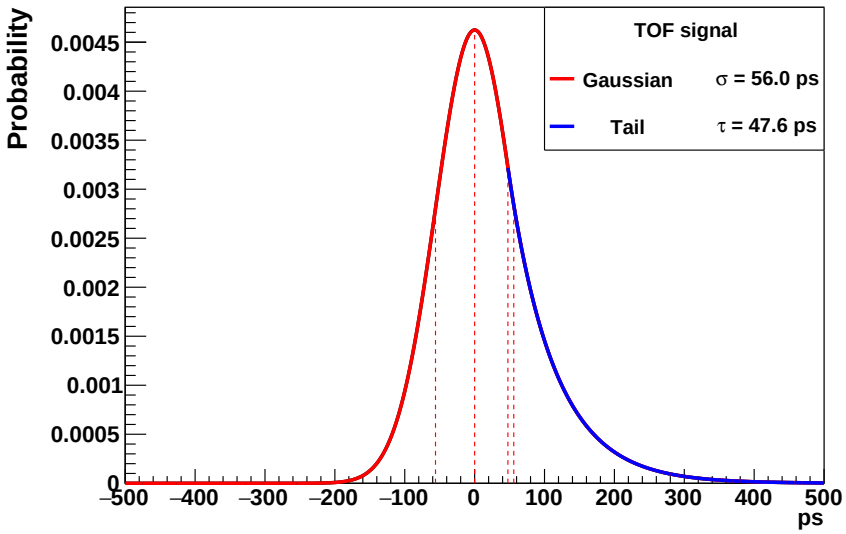

Figure 3.9: Representation of the TOF signal parameterization as reported in Eq. 3.9. The Gaussian part is drawn in red while the exponential tail is drawn in blue. The bands at $\pm 1\sigma$ and $\mu + \tau$.

3.3 TPC-TOF mis-association (mismatch)

In high occupancy environments like the heavy-ion collisions, it is possible that a track, correctly defined inside the TPC, is matched to a time which does not correspond to the one of the track, due to combinatorial background. This uncorrelated background is known as *mismatch* and has to be accounted for in both yield extraction and efficiency correction. Mismatch is also present in pp collisions, albeit smaller.

A data driven approach is chosen to parametrize the mismatch contribution. The uncorrelated background is obtained by sampling the distribution of TOF raw times shown in Fig. 3.10. The mismatch distributions $t_i = t_{mismatch} - t_{exp,i}$ are computed for each particle hypothesis i, where $t_{mismatch}$ indicates the raw time obtained from the sampling.

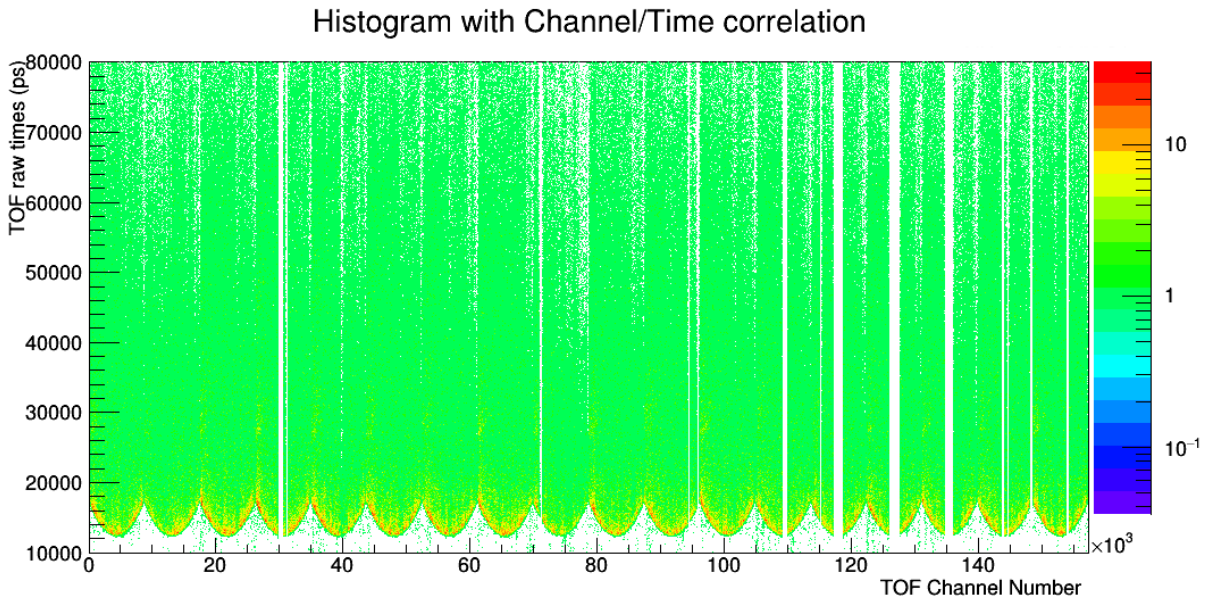

Figure 3.10: TOF raw time - TOF channel number correlation extracted from data. The visible structures are due to the geometrical location of the different channels.

3.4 Raw spectra

Templates for each particle species (e, μ, π, K, p, d) plus an additional one to account for the TPC-TOF track mismatch have been generated. These templates will be used together for the raw yield extraction. The procedure for the raw yield extraction uses the templates to perform a fit to the data. It is important to note that the data distribution to which the templates are fitted is constructed for each mass hypothesis (π, K, p) to correctly define the rapidity cut ($|y| < 0.5$). This means that it is not possible to extract simultaneously the yield of all particle species but a separated procedure is required. The raw yields for each particle species are computed by integrating the fitted distribution. An example of how the templates look like when put together is inside Fig. 3.11.

The raw spectra have been obtained with all these ingredients for all the centrality bins. They are shown in Figg. 3.12, 3.13, 3.14, for π, K, and p respectively.

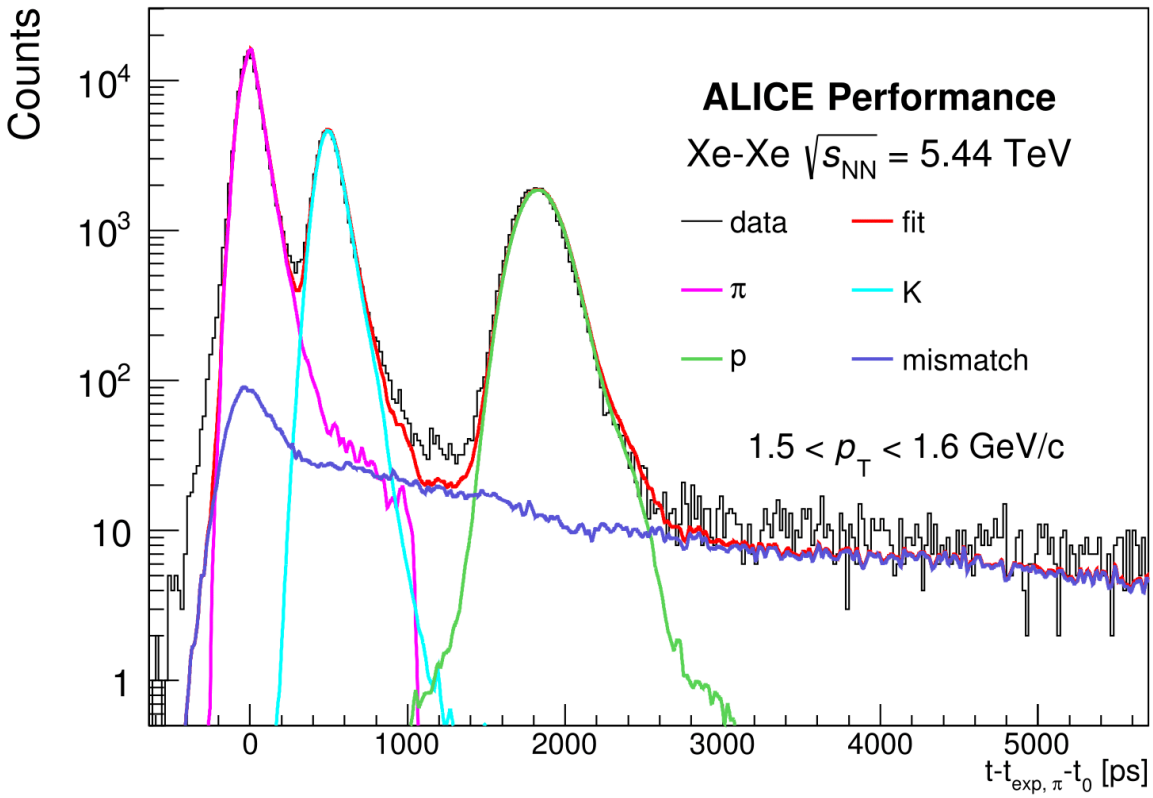

Figure 3.11: TOF signal: single template components. Mismatch depicted with a dark blue colour, pions with magenta, kaons with light blue and protons with green. The analyzed p_{T} bin is $[1.00, 1.10]$ GeV/c.

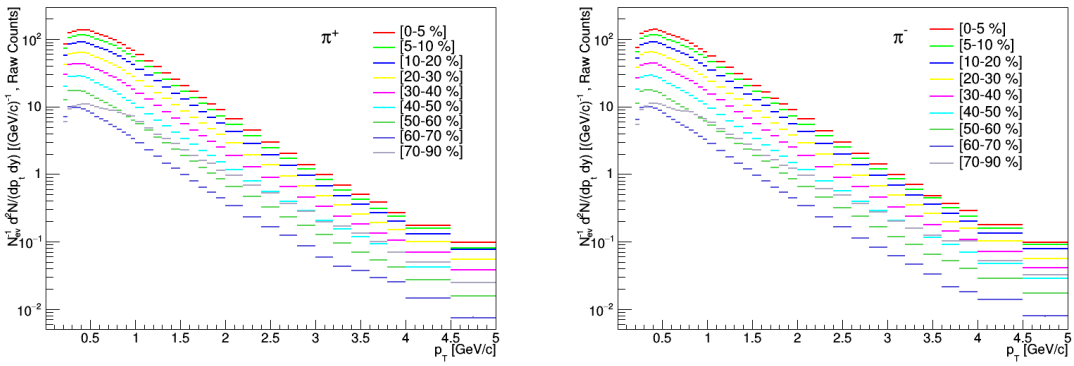

(a) Positive pions.

(b) Negative pions.

Figure 3.12: Pion raw spectra for different centrality classes.

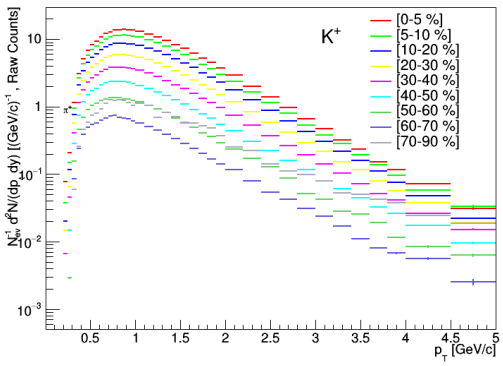

(a) Positive kaons.

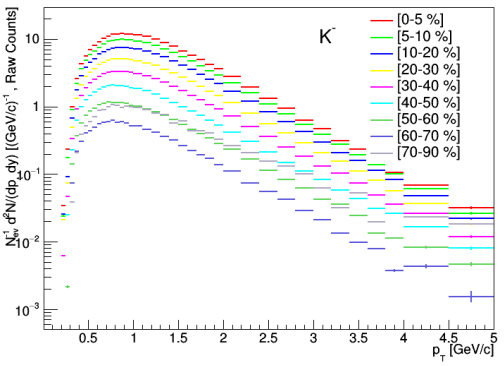

(b) Negative kaons.

Figure 3.13: Kaon raw spectra for different centrality classes.

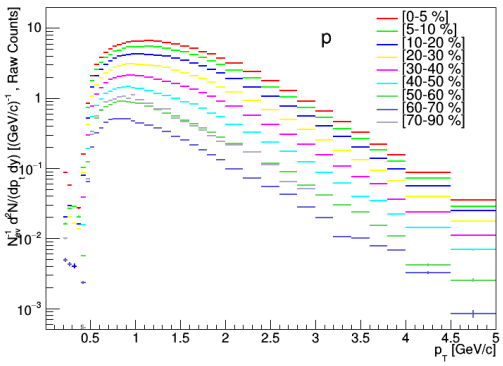

(a) Proton raw spectra.

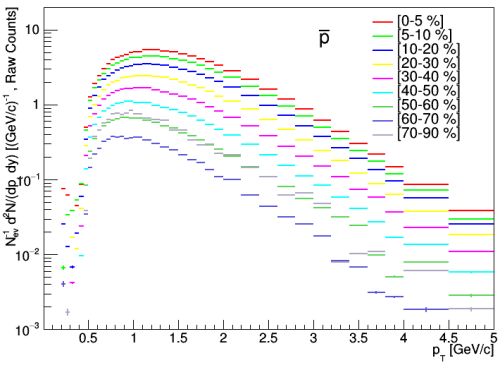

(b) Anti-proton raw spectra.

Figure 3.14: Proton raw spectra for different centrality classes.

3.5 Efficiency corrections

The efficiency corrections can be computed by considering the tracking efficiency as well as the matching efficiency of tracks to TOF. The overall efficiency corrections can be defined as reported in Eq. 3.10. The efficiencies have been computed with the HIJING [87] Monte Carlo for Xe–Xe collisions, convoluted with the full simulation and reconstruction of the ALICE detector.

$$\epsilon_{tot} = \epsilon_{tracking} \times \epsilon_{matching} \tag{3.10}$$

Tracking efficiency

The tracking efficiency (Eq. 3.11) is defined as the ratio between the number of tracks that are reconstructed by the global tracking (for the TPC tracks) and those which are generated. Only primary particles are considered at both numerator and denominator. Monte Carlo (MC) truth on the particle identity is required. Reconstructed tracks have to pass the same cuts the data do. The shape of the tracking efficiency correction depends strongly on the cuts used for track selection. Above all, the non-monotonous behavior of the tracking efficiency is due to the cut on the geometric track length in TPC, removing tracks which cross dead regions of the TPC and granting better agreement with the Monte Carlo simulation. Tracking efficiencies are shown for MB Xe–Xe collisions in Figg. 3.15, 3.16 and 3.17 for π, K, p respectively, while in Fig. 3.18 efficiencies are shown as a function of centrality, and in Fig. 3.19 the ratios between the efficiencies in the many centralities and the MB are shown. No significant dependence has been found and therefore we used the efficiency corrections determined in the MB sample to determine the final spectra.

Here follows a summary of the common requirements:

- Primary particles
- $|y| < 0.5$

- $|\eta| < 0.8$
- Required physics selection
- Required event selection
- Monte Carlo truth on PID (π, K or p)

$$\epsilon_{tracking} = \frac{\text{Tracks reconstructed}_{\text{MC PID, primaries,}|y|<0.5,|\eta|<0.8}}{\text{Particles generated}_{\text{MC PID, primaries,}|y|<0.5,|\eta|<0.8}} \tag{3.11}$$

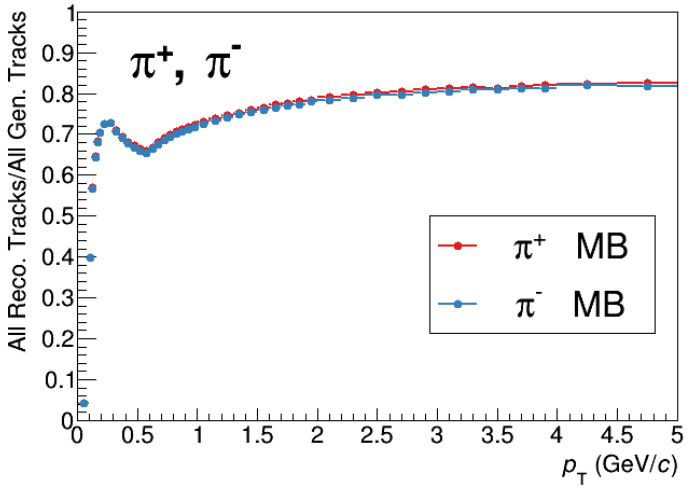

Figure 3.15: Tracking efficiency for π.

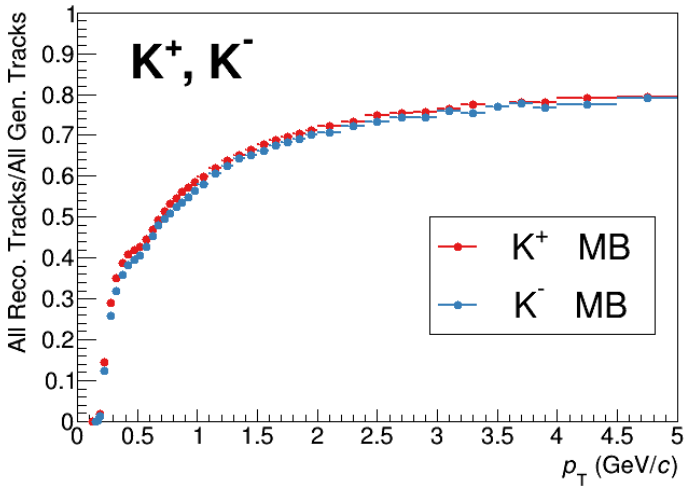

Figure 3.16: Tracking efficiency for K.

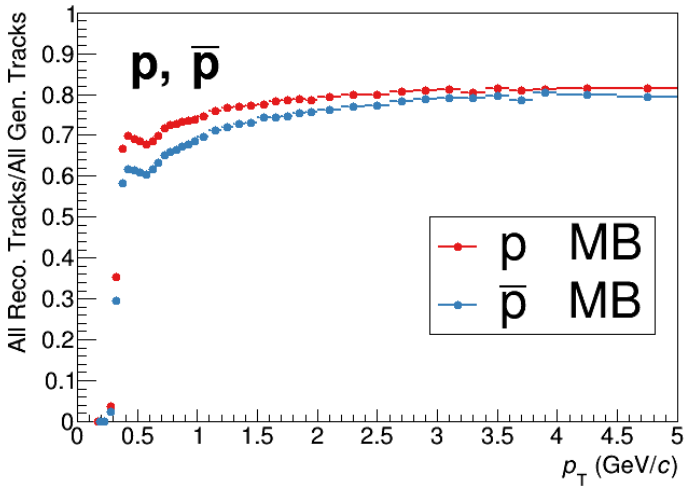

Figure 3.17: Tracking efficiency for p.

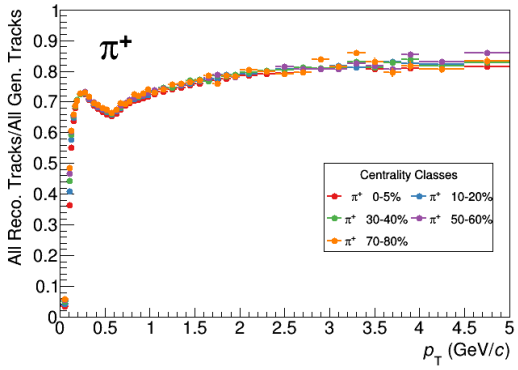

(a) Tracking efficiency for π^+.

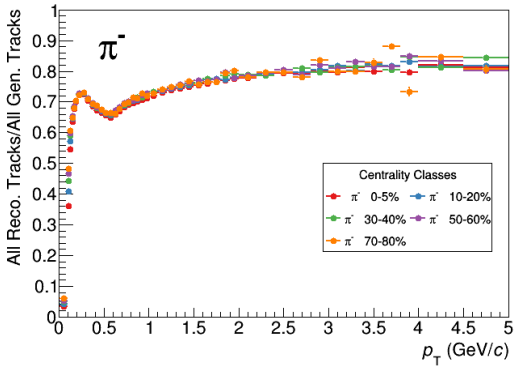

(b) Tracking efficiency for π^-.

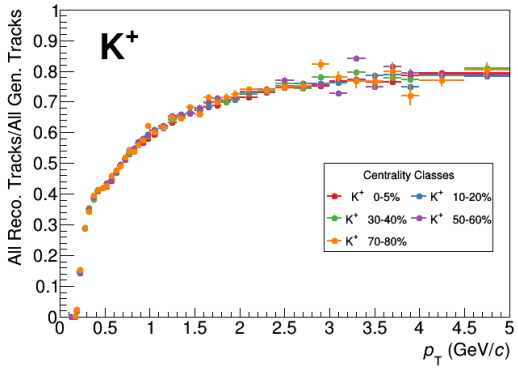

(c) Tracking efficiency for K^+.

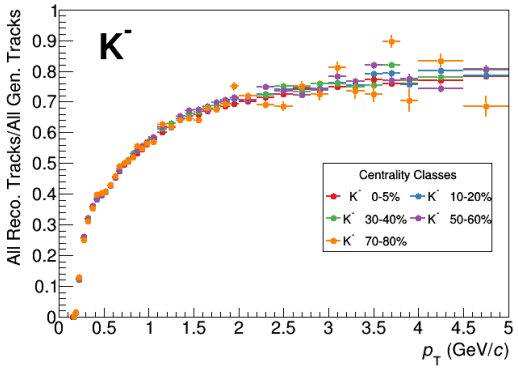

(d) Tracking efficiency for K^-.

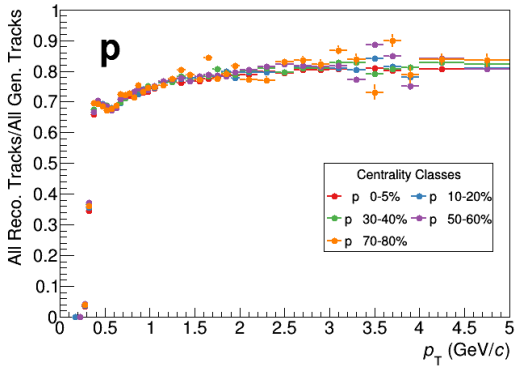

(e) Tracking efficiency for p.

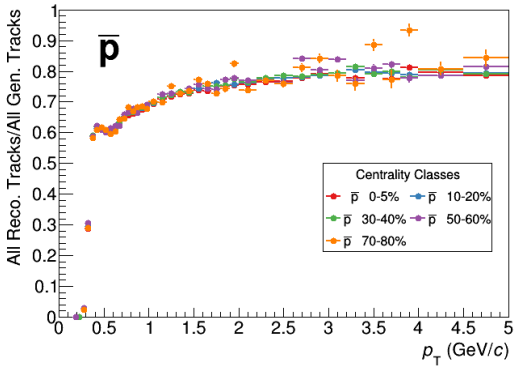

(f) Tracking efficiency for $\bar{p}$.

Figure 3.18: Tracking efficiency for both positive and negative π, K and p as measured in each centrality class in Xe–Xe collisions.

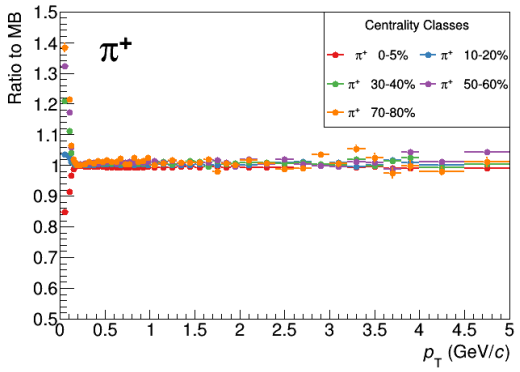

(a) Tracking efficiency for π^+.

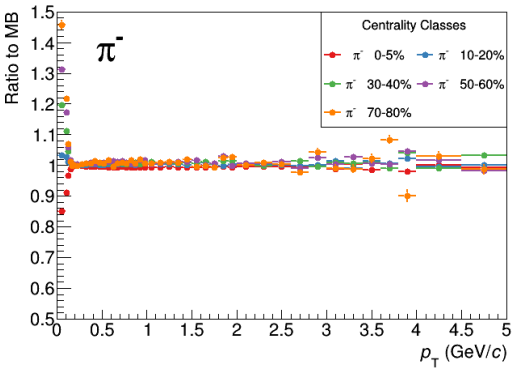

(b) Tracking efficiency for π^-.

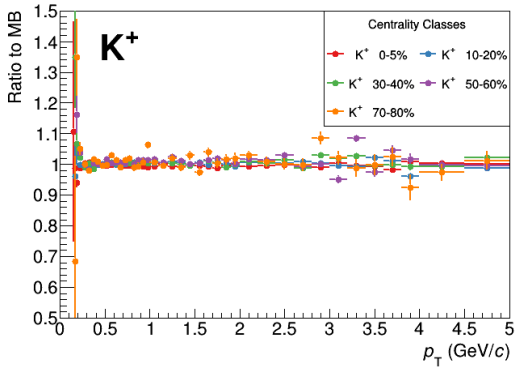

(c) Tracking efficiency for K^+.

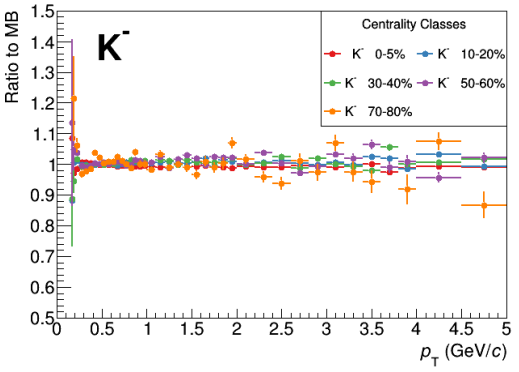

(d) Tracking efficiency for K^-.

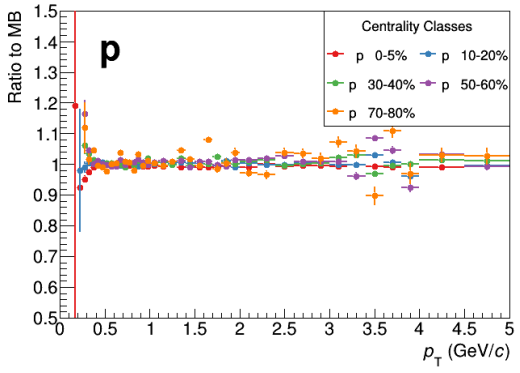

(e) Tracking efficiency for p.

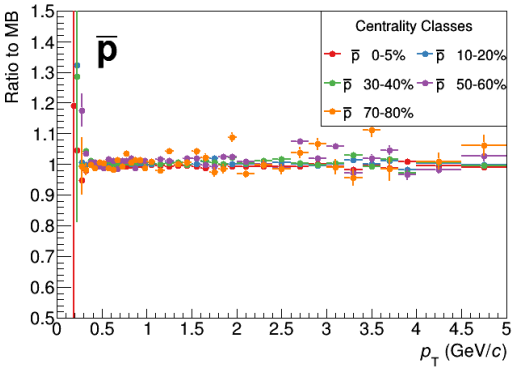

(f) Tracking efficiency for $\bar{p}$.

Figure 3.19: Tracking efficiency for both positive and negative π, K and p as measured in each centrality class in Xe–Xe collisions scaled to the MB inclusive sample.

Matching efficiency

The matching efficiency is obtained by computing the ratio between the tracks which are matched to TOF and the tracks reconstructed in TPC. By construction the denominator of the matching efficiency is equal to the numerator of the tracking efficiency. Matching efficiencies are shown for MB Xe–Xe collisions in Figg. 3.20, 3.21 and 3.22 for π, K, p respectively, while in Fig. 3.23 efficiencies are shown as a function of centrality, and in Fig. 3.24 the ratios between the efficiencies in the many centralities and the MB are shown. No significant dependence has been found and also in this instance we employ the MB corrections for all the centrality classes.

$$\epsilon_{matching} = \frac{\text{Tracks matched to TOF}_{\text{True Match, MC PID, primaries, } |y|<0.5,|\eta|<0.8}}{\text{Tracks reconstructed}_{\text{MC PID, primaries, } |y|<0.5,|\eta|<0.8}} \tag{3.12}$$

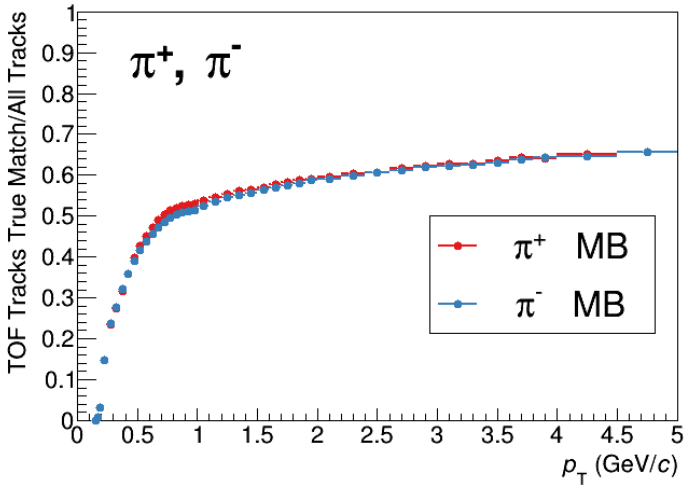

Figure 3.20: Matching efficiency for π.

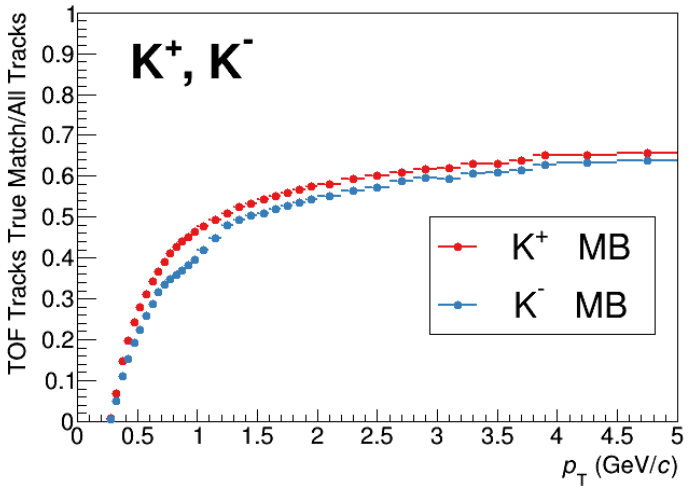

Figure 3.21: Matching efficiency for K.

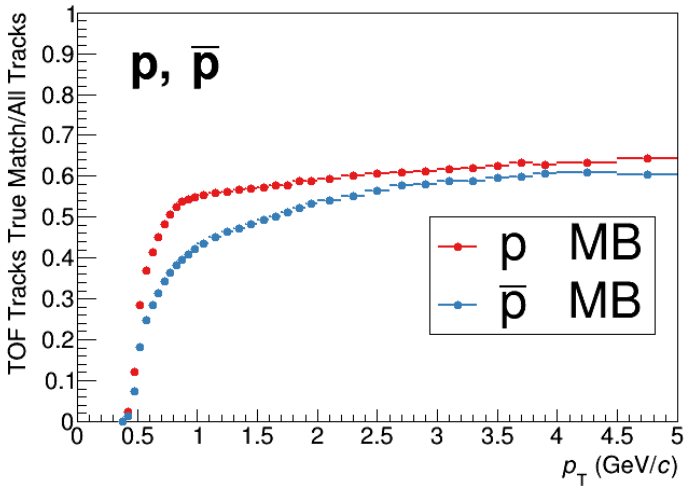

Figure 3.22: Matching efficiency for p.

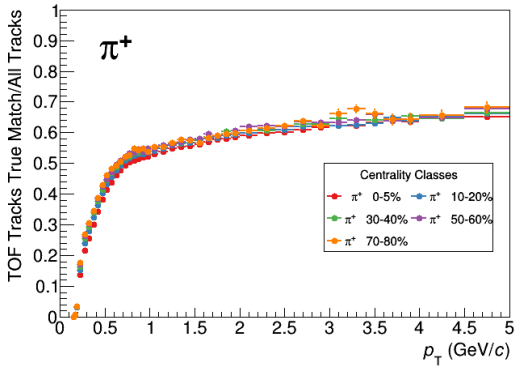

(a) Matching efficiency for π^+.

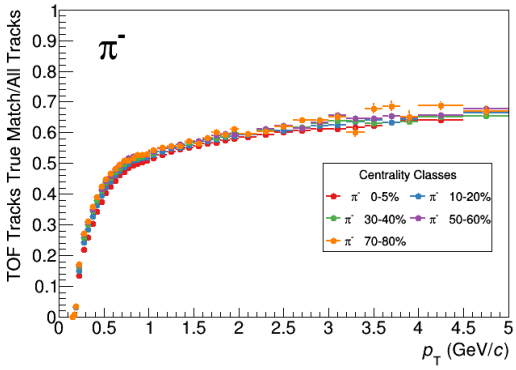

(b) Matching efficiency for π^-.

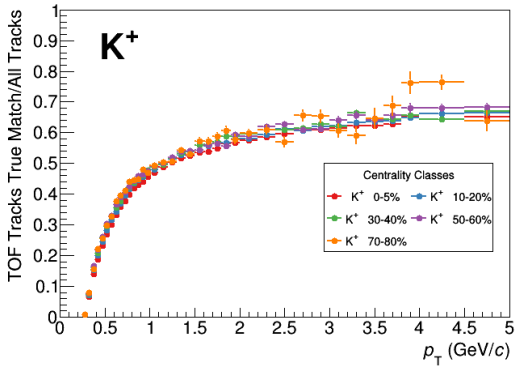

(c) Matching efficiency for K^+.

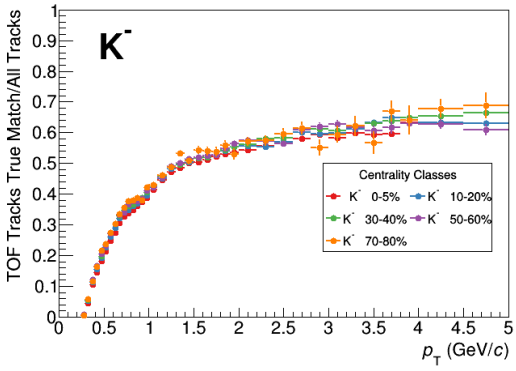

(d) Matching efficiency for K^-.

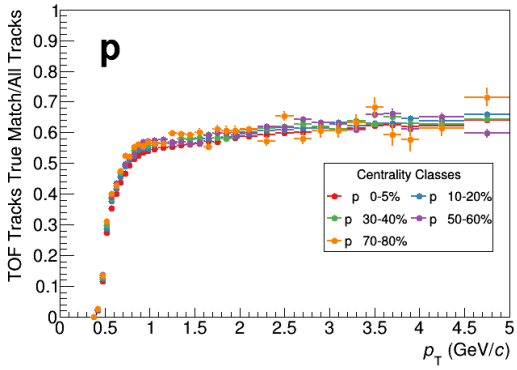

(e) Matching efficiency for p.

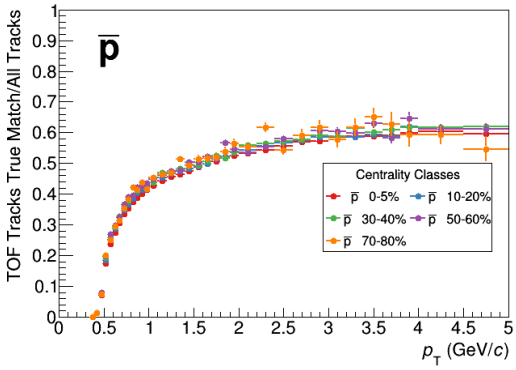

(f) Matching efficiency for $\bar{p}$.

Figure 3.23: Matching efficiency for both positive and negative π, K and p as measured in each centrality class in Xe–Xe collisions.

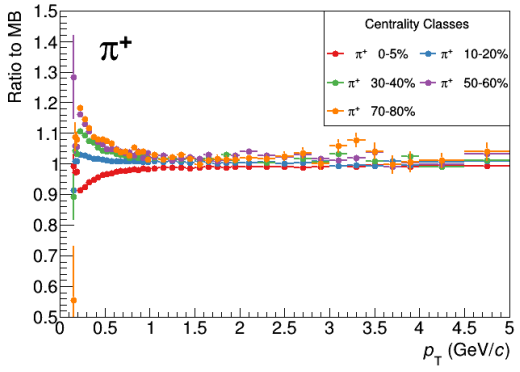

(a) Matching efficiency for π^+ vs centrality scaled to MB.

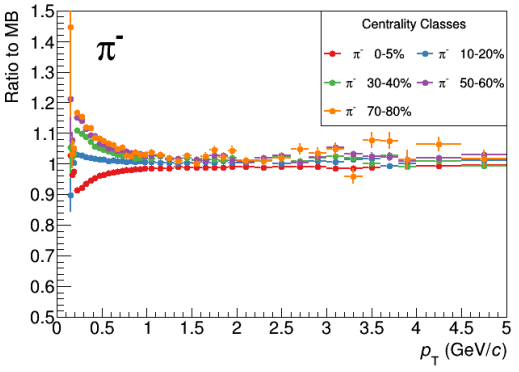

(b) Matching efficiency for π^- vs centrality scaled to MB.

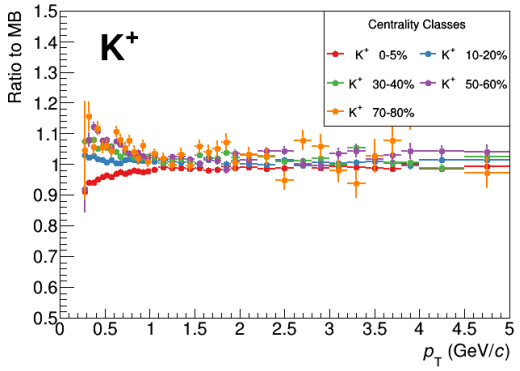

(c) Matching efficiency for K^+ vs centrality scaled to MB.

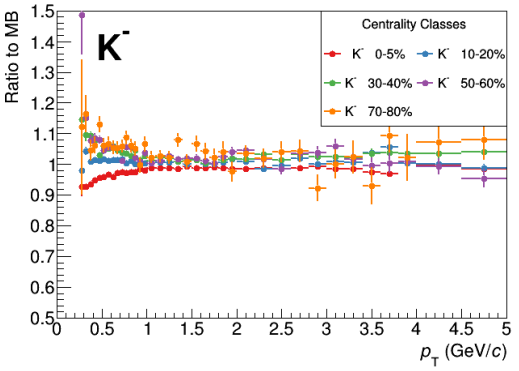

(d) Matching efficiency for K^- vs centrality scaled to MB.

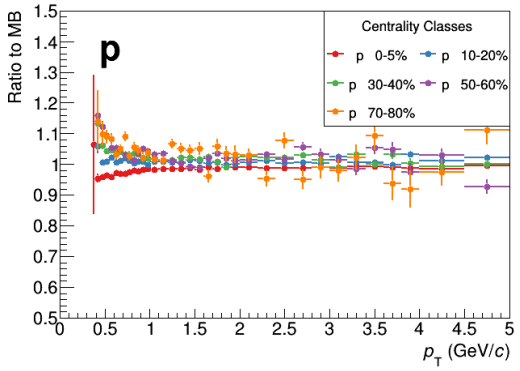

(e) Matching efficiency for p vs centrality scaled to MB.

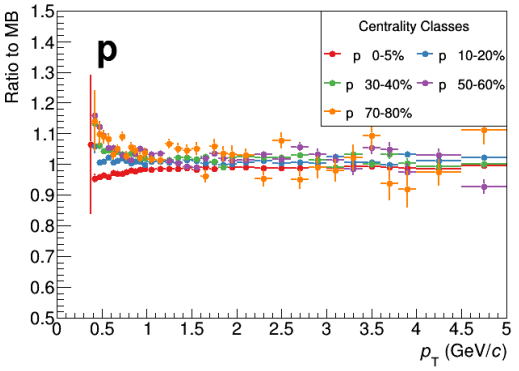

(f) [Matching efficiency for $\bar{p}$ vs centrality scaled to MB.

Figure 3.24: Matching efficiency for both positive and negative π, K and p as measured in each centrality class in Xe–Xe collisions scaled to the MB inclusive sample.

3.6 Systematic Uncertainties

The systematic uncertainties on this analysis have been estimated mainly performing the parameter variation. Other general contributions affecting charged particles have been directly taken from the non-identified spectra analysis on Xe–Xe data [88]. All these contributions are added in quadrature and summarized in Tab. 3.3.

The effect of the selection of events based on the vertex position had been studied by comparing the fully corrected p_{T} spectra obtained with alternative vertex selections corresponding to ± 5 cm, and ± 20 cm. The difference in the fully corrected p_{T} spectra is less than 0.3% for central collisions and less than 0.5% for peripheral collisions.

In order to test the description of the detector response and the track reconstruction in the simulation, all criteria for track selection had been varied within the ranges. A full analysis had been performed by varying one selection criterion at a time. The maximum change in the corrected p_{T} spectrum is then considered as systematic uncertainty. The overall systematic uncertainty related to track selection had been obtained from summing up all individual contributions quadratically and it amounts to 0.6-3.0%, depending on p_{T} and centrality. This has been checked in our analysis too, using the same variation technique, for instance varying the χ^2 of the tracks (between 4, being the standard requirement, 3 and 5), or the number of traversed TPC rows (between 70, being the standard requirement, 60 and 80), and the requests on the geometrical cut. It has been noted that we are consistent with the other analysis.

The difference in the TPC-ITS track-matching efficiency between data and simulation is assigned to the corresponding systematic uncertainty. It amounts to 2% in central collisions, and up to 3.5% in peripheral collisions.

A difference in the amount of detector material budget leads to different amounts of secondary particles that are produced. A variation of the material leads to a p_{T} dependent systematic uncertainty on the tracking efficiency of 0.1-0.3%.

The uncertainty due to the finite p_{T} resolution is estimated using the azimuthal dependence

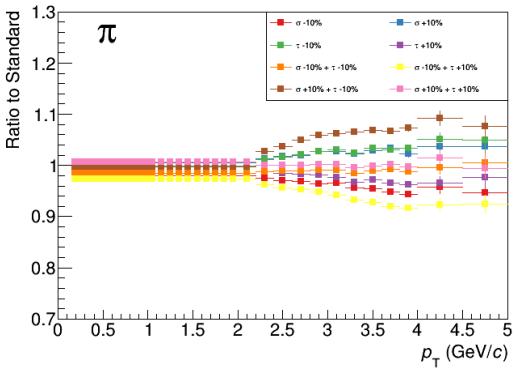

(a) PID variation π.

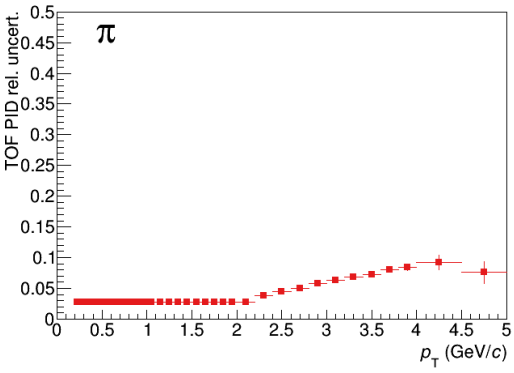

(b) TOF PID relative uncert. for π.

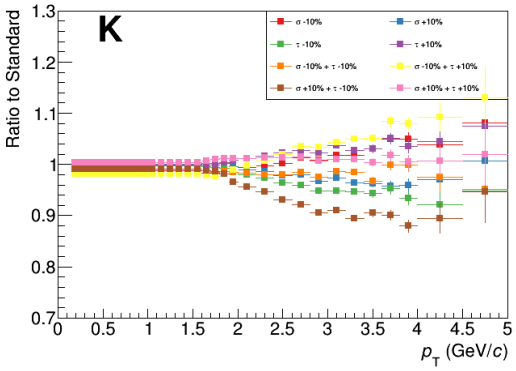

(c) PID variation K.

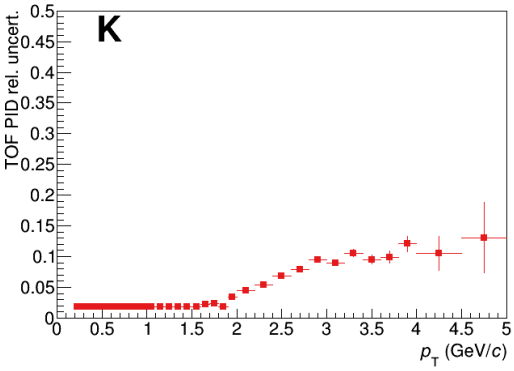

(d) TOF PID relative uncert. for K.

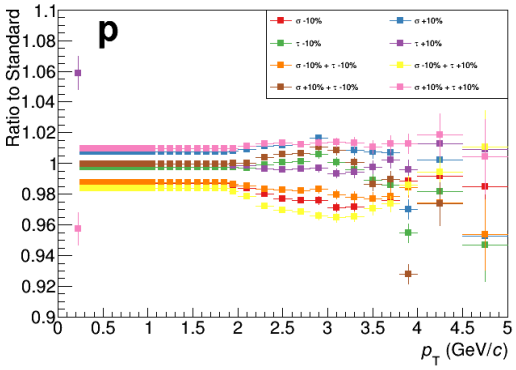

(e) PID variation p.

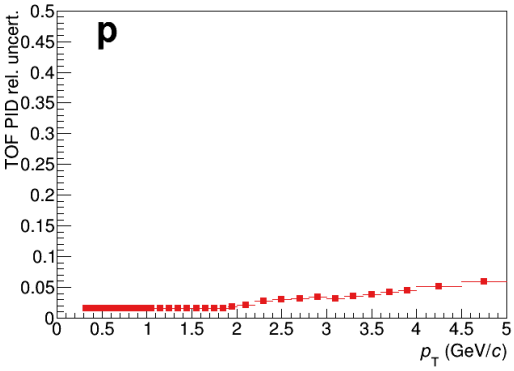

(f) TOF PID relative uncert. for p.

Figure 3.25: PID variations for π, K and p in Xe–Xe collisions for the TOF analysis.

of the $1/p_{\mathrm{T}}$-spectra for positively and negatively charged particles. The relative shift of the spectra for oppositely charged particles along $1/p_{\mathrm{T}}$ determines the size of uncertainty for a given angle. The RMS of the $1/p_{\mathrm{T}}$-shift as distributed over the full azimuth is used as an additional increase of the p_{T} resolution. The uncertainty due to the finite p_{T} resolution is significant only at the highest momentum bin and amounts to 0.5% (0.9%) for the 0-5% (70-80%) centrality class.

The uncertainty due to the centrality determination is estimated by changing the fraction of the visible cross section. The uncertainty is estimated from the variation of the resulting p_{T}-spectra and amounts to $\sim$0.1% and $\sim$3.2% for central (0-5%) and peripheral (70-80%) collisions, respectively.

Concerning the PID variations, the procedure was the following: the tail and the sigma of the signal have been modified by a $\pm$10% both separately and at the same time, to check how the raw spectra get modified if compared to the standard parameterization, as it is shown in Fig. 3.25, where every point in Figg. 3.25b, 3.25d, 3.25f is the difference between the corresponding widest spread apart points on the PID variations. The results are that the effect is 3%, 2% and 2% for π, K, p respectively for $p_{\mathrm{T}} < 2$ GeV/c, while it gets higher at higher p_{T}, reaching 9%, 12% and 5% for π, K, p respectively.

Another systematic source is due to the fact that the tracks reaching the TOF detector have to cross a substantial amount of additional material budget (about 23%X/X$_0$), mostly from the TRD. The systematic uncertainties on the TOF matching were estimated comparing the matching efficiency evaluated in Monte Carlo and from data using samples of cleanly identified particles in TPC. Good agreement is observed with deviations at the level of at most 2%, 4%, 6%, 6%, 4% and 6% for π^+, π^-, K$^+$, K$^-$, p and $\bar{\mathrm{p}}$ respectively, over the full p_{T} range [89].

Uncertainties in the estimate of contamination from secondary particles can arise from differences in the fitting procedure used for the DCA_{xy} distributions using either $Roofit$ or $TFractionFitter$. The relative difference between the two results goes as an additional systematic source, $< 0.3\%$ and $\sim 1\%$ for pions and protons respectively.

Another thing that should be pointed out is that the mismatch accounts for only the 1-2% of the raw spectra, so any change to the parametrization of the mismatch template converts in an effect that is negligible compared to the other contributions to the systematic uncertainty.

species	π	K	p
p_{T} – range [GeV/c]	0.2-0.5/1-2	0.2-0.5/1-2	0.2-0.5/1-2
Source			
Vertex selection	0.2/0.2 [0-5 %]	0.2/0.2 [0-5 %]	0.2/0.2 [0-5 %]
	0.8/0.8 [30-80 %]	0.8/0.8 [30-80 %]	0.8/0.8 [30-80 %]
Track selection	1.6/0.9 [0-5 %]	1.6/0.9 [0-5 %]	1.6/0.9 [0-5 %]
	0.9/0.6 [30-40 %]	0.9/0.6 [30-40 %]	0.9/0.6 [30-40 %]
	0.9/0.5 [70-80 %]	0.9/0.5 [70-80 %]	0.9/0.5 [70-80 %]
Tracking efficiency	1.9/1.2 [0-5 %]	1.9/1.2 [0-5 %]	1.9/1.2 [0-5 %]
	2.2/1.2 [30-40 %]	2.2/1.2 [30-40 %]	2.2/1.2 [30-40 %]
	2.2/1.4 [70-80 %]	2.2/1.4 [70-80 %]	2.2/1.4 [70-80 %]
Material budget	0.3/0.3	0.3/0.3	0.3/0.3
p_{T} resolution	*negligible*	*negligible*	*negligible*
PID variations	3 [0.5-2 GeV/c]	2 [0.5-2 GeV/c]	2 [0.5-2 GeV/c]
	9 [4-5 GeV/c]	12 [4-5 GeV/c]	5 [4-5 GeV/c]
Matching efficiency	2 [π^+]	6 [K^+]	4 [p]
(TPC-TOF)	4 [π^-]	6 [K^-]	6 [$\bar{\mathrm{p}}$]
Secondaries	< 0.3	-	~ 1
Sum. p_{T} dependent			
0-5 %	4.5(5.4)/4.0(5.3) $\pi^+(\pi^-)$	6.9/6.5	5.2(6.9)/4.8(6.5) p($\bar{\mathrm{p}}$)
30-40 %	4.5(5.4)/3.9(5.2) $\pi^+(\pi^-)$	6.9/6.5	5.2(6.9)/4.7(6.5) p($\bar{\mathrm{p}}$)
70-80 %	4.5(5.4)/4.1(5.4) $\pi^+(\pi^-)$	6.9/6.6	5.2(6.9)/4.9(6.6) p($\bar{\mathrm{p}}$)
Centrality selection	0.1 [0-5 %]	0.1 [0-5 %]	0.1 [0-5 %]
	0.8 [30-40 %]	0.8 [30-40 %]	0.8 [30-40 %]
	3.2 [70-80 %]	3.2 [70-80 %]	3.2 [70-80 %]

Table 3.3: Contributions to the systematic uncertainties expressed as percentages. Where indicated, single contributions refer only to the corresponding centrality classes or to the p_{T} bin indicated.

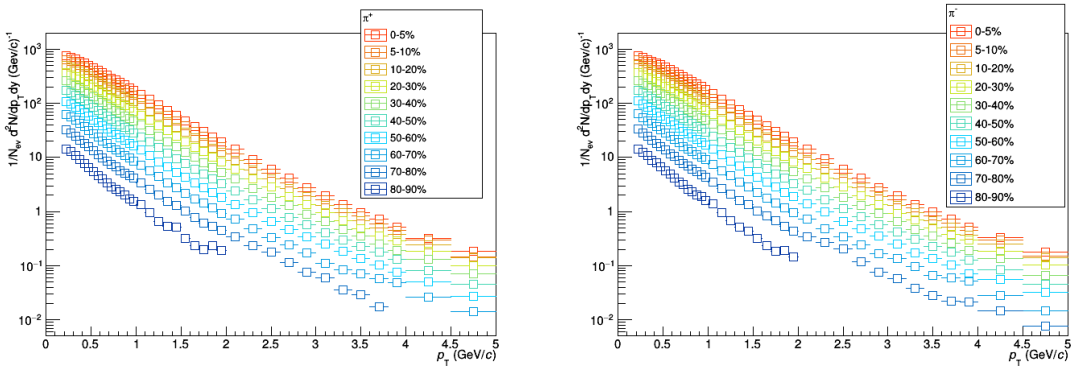

(a) Spectra for π^+.

(b) Spectra for π^-.

Figure 3.26: Spectra for charged pions as measured in Xe–Xe collision at $\sqrt{s_{\rm NN}} = 5.44$ TeV for the different centrality classes taken into account.

3.7 Corrected spectra

The TOF raw yields have been corrected for efficiency and feed-down in order to get the final spectra, after having been normalized by the number of events. The corrected results are shown in the following. Spectra are shown in the full range where the yield extraction procedure is feasible. The $p_{\rm T}$ used for the combination of the different analyses is obtained by reducing the spectra ranges shown in Figg. 3.26, 3.27 and 3.28 (the corrected spectra for the π, K, p respectively) to the ones reported in Table 3.1. Due to large statistical fluctuations in the computed efficiency, especially in peripheral centrality bins, the efficiency corrections used to obtain the corrected spectra are computed from MB events. This is not the case for the primary fraction which is computed and applied for each centrality separately.

$$\frac{dN}{dp_{\rm T}dy} = \frac{1}{N_{\text{Ev. after all selections}}} \frac{dN}{dp_{\rm T}dy} \times \frac{1}{\epsilon_{tracking}} \times \frac{1}{\epsilon_{matching}} \times f_{primary\ fraction} \tag{3.13}$$

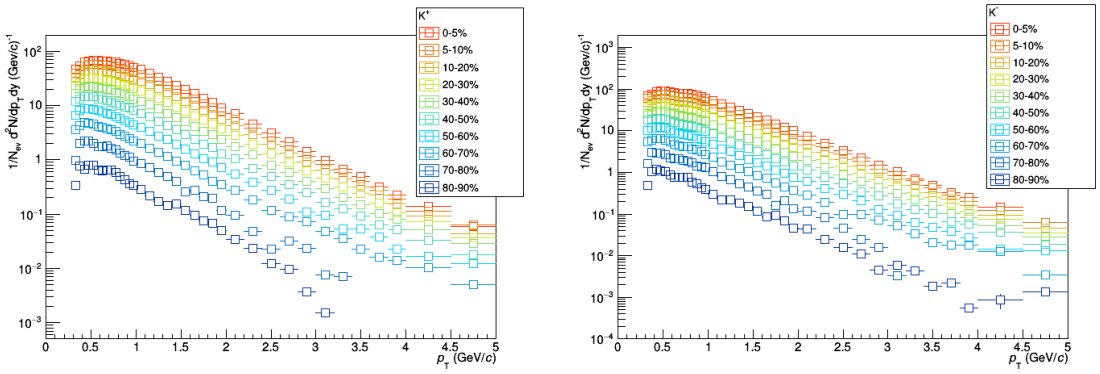

(a) Spectra for K^+. (b) Spectra for K^-.

Figure 3.27: Spectra for charged kaons as measured in Xe–Xe collision at $\sqrt{s_{\rm NN}} = 5.44$ TeV for the different centrality classes taken into account.

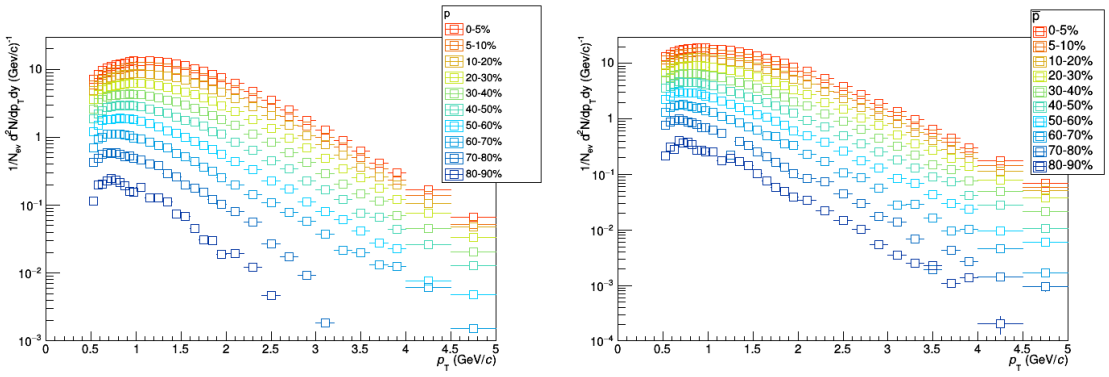

(a) Spectra for p. (b) Spectra for $\bar{\rm p}$.

Figure 3.28: Spectra for protons and anti-protons as measured in Xe–Xe collision at $\sqrt{s_{\rm NN}} = 5.44$ TeV for the different centrality classes taken into account.

Chapter 4

Results

4.1 Combined spectra

The combined spectra (considering all the analyses i.e. ITS, TPC, TOF) for π^++π^-, K^++K^- and p+$\bar{p}$ and all the related results in all the centrality bins are presented in this section.

Final combined pion, kaon and proton spectra In Fig. 4.1, 4.2, and 4.3, the combined spectra for π^++π^-, K^++K^- and p+$\bar{p}$ are shown for Xe–Xe collisions at $\sqrt{s_{NN}} = 5.44$ TeV. For the combination, the p_T ranges listed in Table. 3.1 have been used for the different analyses and the weighted average has been calculated for the spectrum points superimposed in p_T, with the systematics and statistical errors (summed in quadrature) as weights. In addition, half of the difference between the different spectra has been assigned as an additional systematic source.

In the high-p_T part of the spectra in this Xe–Xe analysis, the points with a statistical error greater than 30% have been excluded.

The change of shapes with centrality is fully manifested especially in the K and p spectra: the spectra get harder with increasing centrality. The spectra for all particle species have a basically exponential shape at high p_T in central collisions. As expected from a naive

hydrodynamical scenario, the heavier the particle the harder the spectra. This is much more obvious going firstly from pions to kaons and then to protons.

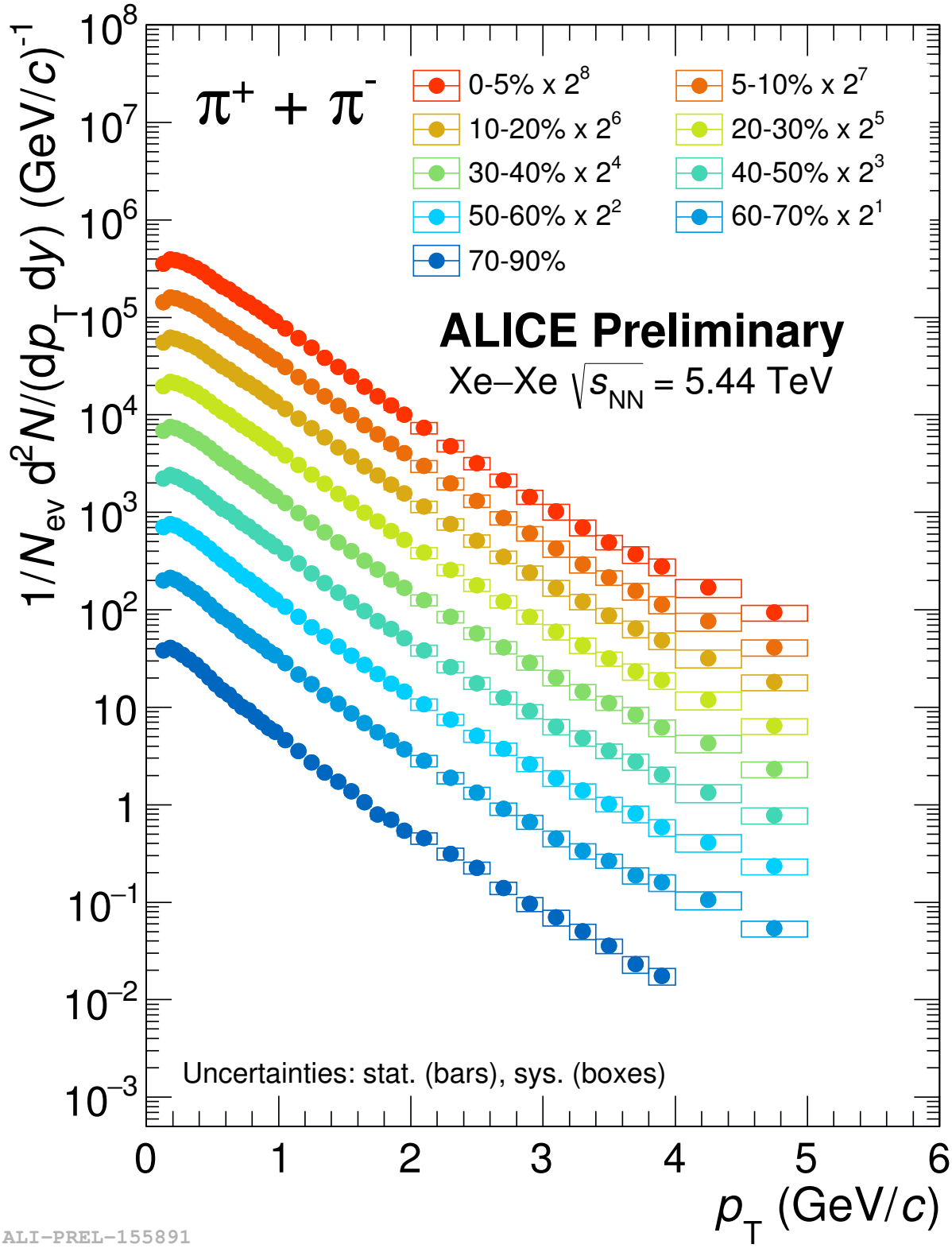

Figure 4.1: Combined spectra for π for all the centrality classes considered in Xe–Xe collisions at $\sqrt{s_{\rm NN}} = 5.44$ TeV. High-$p_{\rm T}$ points with a statistical uncertainty greater than 30% have been removed.

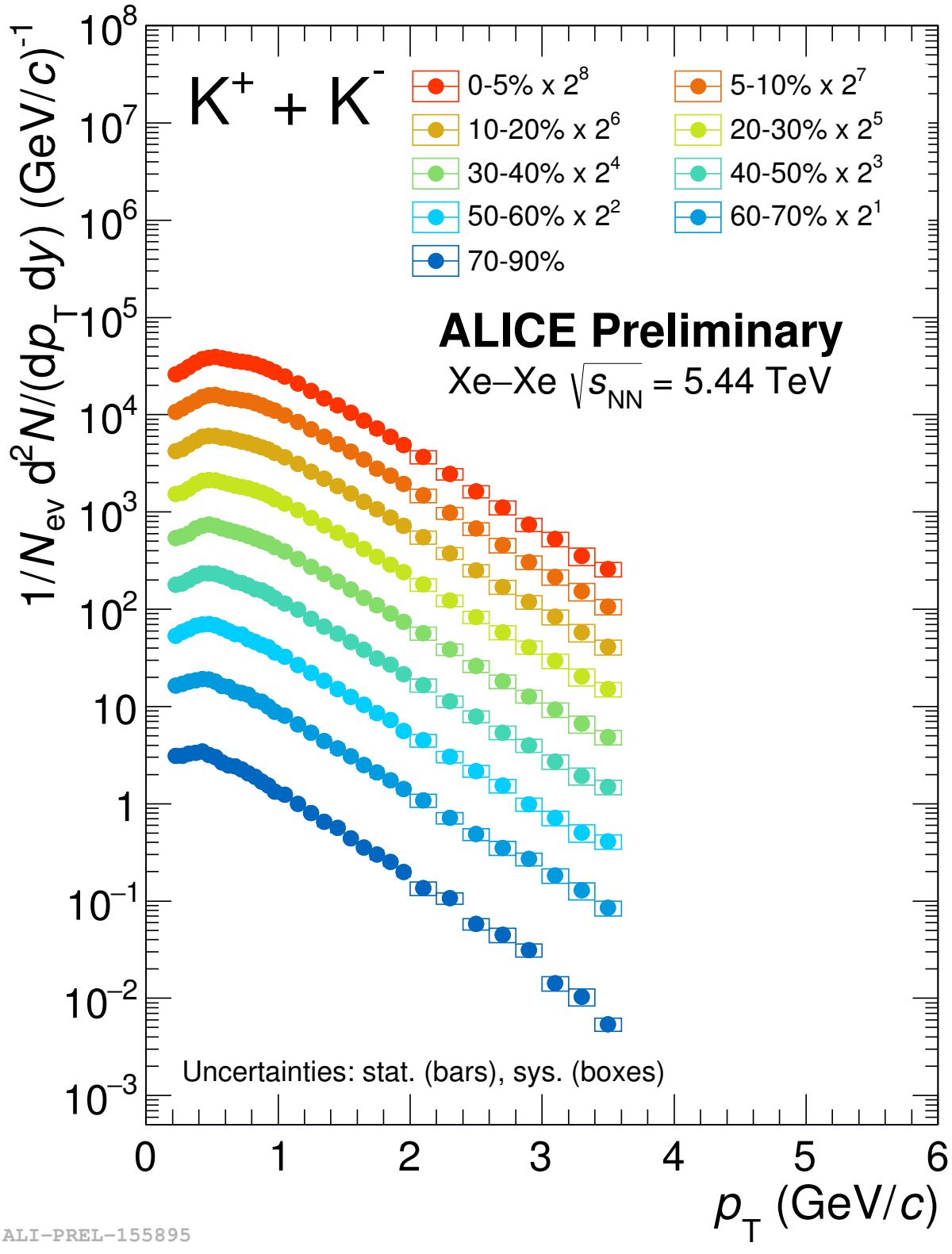

Figure 4.2: Combined spectra for K for all the centrality classes considered in Xe–Xe collisions at $\sqrt{s_{\rm NN}} = 5.44$ TeV. High-$p_{\rm T}$ points with a statistical uncertainty greater than 30% have been removed.

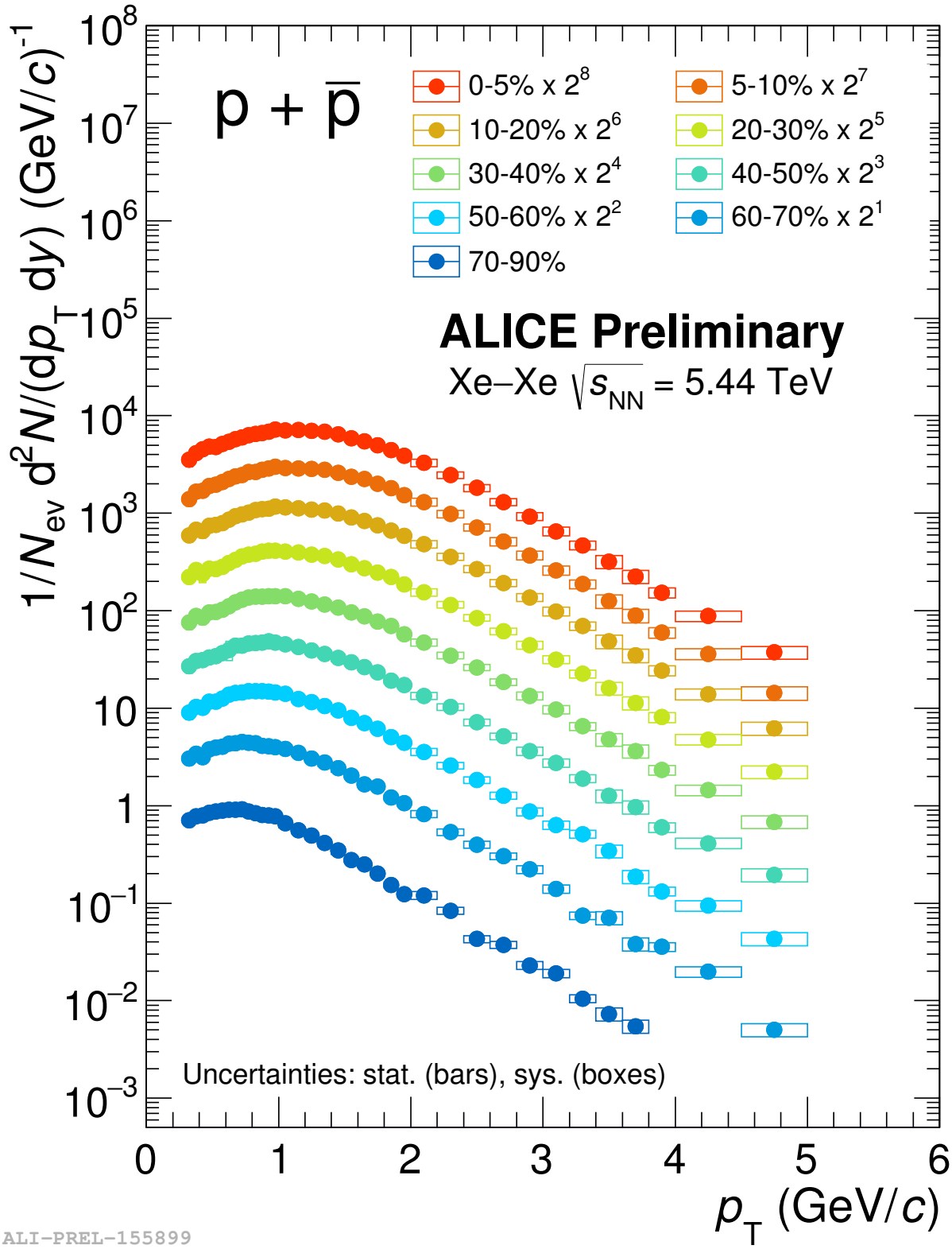

Figure 4.3: Combined spectra for p for all the centrality classes considered in Xe–Xe collisions at $\sqrt{s_{\rm NN}} = 5.44$ TeV. High-$p_{\rm T}$ points with a statistical uncertainty greater than 30% have been removed.

4.2 R_{CP}

The transverse momentum distributions we have been focusing on so far, should also depend on centrality since more central collisions are more likely to come to thermal equilibrium. Thus in addition to comparing with a pp reference process (R_{AA}), the centrality of the collision can be studied by taking the ratio of the results in central collisions to those in more peripheral collisions, especially useful if no pp reference data is available. This central to peripheral ratio is known as R_{CP} where C is for central and P is for peripheral. The denominator is typically the most peripheral bin with meaningful statistics. Measurements of R_{CP} indicate that it is also less than unity. As the numerator of R_{CP} goes from the most central bin to more peripheral bins, R_{CP} increases toward unity, as we can see from Fig. 4.4.

The R_{CP} has proven to be a powerful tool for the study of parton propagation in the dense QCD medium expected to be formed in nucleus-nucleus collision since RHIC's times [90]. Its definition is as following [91]:

$$R_{\mathrm{CP}} = \frac{\langle N^{P}_{collisions} \rangle}{\langle N^{C}_{collisions} \rangle} \cdot \frac{d^2 N^{C}_{\mathrm{AA}}/dp_{\mathrm{T}}dy}{d^2 N^{P}_{\mathrm{AA}}/dp_{\mathrm{T}}dy} \ . \tag{4.1}$$

where $d^2 N^{C(P)}_{\mathrm{AA}}/dp_{\mathrm{T}}dy$ is the number of particles in the more central (peripheral) bin at mid-rapidity as a function of p_{T} and $\langle N^{C(P)}_{collisions} \rangle$ is the mean number of collisions for the most central (peripheral) bin.

As it is shown inside Fig. 4.4, the three particle species behave similarly for all the centrality bins involved, showing medium-absorption effects (being less than unity).

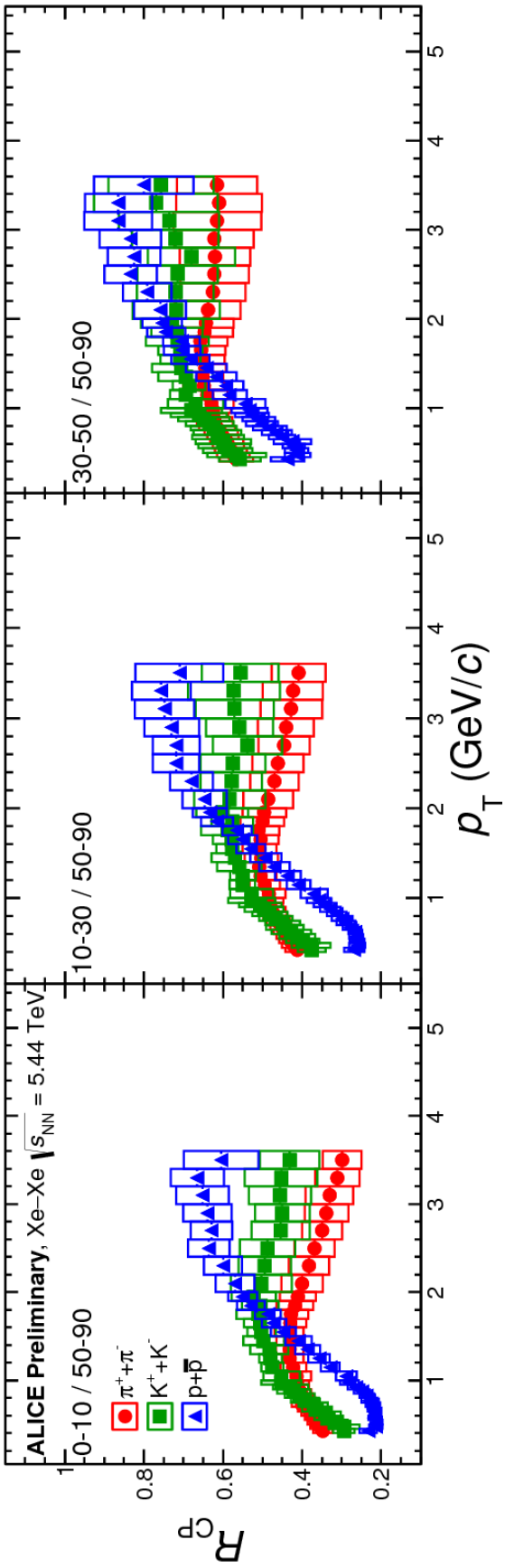

Figure 4.4: R_{CP} as obtained with the Xe–Xe data at $\sqrt{s_{\mathrm{NN}}} = 5.44$ TeV.

4.3 Particle ratios

Figg. 4.5 and 4.6 show the $\mathrm{p}/\pi \equiv (\mathrm{p}+\bar{\mathrm{p}})/(\pi^+ + \pi^-)$ and $\mathrm{K}/\pi \equiv (\mathrm{K}^+ + \mathrm{K}^-)/(\pi^+ + \pi^-)$ ratios as a function of p_T. Both ratios are seen to increase as a function of centrality at intermediate p_T with a corresponding depletion at low p_T. The p/π ratio, in particular, shows a more pronounced increase. It should be noted that a rise of the ratio with p_T is an intrinsic feature of hydrodynamical models, where it is just due to the mass ordering induced by radial flow (heavier particles are pushed to higher p_T by the collective motion). Both figures show the ratios obtained for Pb–Pb and Xe–Xe spectra.

K/π and p/π ratios measured in Pb–Pb and Xe–Xe overlap when compared at the same event multiplicity (but different centralities), suggesting that it is the multiplicity that governs the expansion rather than centrality.

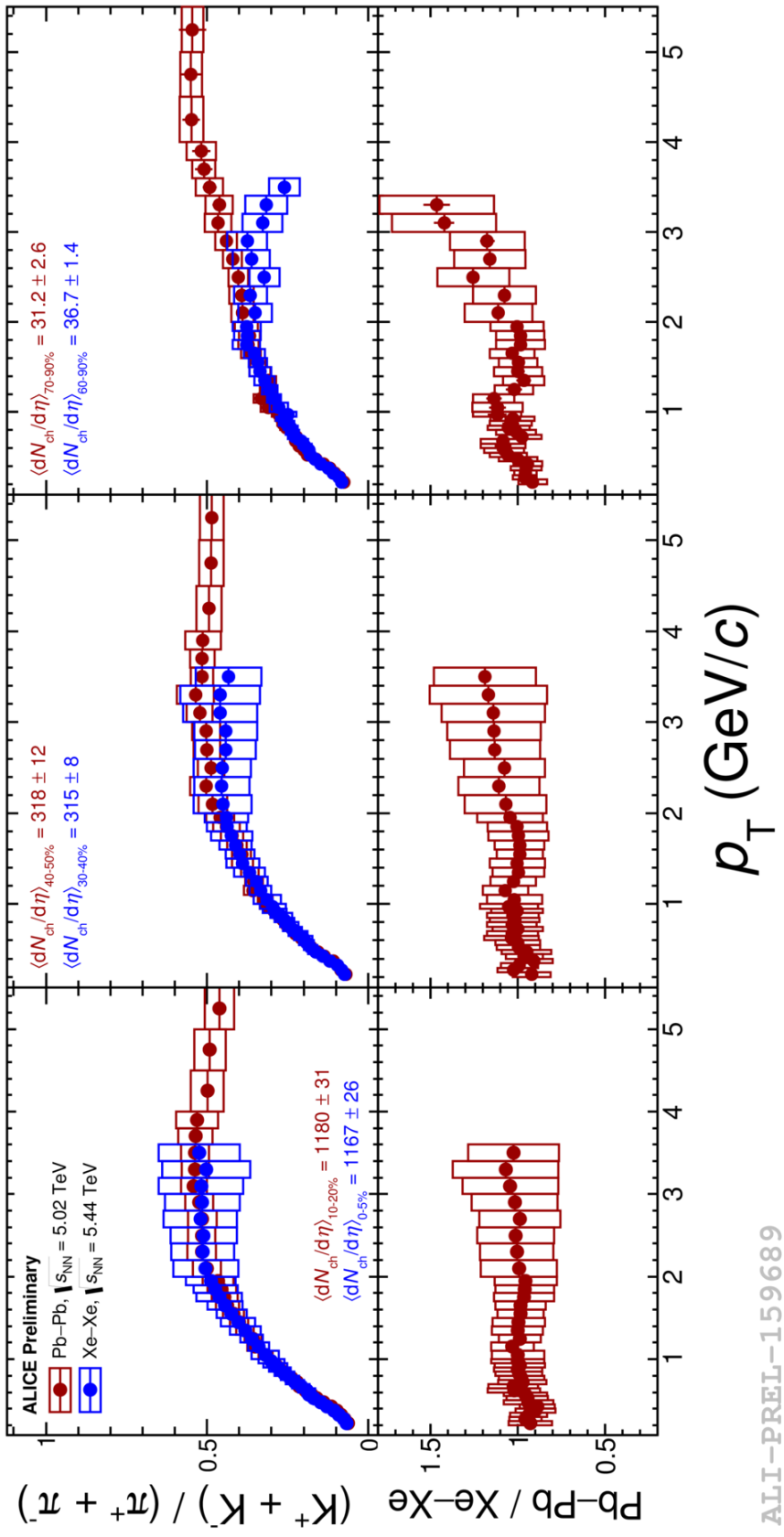

Figure 4.5: Kaon-to-pion ratio at similar multiplicities in Pb–Pb at $\sqrt{s_{NN}} = 5.02$ TeV and Xe–Xe at $\sqrt{s_{NN}} = 5.44$ TeV. The ratios Pb–Pb / Xe–Xe are also shown. Three different cases are shown: high, mid, low multiplicity.

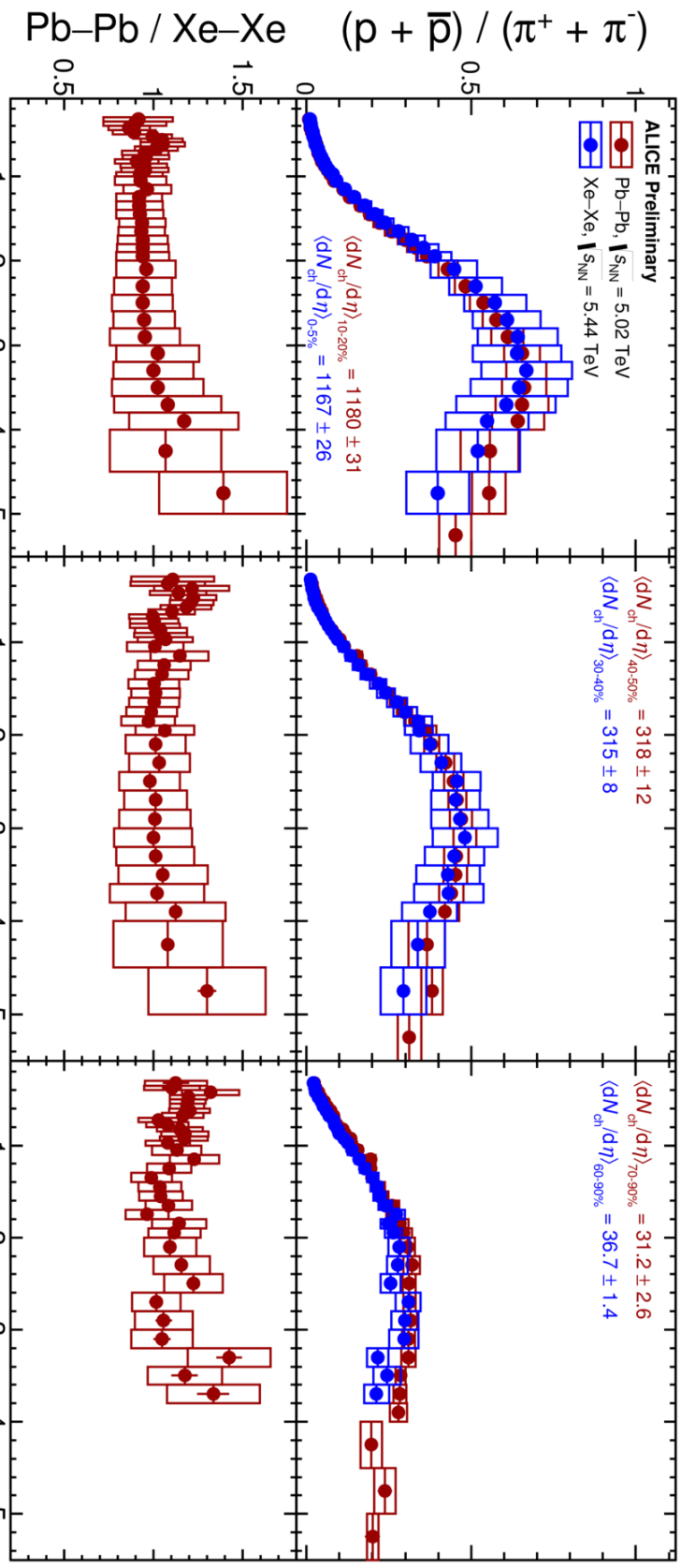

Figure 4.6: Proton-to-pion ratio at similar multiplicities in Pb–Pb at $\sqrt{s_{\rm NN}} = 5.02$ TeV and Xe–Xe at $\sqrt{s_{\rm NN}} = 5.44$ TeV. The ratios Pb–Pb / Xe–Xe are also shown. Three different cases are shown: high, mid, low multiplicity.

4.4 Blast-wave

Heavy-ion collisions are complex, and there are several different models trying to explain their features. One of these models is the blast-wave model, which describes the dynamics of the kinetic freeze-out phase. The main idea is that the hadrons suddenly decouple simultaneously and the freeze-out happens at the same time. This results in a transverse two-dimensional (2D) hydro parametrization blast-wave that boosts the particles created in the collision. The hadrons get boosted according to their mass via the local flow velocity. The first assumption of the model is that the particles detected in heavy-ion collisions are only radiated from a thermal source with temperature T. There are more effects that the model has to consider, related to the boost-invariant longitudinal expansion and transverse flow. When everything is added up, the model results in a blast-wave function given by:

$$\frac{1}{p_{\mathrm{T}}}\frac{dN}{dp_{\mathrm{T}}} \propto \int_0^R dr \cdot r \cdot m_T \cdot I_0\left(\frac{p_T \sinh\rho}{T_{kin}}\right) \cdot K_1\left(\frac{m_T \cosh\rho}{T_{kin}}\right) \tag{4.2}$$

where

$$I_n(x) = \left(\frac{x}{2}\right)^n \sum_{k=0}^{\infty} \frac{\left(x^2/4\right)^k}{k! \cdot \Gamma(n+k+1)}$$

and

$$K_n(x) = \frac{\pi}{2} \cdot \frac{I_{-n} - I_n}{\sin(n\pi)}$$

with R the fireball radius, T_{kin} the temperature of the kinetic freeze-out and finally

$$\rho = \tanh^{-1}\left(\beta_T\right) \equiv \tanh^{-1}\left(\left(\frac{r}{R}\right)^{n_0} \cdot \beta_s\right)$$

where β_T is the transverse expansion velocity, n_0 is the velocity profile's exponent and β_s is the transverse expansion velocity at the surface. So, we can finally fit our p_{T}-spectra using the blast-wave parameterization as shown in Fig. 4.7 for the centrality class [5-10 %]. A combined blast-wave fit of the spectra has been performed in the p_{T} ranges 0.5-1.0 GeV/c, 0.2-1.5 GeV/c and 0.3-3.0 GeV/c for pions, kaons and protons, respectively.

Ultimately, the simultaneous fit to all particle species under consideration can provide insight on the (common) kinetic freeze-out properties of the system. It has to be kept in mind, however, that the actual values of the fit parameters depend substantially on the fit range.

Despite this limitation, the blast-wave model still proves to be a handy way to compare the transverse momentum distributions and their evolution in different collision systems.

A detailed study of the spectral shapes has been done in order to give a quantitative estimate of the thermal freeze-out temperature T_{kin} and the average transverse flow $\langle\beta_T\rangle$. The results obtained on the thermal freeze-out show that in central nucleus-nucleus collisions T_{kin} is relatively larger than in peripheral collisions.

A non-zero $\langle\beta_T\rangle$ of the produced particles is considered in peripheral nucleus-nucleus collisions. The peripheral collisions contain a few participant nucleons that take part in the violent interactions. This situation is similar to small collision systems which also contains a few participant nucleons.

Shown in Fig. 4.8 are the parameters $\langle\beta_T\rangle$ and T_{kin} of the Blast-Wave model for all collision systems studied so far. For Pb–Pb and Xe–Xe data, the parameters are shown for all the centrality classes under investigation, and for all the energies available for the Pb–Pb only (2.76 TeV and 5.02 TeV). For small systems, like pp and p–Pb, the different points correspond to multiplicity classes. Basically speaking, going from lower to higher $\langle\beta_T\rangle$ means moving from more peripheral to more central collisions for large systems while for small systems means going up in multiplicity. It can be seen that for large systems, Xe–Xe and Pb–Pb show an extremely similar behaviour. The obtained values for T_{kin}, β_T for all the centrality classes involved are summarized in Tab. 4.1.

Centrality	T_{kin} **[MeV]**	$\langle\beta_T\rangle$
[0-5 %]	95.9±8.8	0.651±0.007
[5-10 %]	96.0±8.7	0.651±0.007
[10-20 %]	96.0±8.6	0.645±0.007
[20-30 %]	98.2±8.7	0.632±0.007
[30-40 %]	100.1±8.7	0.616±0.008
[40-50 %]	104.7±8.8	0.593±0.009
[50-60 %]	113.4±9.3	0.56±0.01
[60-70 %]	128±10	0.51±0.01
[70-90 %]	155±9	0.39±0.02

Table 4.1: Results for the Blast-Wave fit in the Xe–Xe analysis.

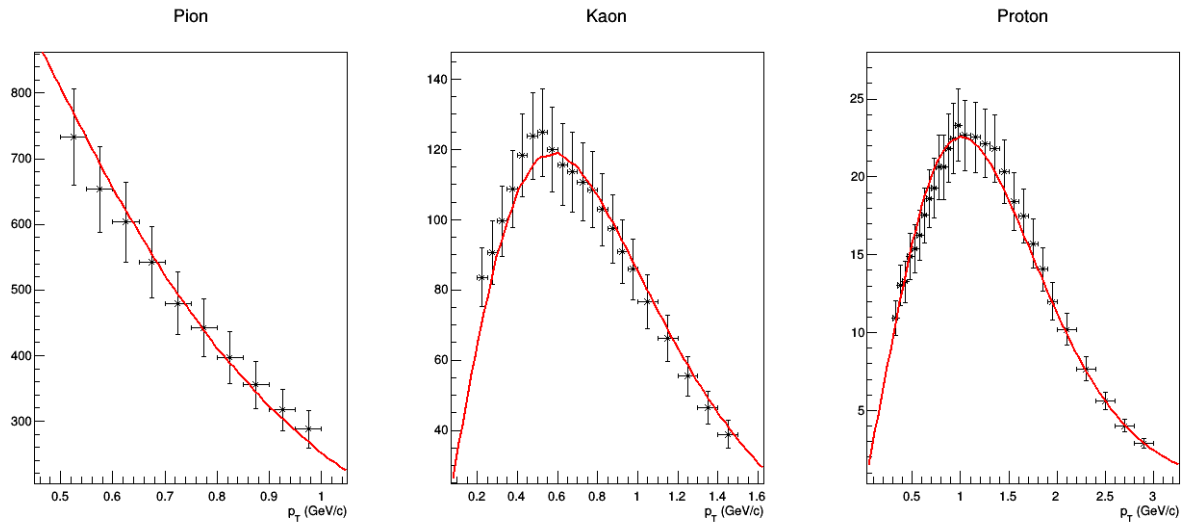

Figure 4.7: Blast-Wave fit to the centrality class [5-10%].

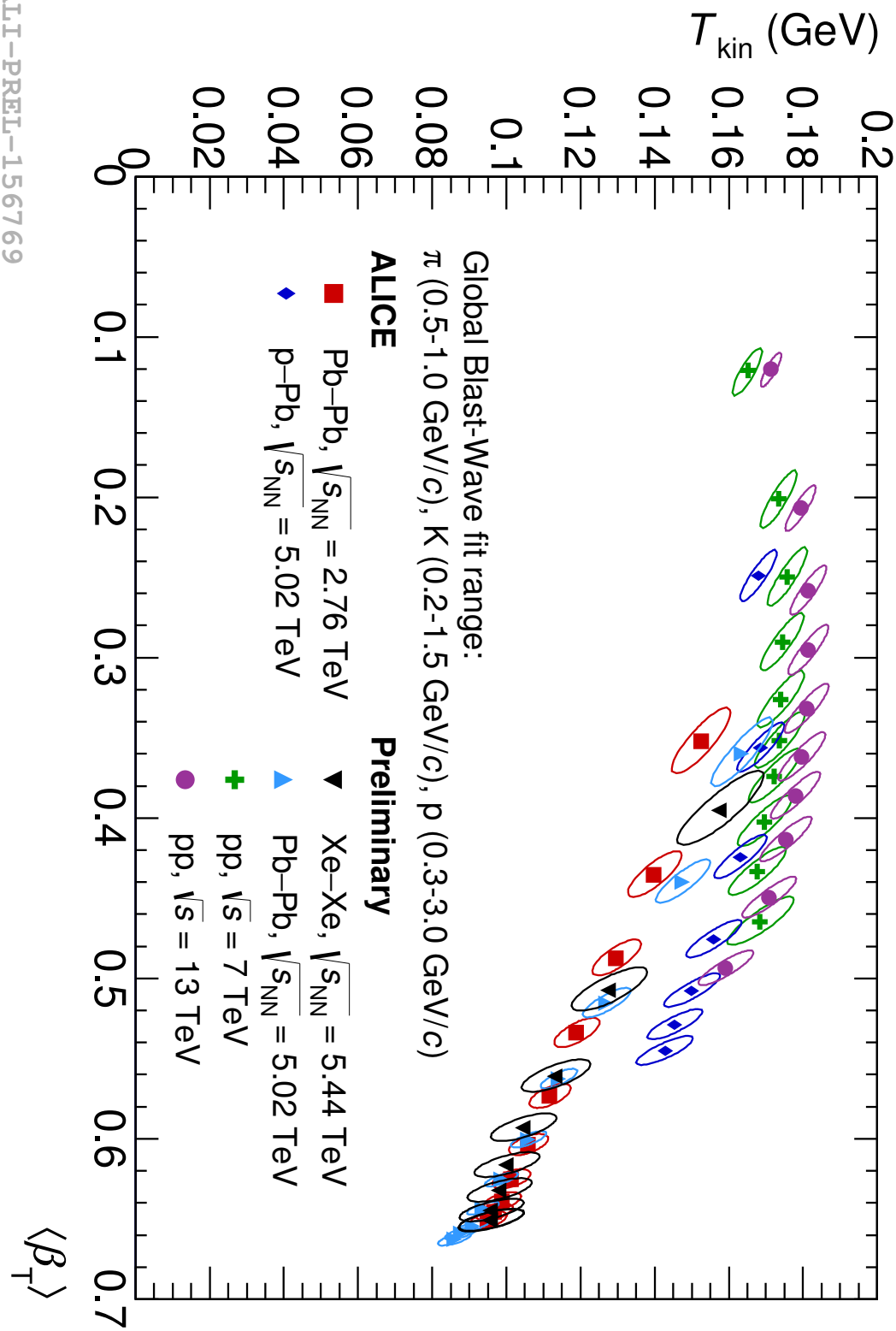

Figure 4.8: Blast-wave fits for all colliding systems considered until now.

Conclusions

This thesis has been focusing on the measurement of the p_{T}-spectra of pions, kaons and protons in Xe–Xe collisions at $\sqrt{s_{\mathrm{NN}}} = 5.44$ TeV with the Time-Of-Flight system of the ALICE experiment, and these spectra have been combined with those obtained for ITS and TPC with different analyses. The importance of said spectra has been more than once highlighted. It has been shown how the spectra exhibit the features we expect from hydrodynamics, so how the spectra get harder and harder as the mass of the species of interest gets higher, or how the centrality is involved, so spectra get harder going from peripheral to more central collisions. It has been shown how the spectra may provide us with information over the latter stages of the QGP formation, so how to extract temperature and flow expansion velocity. The Blast-Wave results highlight how the $\langle\beta_T\rangle$ goes from a lower to a higher value moving to more central collisions while instead the T_{kin} increases going from central to peripheral collisions. Furthermore Xe–Xe and Pb–Pb data show a remarkably similar behaviour.

Similar behaviour between the two A–A collision systems is also observed for the K/π and the p/π ratios when the spectra are compared for similar multiplicities. The p/π ratio in particular exhibits the familiar shoulder-like structure, remnant of the hardening of the p_{T}-spectra due to mass ordering.

With all this remarkable results, it is worth noting that this is a standard but very important measurement to do whenever a new collision system is involved, and it fits perfectly to these new Xe–Xe data, although lack of statistics hurts whenever we go to more peripheral collisions due to the limited amount of available data (two runs corresponding to 1.3 M of

MB events) available.

Appendix A

Centrality

The system produced in a nucleus-nucleus collision is expected to be closer to the conditions necessary for quark-gluon plasma production if more nucleons are involved in the initial collision. Thus the closer the collision is to *head-on*, or the more **central** a collision is, the more likely plasma production will be. More glancing or **peripheral** collisions are less likely to lead to ideal conditions for plasma production. This is referred to as **centrality**.

Several variables are used to quantify collision centrality including the number of participants, $N_{\rm part}$, and the number of collisions, $N_{\rm coll}$. Both are given in terms of the impact parameter, b, the distance between the centers of two colliding nuclei. Low b corresponds to more central collisions, high b to peripheral collisions. Of course the impact parameter is not directly measurable but experience at the BNL AGS and CERN SPS has shown that the number of produced particles, the *multiplicity*, and the energy of the produced particles in the transverse direction, the transverse energy, $E_{\rm T}$, are both proportional to the number of nucleon participants, see Fig. A.1. Thus since the dependence of $N_{\rm part}$ on impact parameter can be calculated rather precisely for a given nuclear density distribution, we can get a good handle on the collision centrality. There are several different measurements that can be performed to determine the centrality of a collision. These include for example the comparison of transverse energy production to energy going forward, and particle production or multiplicity, with transverse energy and multiplicity rather closely connected.

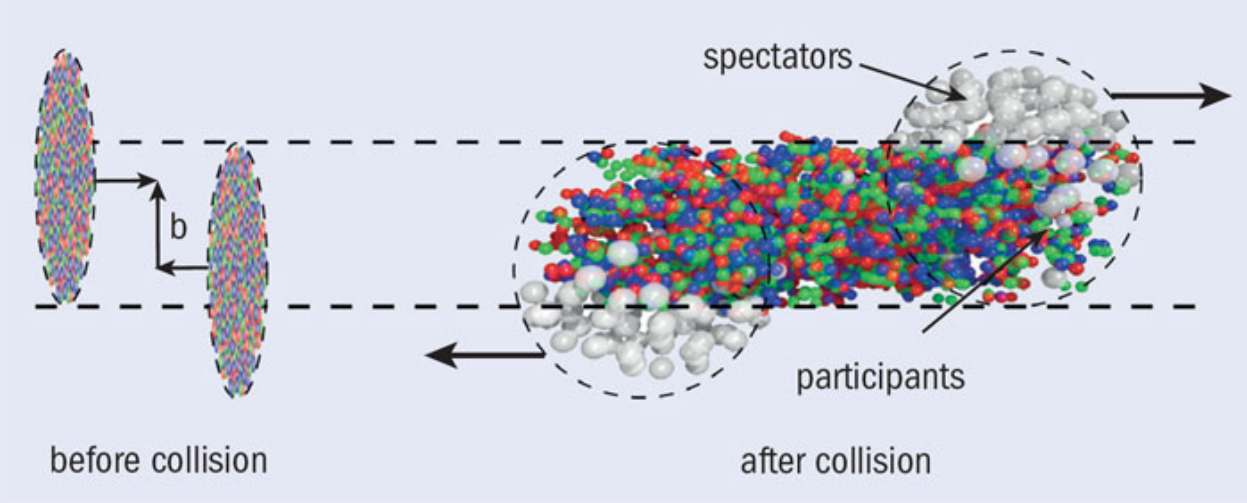

Figure A.1: The picture of a nucleus-nucleus collision. The impact parameter and the number of participants are shown too.

In a hadron-hadron collision, some of the forward hadron momentum is converted to particle production. These produced particles are typically less energetic than the initial hadrons. The produced particles also generally have some energy directed transverse to the colliding hadrons. This energy is called transverse energy, E_{T}. In nucleus-nucleus collisions, each individual nucleon-nucleon collision contributes to the total transverse energy production. A comparison of the collision E_{T} to the energy of the *spectator* nucleons, those nucleons in the initial nuclei that did not take part in the collision but went down the beam pipe, is a good measure of centrality. The spectator energy is measured by *zero degree calorimeters*, (ZDCs) so named because they sit at zero degrees relative to the transverse direction. Thus E_{T} and E_{ZDC} are highly correlated.

Measurements such as the E_{T}, E_{ZDC} and multiplicity distributions are often divided into bins of centrality, such as the central 10% of all collisions, and it is possible to relate centrality bins to impact parameters by means of a chosen model.

Appendix B

Physically relevant quantities

Firstly, let us introduce some kinematic variables, useful in describing a particle's position and momentum. It is common to describe a particle's position and momentum in terms of four-vectors. In the case of position, the four-vector is represented as x^μ where $\mu = 0, 1, 2, 3$ and

$$x^\mu = (x^0, x^1, x^2, x^3) = (ct, x, y, z).$$

However, the spatial four vector is often collapsed to three components with the introduction of a transverse coordinate, $x_{\mathrm{T}}^2 = x^2 + y^2$, neglecting the azimuthal angle, so that

$$x^\mu = (ct, x_{\mathrm{T}}, z).$$

The momentum four-vector can be similarly defined so that

$$p^\mu = (p^0, p^1, p^2, p^3) = (E/c, p_x, p_y, p_z) = (E/c, p_{\mathrm{T}}, p_z)$$

where again

$$p_{\mathrm{T}}^2 = p_x^2 + p_y^2.$$

Moving on, it is worth mentioning two variables that are very convenient for describing particle kinematics, the *transverse mass* and the **rapidity**. The transverse mass, m_{T}, is related to the difference between the squares of the energy and longitudinal momentum, and it is invariant under Lorentz transformation

$$m_{\mathrm{T}} = E^2 - p_z^2 = m^2 + p_{\mathrm{T}}^2.$$

The rapidity of a particle can be defined either in terms of its energy and longitudinal momentum:

$$y = \frac{1}{2} \ln \frac{E + p_z}{E - p_z}$$

or its velocity, β, instead of the momentum and energy if we define its direction of motion to be along the z-axis since $\beta = p_z/E$

$$y = \frac{1}{2} \ln \frac{1 + \beta}{1 - \beta}.$$

Using the definition of rapidity:

$$E = m_{\mathrm{T}} \cdot \cosh y, \quad p_z = m_{\mathrm{T}} \cdot \sinh y.$$

We now examine two extreme instances and look at the particle rapidity. The first is when the velocity, β, is very small, $\beta \ll 1$. Then we can expand the numerator and denominator of the y definition to find $y \approx \beta$.

On the other hand, when the particle momentum is so high that the mass can be ignored, $p \gg m$, we can relate the rapidity to the **pseudorapidity**, η, and then to the angle of emission, θ. The pseudorapidity is often a more useful experimental measure, especially if the detected particles are not identified and their masses are thus unknown. We define the angle of particle emission relative to the z-axis as $\cos\theta = p_z/p$. As

$$E + p_z = \sqrt{p^2 + m^2} + p_z \approx p_z + p \cdot \left(1 + \frac{m^2}{2p^2} + \cdots\right)$$

and by introducing θ

$$E + p_z \approx 2p \cdot \left(\cos^2 \frac{\theta}{2} + \frac{m^2}{4p^2}\right).$$

It works exactly the same for

$$E - p_z \approx 2p \cdot \left(\sin^2 \frac{\theta}{2} + \frac{m^2}{4p^2}\right).$$

Dropping the second terms as $p \gg m$, it easy to see

$$y \approx -\ln \tan \frac{\theta}{2} = \eta$$

It is often more convenient to use rapidity for phenomenological calculations since the mass of the desired particle is known. On the other hand, pseudorapidity is typically used by us

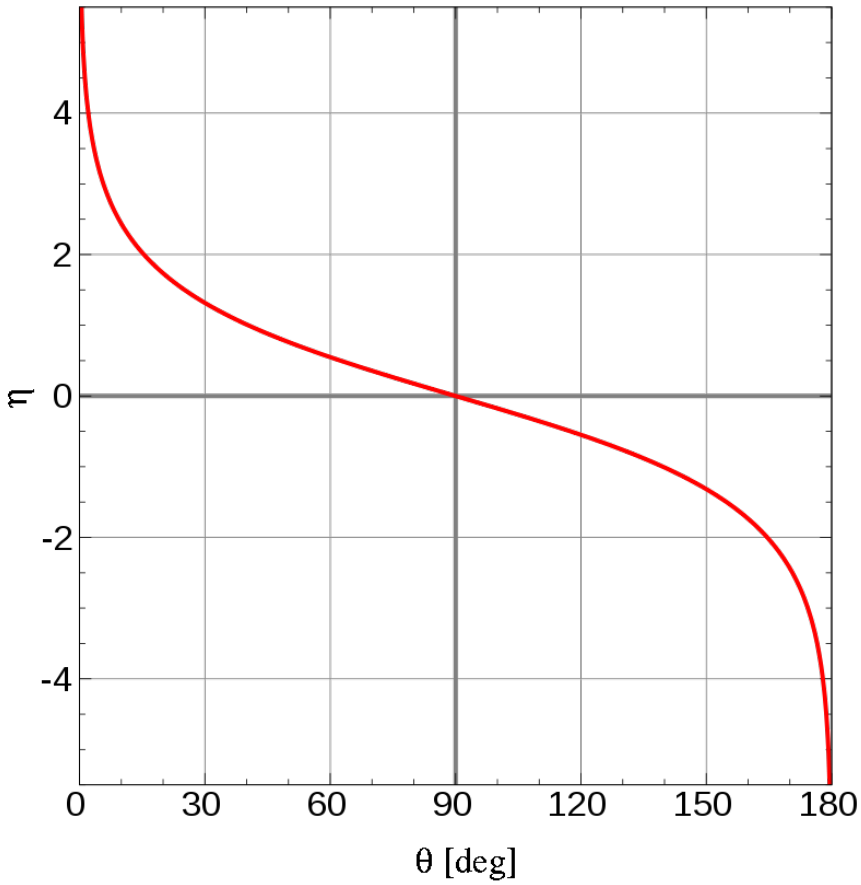

Figure B.1: Pseudorapidity as a function of the emission angle.

experimentalists for reasons of convenience. As stated above, if the measured particles are unidentified, then rapidity cannot be defined as above. In addition, a typical detector or detector component covers some well-defined θ region with respect to the beam axis, making pseudorapidity a natural variable to use.

Acknowledgements

It feels like these five years have gone in a flash. Five years of hard work, where I have learnt all sort of stuff. I have always wanted to be involved in this kind of field, and finally I am at that threshold, ready to embark on my Ph.D. studies. Quite a few people have helped in this journey, and while many difficulties have honed me over time, their help has molded the me of today. As the Chinese people say, only in the hottest of fires may the best swords be made.

For now I would like to thank my supervisors, that is to say Prof. Silvia Arcelli, Prof. Francesco Noferini, and Prof. Eugenio Scapparone, all the TOF group who has been so enthusiastic in taking me in, especially Dr. Pietro Antonioli and Dr. Roberto Preghenella, and my past supervisor for the bachelor thesis Dr. Lorenzo Bellagamba. Many thanks to Nicolò Jacazio (PhD student of the TOF group).

Thanks to my mom and dad, who seem to be very proud of what I have become.

Bibliography

[1] N. Cabibbo and G. Parisi: Phys.Lett. 59B, 67 (1975) 2.

[2] J. Cleymans and H. Satz: Z. Phys. C 57, 135 (1993) 16.

[3] K. Redlich et al.: Nucl.Phys. A 566, 391 (1994).

[4] P. Braun-Munzinger et al.: Phys.Lett. B 344, 43 (1995).

[5] F. Becattini: Z.Phys. C 69, 485 (1996.)

[6] F. Becattini and U. Heinz: Z.Phys. C 76, 268 (1997) 16.

[7] L.D. Landau: Izv.Akad.Nauk Ser. Fiz. 17, 51 (1953) 16.

[8] J.-P. Blaizot and J.-Y. Ollitrault: Title. In: R.C. Hwa (ed.) Quark-Gluon Plasma 2, World Scientific, Singapore (1990).

[9] U. Heinz, P.F. Kolb and J. Sollfrank, Phys.Rev. C 62, 054909 (2000) 16.

[10] E.V. Shuryak: Phys.Rep. 61, 71 (1980) 16.

[11] K. Kajantie and H.I. Miettinen: Z.Phys. C 9, 341 (1981) 16.

[12] S. Datta et al.: Phys.Rev. D 69, 094507 (2004) 17.

[13] G. Aarts et al.: Phys.Rev. D 67, 0945413 (2007) 17.

[14] T. Matsui and H. Satz: Phys.Lett. B 178, 416 (1986) 18.

[15] F. Karsch and H. Satz: Z.Phys. C 51, 209 (1991) 18.

[16] J.D. Bjorken: Fermilab-Pub-82/59-THY (1982) 18.

[17] M. Gyulassy and X.-N. Wang: Nucl.Phys. B 420, 583 (1994).

[18] R. Baier et al.: Phys.Lett. B 345, 277 (1995).

[19] B.G. Zakharov: JETP Lett. 63, 952 (1996) 18.

[20] N. Armesto et al., J.Phys.G 35: 054001, 2008.

[21] K. Geiger and B. Müller: Nucl.Phys. B369, 600 (1992) 72, 81, 97.

[22] K. Geiger and D.K. Shrivastava: Nucl.Phys. A661, 592 (1999) 72, 81, 97.

[23] U. Heinz: nucl-th/9810056 82, 84, 95.

[24] CMS Collaboration. Measurement of the pseudorapidity and centrality dependence of the transverse energy density in Pb–Pb collisions at $\sqrt{s_{\mathrm{NN}}} = 2.76$ TeV, `arXiv:1205.2488 [nucl-ex]`, 2012.

[25] M. Gyulassy, I. Vitev, X.N. Wang and B.W. Zhang: `arXiv:nucl-th/0302077 141`.

[26] A. Kovner and U.A. Wiedemann: arXiv:hep-ph/0304151 141.

[27] T. Matsui and H. Satz: Phys.Lett. B 178, 416 (1986) 141.

[28] C. Eckart: Phys.Rev. 58, 919 (1940) 142, 145.

[29] C. Cattaneo: Atti.Sem.Mat.Fis.Univ.Modena 3, 83 (1948) 153.

[30] L.D. Landau, E.M. Lifshitz: Fluid Mechanics, pp. 133136, Pergamon Press, New York (1959) 145.

[31] M. Namiki and C. Iso: Prog.Theor.Phys. 18, 591 (1957).

[32] C. Iso, K. Mori and M. Namiki: Prog.Theor.Phys. 22, 403 (1959).

[33] I. Müller: Z.Phys. 198, 329 (1967).

[34] W. Israel: Ann.Phys. 100, 310 (1976).

[35] W. Israel and J.M. Stewart: Ann.Phys. 118, 341 (1979).

[36] J.D. Bjorken: Phys.Rev.D 27, 140 (1983) 150, 151, 155.

[37] A. Hosoya and K. Kajantie: Nucl.Phys.B 250, 666 (1985).

[38] F. Bastianelli, Notes on Path Integrals, `http://www-th.bo.infn.it/people/bastianelli/3-Path-i`

[39] A. Tawfik, and T. Harko, Quark-Hadron Phase Transitions in Viscous Early universe, `arXiv:1108.5697 [astro-ph.CO]`.

[40] S. Sarkar, H. Satz et al., The physics of the Quark-Gluon Plasma, Springer.

[41] R. Vogt, Ultrarelativistic Heavy-Ion Collisions, Elsevier.

[42] M. Asakawa and T. Hatsuda: Nucl.Phys. A 610, 470c (1996) 5, 9.

[43] P.F. Kolb and U.W. Heinz: arXiv:nucl-th/0305084 154, 163, 166.

[44] P. Huovinen: `arXiv:nucl-th/0305064`.

[45] P. Huovinen and P.V. Ruuskanen: Ann.Rev.Nucl.Part.Sci. 56, 163 (2006).

[46] T. Hirano: Acta Phys.Pol.B 36, 187 (2005).

[47] T. Hirano: Prog.Theor.Phys.Suppl. 168, 347 (2007).

[48] Y. Hama, T. Kodama and O. Socolowski Jr.: Braz.J.Phys. 35, 24 (2005).

[49] F. Grassi: Braz. J. Phys. 35, 52 (2005).

[50] C. Nonaka: J. Phys. G 34, S313 (2007) 154.

[51] ALICE Collaboration, Centrality Dependence of Charged Particle Production at Large Transverse Momentum in Pb–Pb Collisions at 2.76 TeV, `arXiv:1208.2711 [hep-ex]`.

[52] P.J. Siemens and J.O. Rasmussen: Phys.Rev.Lett. 42, 880 (1979) 157, 158.

[53] E. Schnedermann, J. Sollfrank and U.W. Heinz: Phys.Rev.C 48, 2462 (1993) 157, 158.

[54] A.P. Kalweit, Highlights from ALICE, QM 2018 The 27th Int. Con. on Ultrarelativistic Nucleus-Nucleus Collisions.

[55] P. Braun-Munzinger, K. Redlich and J. Stachel: arXiv:nucl-th/0304013 156.

[56] F. Bellini, Testing the system size dependence of hydrodynamical expansion and thermal particle production via the production of π, K, p, and ϕ in Xe–Xe and Pb–Pb collisions with ALICE, QM 2018 The 27th Int. Con. on Ultrarelativistic Nucleus-Nucleus Collisions.

[57] M. Floris, Hadron yields and the phase diagram of strongly interacting matter, Nuclear Physics A 00 (2014).

[58] A.M. Poskanzer and S.A. Voloshin: Phys.Rev.C 58, 1671 (1998) 160.

[59] J.Y. Ollitrault: Phys.Rev.D 46, 229 (1992) 161.

[60] H. Heiselberg and A.M. Levy: Phys.Rev.C 59, 2716 (1999) 161.

[61] H. Sorge: Phys.Rev.Lett. 82, 2048 (1999).

[62] S.A. Voloshin and A.M. Poskanzer: Phys.Lett.B 474, 27 (2000) 161.

[63] M.W. Phipps, A New ATLAS ZDC for the High Radiation Environment at the LHC, 18th International Conference on Calorimetry in Particle Physics.

[64] CMS Collaboration, CMS Technical Design Report for the Level-1 Trigger Upgrade.

[65] `http://aliceinfo.cern.ch/Public/en/Chapter2/Chap2InsideAlice-en.html`

[66] D.K. Swoboda et al., Results from the ALICE dipole magnet commissioning, Proceedings of the 19 th International Conference on Magnet Technology, Genua Italy, IEEE Trans. Appl.Sup., June 2006, IEEE Trans. Appl. Supercond. 16 (2006) 1696.

[67] ALICE collaboration, ALICE time projection chamber: Technical Design Report, CERN-LHCC-2000-001, `http://cdsweb.cern.ch/record/451098`.

[68] Alice Collaboration, Technical Design Report for the Upgrade of the ALICE Time Projection Chamber, `https://cds.cern.ch/record/1622286/files/ALICE-TDR-016.pdf`.

[69] C. Garabatos, The ALICE TPC, Nucl.Instrum.Meth. A 535 (2004) 197.

[70] J. Wiechula et al., High-precision measurement of the electron drift velocity in Ne-CO_2 , Nucl.Instrum.Meth. A 548 (2005) 582.

[71] ALICE collaboration, ALICE transition-radiation detector: Technical Design Report,CERN-LHCC-2001-021, `http://cdsweb.cern.ch/record/519145`.

[72] ALICE collaboration, ALICE Time-Of-Flight system (TOF): Technical Design Report,CERN-LHCC-2000-012, `http://cdsweb.cern.ch/record/430132`; ALICE Time-Of Flight system (TOF): addendum to the technical design report, CERN-LHCC-2002-016, `http://cdsweb.cern.ch/record/545834`.

[73] C. Grupen et B. Schwarz, Particle Detectors.

[74] The ALICE-TOF Group, The ALICE TOF System.

[75] ALICE-TOF Group, TDR of the TOF System.

[76] Wikipedia, `https://en.wikipedia.org/wiki/Soda\%E2\%80\%93lime\_glass`.

[77] A. Akindinov et al., Latest results on the performance of the multigap resistive plate chamber used for the ALICE TOF, NIM A 533 no. 1, (2004) 74-78.

[78] F. Carnesecchi (on behalf of the ALICE Collaboration), Performance of the ALICE Time-Of-Flight detector at the LHC, `arXiv:1806.03825 [physics.ins-det]`.

[79] ALICE collaboration, ALICE high-momentum particle identification: Technical Design Report, CERN-LHCC-98-019, `http://cdsweb.cern.ch/record/381431`.

[80] ALICE collaboration, Technical design report of the photon spectrometer, CERN-LHCC-99-004, `http://cdsweb.cern.ch/record/381432`.

[81] ALICE collaboration, ALICE electromagnetic calorimeter: addendum to the ALICE technical proposal, CERN-LHCC-2006-014, `http://cdsweb.cern.ch/record/932676`.

[82] ALICE collaboration, ALICE Photon Multiplicity Detector (PMD): Technical Design Report, CERN-LHCC-99-032, http://cdsweb.cern.ch/record/451099; ALICE Photon Multiplicity Detector (PMD): addendum to the technical design report, CERN-LHCC-2003-038, http://cdsweb.cern.ch/record/642177.

[83] ALICE collaboration, ALICE forward detectors: FMD, TO and VO: Technical Design Report , CERN-LHCC-2004-025, http://cdsweb.cern.ch/record/781854.

[84] M. Bondila et al., ALICE T0 detector, IEEE Trans. Nucl. Sci. 52 (2005) 1705.

[85] ALICE Collaboration, Determination of the event collision time with the ALICE detector at the LHC, arXiv:1610.03055 [physics.ins-det].

[86] ALICE Collaboration, Centrality dependence of the nuclear modification factor of charged pions, kaons, and protons in Pb-Pb collisions at $\sqrt{s_{\rm NN}} = 2.76$ TeV, arXiv:1506.07287 [nucl-ex].

[87] X.N. Wang and M. Gyulassy, HIJING: A Monte Carlo model for multiple jet production in pp, p–A and A–A collisions, Phys.Rev.D 44 (1991) 3501-3516.

[88] Alice Collaboration, Transverse momentum spectra and nuclear modification factors of charged particles in Xe–Xe collisions at $\sqrt{s_{\rm NN}} = 5.44$ TeV, arXiv:1805.04399.

[89] Alice Collaboration, Centrality dependence of π, K and p production in Pb–Pb collisions at $\sqrt{s_{\rm NN}} = 2.76$ TeV, Phys.Rev.C 88, 044910 (2013).

[90] J. Adams et al., STAR Collaboration, Phys. Rev. Lett. 92 (2004) 052302.

[91] G.E. Bruno, A. Dainese (for the NA57 Collaboration), First measurement of the strange particles Rcp nuclear modification factors in heavy-ion collisions at the SPS, arXiv:nucl-ex/0511020.

[92] B.Abelev et al. (ALICE Collaboration), Phys.Rev.Lett.109(2012)252301.

[93] J. Anielski, M.Chojnacki, M. Floris, B. Guerzoni, A. Kalweit, L.Milano, R.Preghenella. Spectra analysis pp at $\sqrt{s}t = 7$TeV, PbPb at $\sqrt{s_{NN}} = 2.76$ TeV. ALICE-ANA 570.